POLITECNICO DI TORINO

Master of Science in Energy and Nuclear Engineering

Joint M.Sc. Program in Nuclear Engineering with Politecnico di Milano

Master Thesis

Extension and application of TRANSURANUS fuel performance code to the MYRRHA reactor in normal and transient conditions

Supervisors:
Prof. Cristina Bertani
Prof. Lelio Luzzi (PoliMi)
Dr. Davide Pizzocri (PoliMi)

Candidate:
Erik Guizzardi

March 2020

Abstract

The Belgian Nuclear Research Centre (SCK•CEN) is designing an innovative Accelerator Driven System (ADS) called MYRRHA (Multi-purpose Hybrid Research Reactor for High-tech Applications), embedded inside the European Sustainable Nuclear Industrial Initiative (ESNII) program. Objectives of this facility are to prove the feasibility of the ADS concept at a reasonable power level and to sustain the development of future Generation IV reactors making available a heavy metal-cooled core environment featured by a fast neutron spectrum. This work deals with MYRRHA fuel pin performance analysis employing the TRANSURANUS fuel performance code, with the aim of assessing the current design specifications in normal operating conditions and in the event of a particular design basis accident originating from a particle accelerator trip (i.e., a beam power jump, BPJ). For simulating in a thorough way the fuel pin response, the TRANSURANUS applicability is extended to the specific cladding material adopted for MYRRHA, contributing to its predictive capability enlargement by implementing five new correlations. The thermo-mechanical simulations are carried out considering a conservative fictitious hottest fuel pin and employing the most reliable set of input models suggested by the TRANSURANUS manual, relying upon fuel and cladding design limits for normal operating conditions and for the overpower accidental transient. A sensitivity analysis on phenomena/properties which most affect the scenario results is performed, with the purpose of facing the issue linked to model uncertainties in a deterministic way, providing a conservative assessment of the fuel pin design. The main outcome of this analysis is that the MYRRHA fuel pin performs well below the design limits in both normal operation and BPJ conditions. Considering the wide safety margins unveiled in the accidental scenarios, the linear power required to exceed the design limits is investigated, supplying a useful indication for licensing purposes or for devising a potential reactor power increment.

Contents

List of acronyms

ADS	Accelerator Driven System
ALFRED	Advanced Lead Fast Reactor European Demonstrator
BoL	Beginning of Life
BPJ	Beam Power Jump
BR2	Belgian Reactor 2
DeBeNe	Deutschland-Belgium-Netherlands
EBR-I	Experimental Breeder Reactor I
EFIT	European Facility for Industrial Transmutation
EoL	End of Life
ESNII	European Sustainable Nuclear Industrial Initiative
EURATOM	EURopean ATOMic energy community
EUROTRANS	EUROpean research programme for the TRANSmutation of high level nuclear waste in an accelerator driven system
FCCI	Fuel-Cladding Chemical Interaction
FCMI	Fuel-Cladding Mechanical Interaction
FGR	Fission Gas Release
FR	Fast Reactor
GFR	Gas-cooled Fast Reactor
GIF	Generation IV International Forum
INSPYRE	INvestigations Supporting MOX fuel licensing in ESNII PrototYpe REactors
IPS	In-Pile test Sections
ITU	Institute for TransUranium elements
LBE	Lead-Bismuth Eutectic
LFR	Lead-cooled Fast Reactor

LINAC	LINear ACcelerator
LM	Larson Miller
LME	Liquid Metal Embrittlement
LMFBR	Liquid Metal-cooled Fast Breeder Reactor
LMP	Larson Miller Parameter
LWR	Light Water Reactor
MOX	Mixed-OXide
MTR	Material Testing Reactor
MYRRHA	Multi-purpose hYbrid Research Reactor for High-tech Applications
ODS	Oxide-Dispersion Strengthened
PLB	Power-Law Breakdown
RC	Reference Case
SCK•CEN	StudieCentrum voor Kernenergie • Centre d'Étude de l'énergie Nucléaire
SFR	Sodium-cooled Fast Reactor
TRU	TRansUranic
WC	Worst Case

List of figures

List of tables

List of tables

Chapter 1

Introduction

A key point during the design of a reactor is the assessment of fuel pin thermo-mechanical performance, consisting in studying the capability of the pins to sustain the conditions they will undergo during their three to four years in-reactor life. The main common features to be assessed are the maximum fuel and cladding temperatures, cladding deformation (allowing to preserve its tightness and its effective external cooling) and the plenum pressure reached at the end of the irradiation history after the release of fission gases from the fuel [1][2].
A large number of phenomena is involved in determining the ultimate fuel pin response [3][4]. Given that, very often, a strong interrelationship between them exists and many processes are non-linear, computer codes were developed in the past and are currently widely employed to support both reactor design and verification [5]. These codes take in input the axial distribution of power and neutron flux as functions of time and are able to compute the evolution of the fuel pin thermo-mechanical state with a degree of accuracy dependent on their spatial representation of the domain.
TRANSURANUS [6][7] is a fuel performance code developed in the 1970s at the Institute for Transuranium Elements (ITU), widely assessed for light water reactor (LWR) conditions and now used to simulate both LWRs and fast reactors (FRs). It pertains to the category of 1.5D codes[1] and solves the bulk equations of thermo-mechanics together with additional physical and empirical models describing each of the fuel and cladding phenomena (most of which are irradiation induced). During its development, great effort was spent on obtaining an extremely flexible tool:

[1] Despite the actual fuel pin domain is 3D, the very long and thin rod structure suggests to treat any axial section as part of an infinite body [56]. The cylindrical shape, then, allows assuming an axially symmetric condition, meaning to ignore dependences on the rotational angle. Codes which make such hypothesis are called 1.5D given that the axial derivatives are called off, but the simulation outcomes are 1D radial profiles coupled along the axial coordinate (according to the boundary condition). The computational time is restrained for such codes allowing potentially to analyse all the fuel pins inside a reactor core. Common examples of 1.5D fuel performance codes, besides TRANSURANUS, are GERMINAL [60], FRAPCON [61] and FRAPTRAN [62].
A higher level of detail is provided, instead, by 2D and 3D tools such as FALCON [63], BISON [64] and ALCYONE [65], mostly applied to investigate local effects due to their computational cost.

it is possible to exploit TRANSURANUS both for normal, off-normal and accidental conditions and it is very easy to incorporate new correlations and physical models in the code [7]. These advantages, together with an extensive code validation and very fast running, are the primary features justifying its recent and past success [8].

Nowadays, the need for safer and more sustainable technologies has strongly affected the nuclear energy field, requiring the introduction of a new generation of reactors [9]. In such context, fuel performance codes constitute again a helpful tool to assist in the fuel pin design. The implementation of Generation IV systems (especially fast reactors), however, calls for new materials, capable to stand against the extremely demanding conditions (in terms of power and neutron flux) they will be asked to operate in [10]. In order to be properly exploited, fuel performance codes must be updated accordingly.

To improve the code predictive capabilities for fast reactor fuel performance and to transfer their results to end-users for contributing in the development of ESNII prototypes[2], are two of the strategic objectives of the INSPYRE (Investigations Supporting MOX Fuel Licensing in ESNII Prototype Reactors) H2020 European Project [11], specifically addressed in the Work Package 7 [12].

This thesis work joins the INSPYRE project itself and deals with the fuel performance assessment for the MYRRHA (Multi-purpose Hybrid Research Reactor for High-tech Applications) reactor, an innovative facility under design at the Belgian Nuclear Research Centre (SCK•CEN) as a multipurpose Accelerator Driven System for R&D applications. In particular, the TRANSURANUS code is applied, and both normal operating conditions and a transient scenario selected among the design basis accidents (in its worst possible progression) are considered [13].

An improvement of the TRANSURANUS code itself is carried out as first essential step towards the simulation of the MYRRHA fuel pin behaviour, with the aim to extend the code applicability to DIN1.4970 double stabilized austenitic stainless steel, the cladding material adopted for MYRRHA [14]. A review of the original *v1m1j18* TRANSURANUS version is performed to assess the standard code predicting capabilities, followed by an integration based on what it can be found in the open literature. Such effort must be intended useful to the scope of the present work but also for a wider application, complying with the first INSPYRE strategic objective[3].

After the extension of the TRANSURANUS code, MYRRHA thermo-mechanical performance is conservatively analysed considering a fictitious hottest pin. In this regard, two sets of responses are evaluated: a “reference case” obtained employing all the input model options suggested as the most reliable ones by the code manual; a “worst case” needed to account in a deterministic way for the effects of such phenomena/properties crucial in outlining the fuel pin behaviour and affected by high uncertainties. The worst case scenario is discovered through a sensitivity analysis on models and supplies the worst fuel pin condition at the end of the irradiation history. This

[2] The ESNII (European Sustainable Nuclear Industrial Initiative) program was born in 2010 and addresses the need for demonstration of Generation IV fast neutron reactor technologies, together with the supporting research infrastructures, fuel facilities and R&D work [66]. Within the program, four prototypes are under design: ASTRID as sodium fast reactor [67], MYRRHA and ALFRED as lead fast reactors [18][47], ALLEGRO as gas fast reactor [69].

[3] Actually, since the fuel is the main target of the INSPYRE project, this part of the work may be considered as its complementary but natural extension, being a thorough investigation of cladding properties crucial for a proper fuel pin design assessment.

allows comparing the results with the correspondent fuel and cladding design limits, providing a conservative judgement regarding the current fuel pin specifications, both in normal operating conditions and for the design basis accident of interest.

The structure of the work reflects its own goals. First of all, a complete description of the MYRRHA facility and its framework in the today's nuclear energy field context is discussed in Chapter 2. In Chapter 3, the specific cladding material choice is revealed and motivated, followed by the improvement of the TRANSURANUS code for an effective MYRRHA simulation. The fuel pin performance assessment, firstly for normal operating conditions and then for the accidental scenarios, is investigated in Chapter 4 and Chapter 5, respectively. Finally, Chapter 6 summarizes the main achievements of the present work.

Chapter 2

MYRRHA: framework and facility description

The nuclear source of energy has suffered many ups and downs during its history started in 1951 with EBR-I reactor at Idaho National Reactor Testing Station, the first nuclear facility connected to the electrical grid. The growing worries of the new century about the problem of global warming have increased once more the interest in nuclear power as base-load alternative to coal power plants within a CO_2-free electricity production system, clearly involving renewable energy sources. The current nuclear technology, however, displays technical limitations (e.g., inefficient resource utilization, production of considerable amounts of high-level radiotoxic wastes) and suffers from public scepticism, calling for a complete revolution.

MYRRHA is just one of the numerous innovative facilities with the purpose to pave the way towards next generation nuclear power plants. In particular, it has been embraced by the ESNII project as key facility to support the Advanced Lead Fast Reactor European Demonstrator (ALFRED) development by EURATOM (European Atomic Energy Community), aiming at the same time to prove the Accelerator Driven System (ADS) technological feasibility.

This chapter, besides presenting the current MYRRHA design choices, also wants to depict the scenario under which the facility has been conceived. Accordingly, Section 2.1 deals with the Generation IV International Forum, the first official proof about the innovation calling. The main peculiarities of fast reactors, the most promising perspective on which the consortium is looking at, are discussed within the same section. Finally, before deeply detailing MYRRHA facility in Section 2.2, the last focus is on lead-cooled fast reactors, the family which the MYRRHA reactor belongs to.

2.1 Generation IV reactors

The LWR nuclear technology employed so far in commercial power reactors has shown two main aspects in terms of which it exhibits crucial shortages, requiring deep improvements. First, the three big nuclear accidents (i.e., Three Mile Island, Chernobyl and Fukushima) have fed mistrust inside public opinion concerning the safety of nuclear power plants, having thus to demonstrate they excel under such point of view. A complete revolution of reactor technology together with its fuel cycle, then, is called by today's sustainability goals, both in terms of resource utilization and in terms of waste management. Indeed, current LWRs with a once-through scheme exploit less than 1% of uranium resources, restricting their availability to just 80 years [15] and thereby making compulsory to exploit plutonium as an additional fission energy source. Even employing a Pu-based fuel, moreover, big amounts of high-level radiotoxic wastes are generated, owing to the low energy neutron spectrum causing the build-up of transuranic elements inside the fuel.

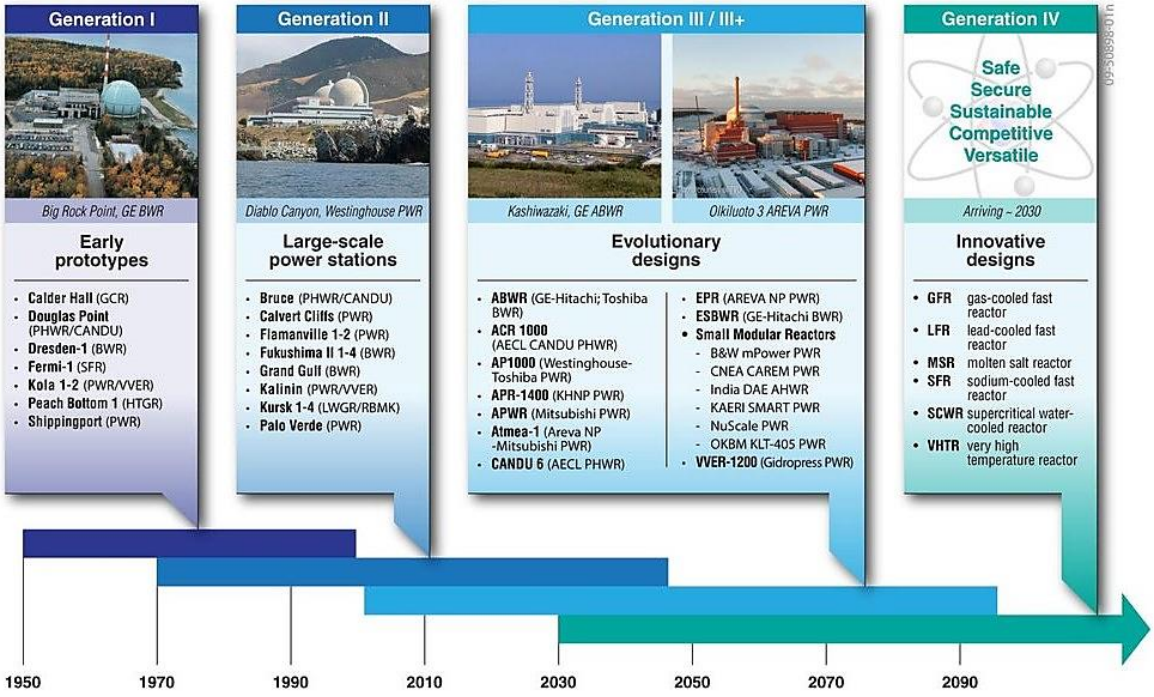

Figure 2.1: Generation IV future role projection [9].

From this scenario, the Generation IV International Forum (GIF) was born in 2000, consisting in an international consortium encouraging collaboration between its members in the development of advanced nuclear systems, capable to affirm the role of nuclear in the future energy contest, overcoming its current weaknesses and public concerns. Final objective is to have the innovative Generation IV reactors ready to produce commercial electricity in the period around 2030 or beyond (Figure 2.1), depending on the degree of technical maturity.
Four broad areas were identified by GIF to set out technology goals useful to guide the cooperative R&D effort and to build on durable pillars the new generation of nuclear reactors [10]:

- SUSTAINABILITY: they must meet clean air objectives, provide long-term availability (optimizing the fuel utilization) and minimize the production of nuclear waste reducing the long-term stewardship burden;

- SAFETY and RELIABILTY: they must excel in safety and reliability in order to have a very low likelihood and degree of reactor core damage, eliminating the need for offsite emergency response as well;
- PROLIFERATION RESISTANCE and PHYSICAL PROTECTION: they must become clearly unattractive for diversion of weapons-usable materials and they must increase the physical protection against acts of terrorism;
- ECONOMY: they must be profitable over other energy sources in terms of lifecycle cost and they must have a level of financial risk comparable to other energy projects.

Based on such objectives, a lot of new reactor proposals were assessed by GIF who eventually identified the six major development tracks[4]. All of them aim at performance improvements through new applications of nuclear energy: some concepts exploit a fast neutron spectrum, others make use of innovative coolants, but all intend to reach high coolant outlet temperatures to improve the overall efficiency and possibly to obtain expendable heat. Figure 2.2 provides a layout sketch of such new systems.

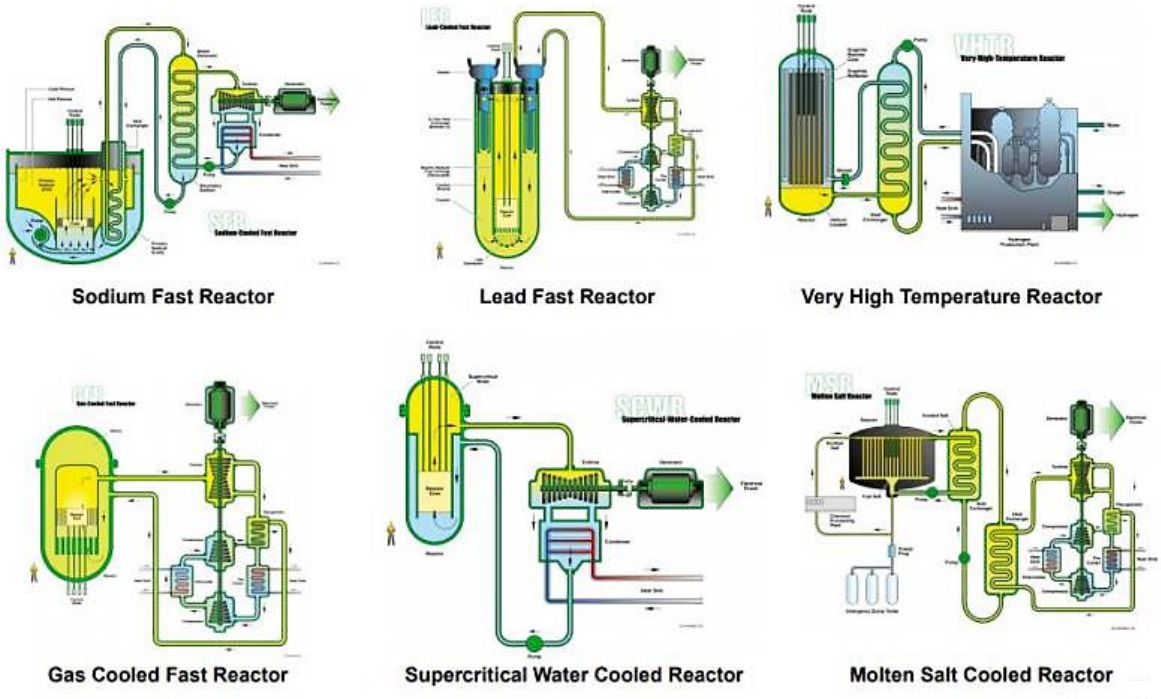

Figure 2.2: Generation IV reactors [16].

Fuel recycling plays an essential role in Generation IV systems in the same way as reactor technology does, because to implement a thorough scheme is the only way to cope with sustainability and proliferation resistance goals. Nowadays, whenever a closed fuel cycle is adopted, the approach involves the separation of pure plutonium oxide (produced by conversion) and unburned ^{235}U in specialized reprocessing plants which are physically separated by NPPs, whereas all the remaining uranium (together with minor actinides and fission products) is treated as waste, being stocked for an indefinite time. This strategy does not meet the GIF requirements

[4] To the six Generation IV nuclear reactor concepts, Small Modular Reactors (SMRs) should be added as well, being a new generation of small power reactors with similar features.

previously mentioned. A possible solution is to rely on fast reactors in the integral fuel cycle, in which the spent fuel of traditional systems forms part of the feed for fast systems, without requiring chemical separation and sensibly reducing the amount of long-lived radioisotopes in the final waste. Whether fuel reprocessing is performed in situ, then the proliferation resistance goal can be fully accomplished as well.

2.1.1 Fast reactors

Fast reactor technology has always been alive during the nuclear era, despite it has never reached a commercial dimension. The first nuclear reactor in history connected to the electrical grid, unexpectedly, was the Experimental (fast) Breeder Reactor I (EBR-I) in 1951 and not a thermal reactor, nonetheless the last ones have dominated the recent nuclear electricity generation scenario. After EBR-I, many experimental fast reactors and prototypes have been operated over years, but a deeper and wider interest in such technology has been fed since the GIF formation in 2000, thanks to its huge potentiality especially from the sustainability point of view, made possible by actinide conversion and transmutation mechanisms.

Conversion, indeed, allows the introduction of breeder reactors[5], in which the fuel consumption switches from ^{235}U (constituting the 0.7% of the total uranium resources on Earth) to ^{238}U (representing the remaining 99.3%), permitting also the utilization of all the depleted uranium stored at present. Thanks to this potentiality, fast reactors would be capable of satisfying the electrical energy needs of the world for thousands of years [15].

In addition, the fast neutron spectrum makes some of the current waste constituents a resource thanks to *transmutation*, sensibly reducing their unused quantity and the time associated to their radiotoxicity burden. Whenever the whole spent fuel is discarded as waste (once-through fuel

[5] Conversion is the process whereby fast reactors can self-produce the fuel they need to operate via the following reactions (considering uranium-based reactors):

$$^{238}\mathrm{U}\ (\mathrm{n},\gamma)\ ^{239}\mathrm{U} \xrightarrow{\beta^-} {}^{239}\mathrm{Np} \xrightarrow{\beta^-} {}^{239}\mathrm{Pu}$$

where ^{238}U is the fertile isotope and ^{239}Pu is the fissile one. This chain reaction takes place inside every uranium-based reactor core but just in specific conditions it is possible to call it a breeding reaction. The requirement is that the conversion ratio (i.e., the ratio between the fissile atoms produced by conversion and those consumed) must be greater than 1 so that more fissile fuel is created than what is burnt. In order to make such condition feasible, the reproduction factor inside the four factor formula [70] must be sufficiently bigger than 2: in this way, on average one neutron is capable to continue the fission chain reaction and another one to induce the conversion of a fertile nucleus, taking into account that some neutrons will escape or will encounter parasitic capture. Considering a plutonium-fuelled reactor, thermal energies are insufficient to support such conditions, being the reproduction factor too close to 2 as inferred from Figure 2.3; instead, fast energies allow having the parameter in excess of 2 enough for breeding to occur: this explains why a nuclear reactor must exploit a fast neutron spectrum to be a breeder.

To make a breeder reactor fully effective, it must be coupled to a proper fuel cycle. Adopting a closed fuel cycle for a LWR (which is merely a converter, meaning a system capable to produce fissile fuel by conversion in "small" quantities) entails a reprocessing stage for the spent fuel, during which the produced ^{239}Pu and the unburned ^{235}U are chemically extracted and re-introduced inside the reactor after plutonium has been mixed to UO_2 to produce mixed-oxide fuel (MOX) and fissile uranium has been sufficiently re-enriched; in this way, the required external amount of ^{235}U is decreased by an effective 40% [15]. The fuel cycle for a breeder is very similar, however the plutonium production is big enough to avoid an additional ^{235}U supply from outside: after the first cycle, the only reactor feed is MOX fuel composed by yielded plutonium and natural or depleted uranium, making the external fuel consumption switched from ^{235}U to ^{238}U.

cycle), indeed, it contains fission products and transuranic (TRU) atoms, including major actinides (uranium and plutonium isotopes) and minor ones (americium, neptunium, curium and californium), both produced by neutron capture; in case of a closed fuel cycle, some of the major actinides are recovered but minor ones and fission products still remain an issue[6]. The primary desire linked to the nuclear waste problem is to shorten the time for radiotoxicity to be reduced [4], and this can be accomplished by partitioning and transmutation strategy. That is, fission products are separated from major and minor actinides (partitioning), so that they can be stored as the real nuclear waste for about 300 years. The TRU fraction, instead, can be burned again: similarly to major actinides, minor ones can be considered as a resource for fast reactors because at high neutron energies they preferentially tend to fission (transmutation), whereas in LWRs they commonly transform to higher actinides as a result of neutron capture. Consequently, minor actinides can be mixed with plutonium and uranium inside the fast reactor fuel, allowing the conversion (under irradiation) to more stable elements (more readily handled and disposed) and the exploitation of an additional source of energy.

By relying on the two mechanisms, FRs would provide a flexible system in which it is either possible to yield fissile material by breeding fertile ^{238}U (fast breeder configuration), or to destroy TRU isotopes in depleted fuel (fast burner configuration). Both the two configurations ask for a hard neutron spectrum which can be achieved only by a proper selection of the coolant: gas-cooled fast reactors (GFRs) and liquid metal-cooled fast breeder reactors (LMFBRs) are both valid alternatives.

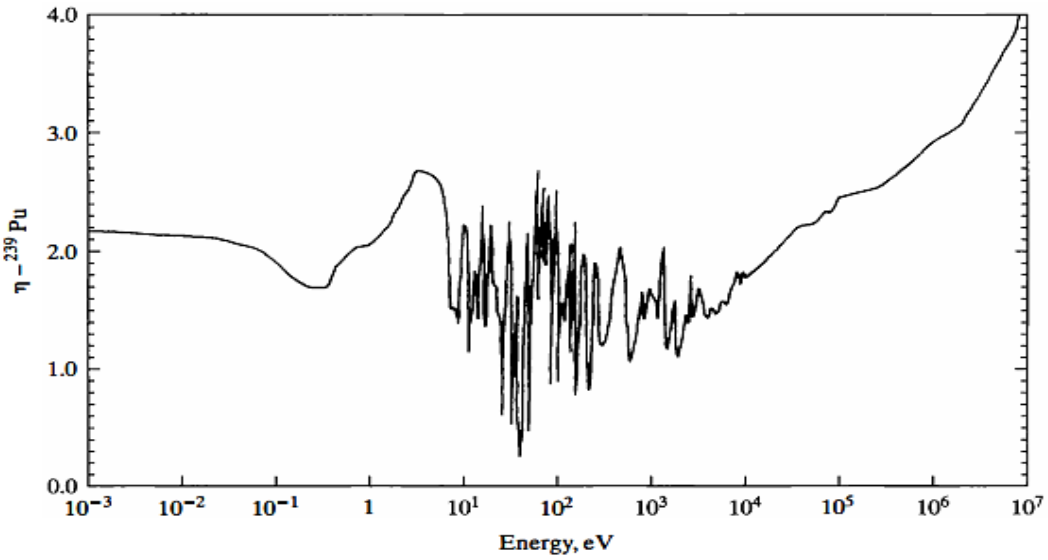

Figure 2.3: Reproduction factor dependence on energy for ^{239}Pu [15].

[6] The major concern related to nuclear high-level waste derives from the TRU fraction, featured by half-lives of the order of hundreds of thousands of years and so requiring exceptionally durable repositories which are still not operational. On the other hand, the vast majority of fission products are very short-lived and just three of them (^{90}Sr, ^{90}Y, ^{137}Cs) have half-lives requiring the storage for few hundreds of years.

2.1.2 Lead fast reactors

Lead-cooled fast reactors (LFRs) are one of the most promising concepts pertaining to the Generation IV family and, together with sodium-cooled fast reactors (SFRs), the only ones for which an operational expertise is already available[7].

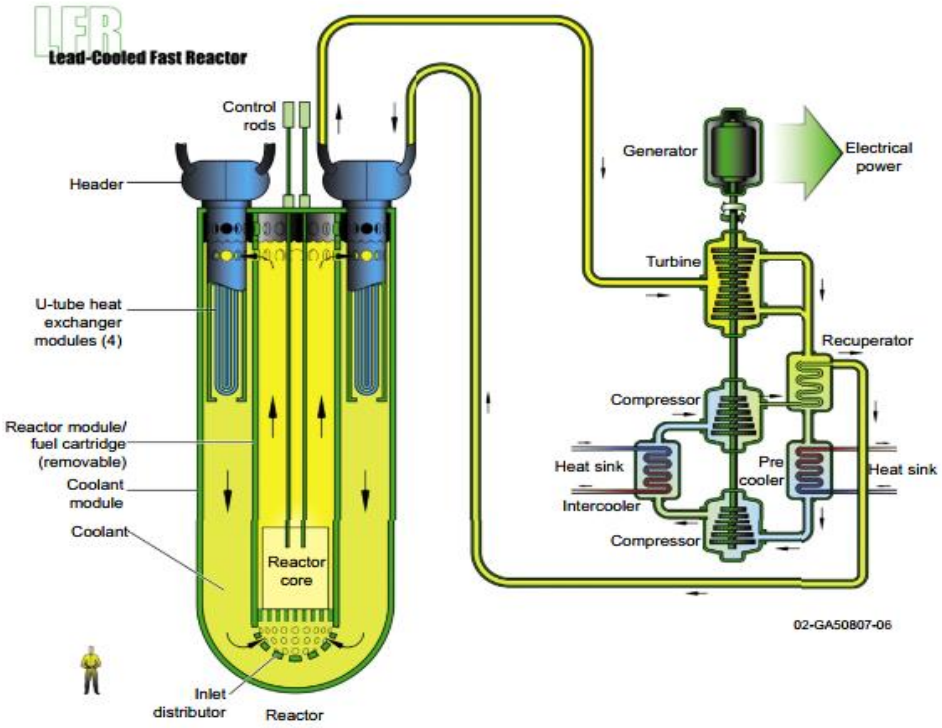

Figure 2.4: Generation IV lead fast reactor with an indirect Brayton cycle [10].

LFRs (Figure 2.4) are fast neutron spectrum reactors for which the key feature is the adoption of either lead or LBE[8] as a coolant. Such choice entails a long list of advantages:

- It allows hosting a neutron spectrum harder than any other Generation IV concept thanks to the huge difference in mass between neutrons and coolant atoms, making the transmutation process very effective when a burner configuration is adopted;
- The coolant is compatible with high temperature operation requirements and does not need a strong pressurization, thanks to the very high boiling point of both lead and lead-bismuth eutectic (Table 2.1);
- Lead and LBE are relatively inert liquid metals in terms of interaction with air or water (they do not bring to hydrogen formation, fires and explosions), hence it is not asked to adopt an intermediate circuit as for SFRs, allowing a net efficiency of over 40% [10];

[7] Starting from the late 1950s, lead-bismuth eutectic-cooled fast reactors were designed and built in Soviet Union for the purpose of submarine propulsion, allowing the collection of 15 reactors experience, two of which on-shore. Although significant differences exist between those reactors and the innovative systems currently under study, the acquired knowledge provides a strong base for understanding the technology and its issues, making it rather mature.

[8] LBE is the eutectic alloy of lead and bismuth, consisting of 44.5% Pb and 55.5% Bi (which are both heavy elements).

- A significant thermal inertia is supplied by the high latent heat and the high thermal capacity of liquid metals in the event of loss of heat sink;
- The low coolant moderation permits greater spacing between fuel pins, reducing core pressure losses; such fact, coupled with optimal heat transfer properties of the liquid metal, makes natural circulation cooling effective for the primary system, so that it is possible to rely upon for a passive shutdown heat removal.

Some drawbacks also exist when lead or LBE are adopted as coolants: the most severe is the corrosive and erosive nature of the heavy metal on structural materials and on the fuel pin cladding, calling for the use of highly corrosion/erosion resistant materials. Then, their exceptional density is the cause of high pumping power requirements, besides the difficulty to achieve a seismically safe design. Finally, the high melting temperature asks for an electrical heating at startup and a secondary inlet temperature at the steam generator higher than the melting point itself to avoid solidification of the metal.

Lead and lead-bismuth eutectic

Lead and LBE as fast reactor coolants share all the aforementioned advantages of liquid heavy metals, despite their own peculiarities make the one or the other preferable under different points of view.

LBE displays the lowest possible melting temperature of the compound (Table 2.1), which is the primary reason justifying the technological interest on it; additionally, it can be employed in ADS as a moving spallation target, capable to supply an effective cooling at the same time. Whereas lead is abundant and so available in case of deployment of a large number of reactors, however, bismuth availability is limited, arising doubts about LBE-cooled reactors sustainability. Furthermore, it is more expensive and more corrosive than pure lead and has a lower thermal conductivity. Last but crucial feature, the bismuth contained inside LBE tends to capture neutrons producing large amounts of ^{210}Po via the following reaction:

$$^{209}\mathrm{Bi} + \mathrm{n} \rightarrow {}^{210}\mathrm{Bi} \xrightarrow{\beta^-} {}^{210}\mathrm{Po}$$

Being ^{210}Po an α-emitter (with 5.3 MeV energy), its inventory inside the coolant constitutes a dangerous source of radioactivity: in the event of leakage (and every time it is needed to get access to reactor internals, including refuelling and decommissioning), indeed, volatile polonium hydrides are released when hot LBE enters in contact with air.

Pure lead forms ^{210}Po as well, after it has transmuted into ^{209}Bi. Nevertheless, the rate of production is much lower: coolant radiotoxicity is the primary feature which actually makes lead the reference coolant for future LFRs according to Generation IV roadmap.

Table 2.1: Comparative properties of liquid metal coolants [17].

Coolant	Melting point [°C]	Boiling point [°C]	Chemical reactivity with air and water
Lead	327	1737	Essentially inert
LBE	124	1670	Essentially inert
Sodium	98	883	Highly reactive

2.2 MYRRHA

MYRRHA is an innovative facility under design at the Belgian Nuclear Research Centre as a "multipurpose Accelerator Driven System for R&D applications"[8] and it represents the first practical implementation of the ADS technology, besides being a modern LBE-cooled fast reactor. Originally conceived as a replacement for the BR2 facility[9] (licensed until 2026), the MYRRHA project was willingly enclosed by GIF and then by ESNII project, being considered pivotal for the development of future LFRs and Generation IV systems in general. Continuing the BR2 reactor work, indeed, MYRRHA will have the following goals [18]:

- To demonstrate the ADS concept at reasonable power level;
- To allow studying the efficient transmutation of high-level nuclear waste (being a fast spectrum facility cooled by a heavy liquid metal);
- To be operated as a flexible fast spectrum irradiation facility allowing for the investigation and assessment of fuel and materials for Generation IV and fusion systems;
- Radioisotopes production.

Besides being exploited as a research reactor, the facility will be connected to the electrical grid as well, providing clean commercial energy.

As for the project timeline, originally MYRRHA was thought to be operational at full power around 2026. However, the Fukushima accident and the economic crisis have drastically impacted the program development. Currently, a phased implementation strategy has been decided for, with a first phase bringing to the construction of a reduced power accelerator able to produce radioisotopes and to perform physics R&D. The extension of the accelerator power and the construction of the reactor will be carried out in parallel afterwards, allowing to start operation in 2036 [19].

2.2.1 The ADS concept of MYRRHA

The Accelerator Driven System is a revolutionary concept inside the nuclear energy field, since it makes use of a subcritical fast core which would not be capable to sustain fission chain reactions alone. However, a particle accelerator is coupled to the core: the idea is to exploit spallation reactions induced by high energy protons inside the core to obtain the missing neutrons required to have a stable neutronic population and so a constant power level.

In Figure 2.5, the functioning of MYRRHA facility is sketched: a proton source sends particles to an accelerator (LINAC) and, finally, to the centre of the subcritical core. Here, bismuth nuclei from the LBE coolant are hit by accelerated protons, producing neutrons by (p, n) (spallation) reactions[10]: these neutrons are those capable to bridge the gap towards a stable neutronic population. Furthermore, the neutrons in excess can be exploited to transmute minor actinides,

[9] BR2 (Belgian Reactor 2) is a Material Testing Reactor (MTR) employed since 1962 by SCK•CEN to carry out scientific campaigns inside the nuclear energy field, including material research for fission and fusion reactors, fuel research, reactor safety and also for the production of radioisotopes for medical and industrial applications.

[10] The choice of LBE both as coolant and as spallation source calls for a beam window, i.e., a physical interface dividing the beam duct from the LBE itself, necessary to avoid the entrance of the second inside the first.

making the ADS concept very interesting under the sustainability point of view, and making MYRRHA attractive to study transmutation feasibility.
The facility owns exceptional intrinsically safe features justifying its attractive. Since the fissile material is not sufficient to maintain the fission chain reaction alone, indeed, it must be continuously fed by the external neutron source through the accelerator. This means that, by switching off the particle accelerator, the reactor shuts down instantaneously.

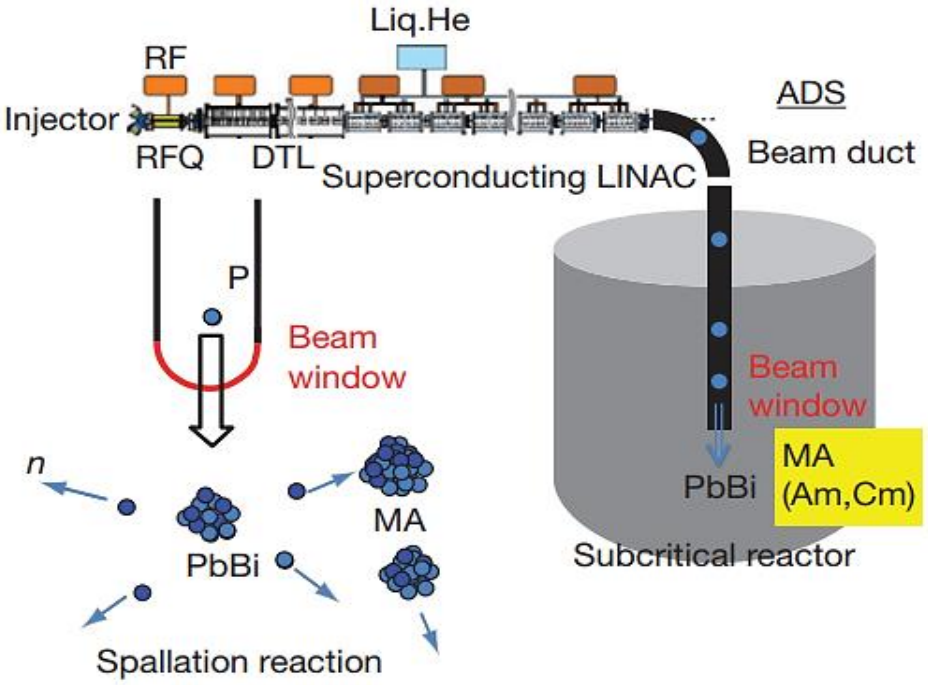

Figure 2.5: Conceptual model of MYRRHA Accelerator Driven System [20].

2.2.2 Reactor description

MYRRHA was designed as a 100 MW_{th} pool-type ADS capable to operate both in subcritical mode and in critical one with a fast neutron spectrum. When the facility operates as ADS, the accelerator is coupled to the reactor fast core, whereas control and shutdown rods must be available whether it operates as a traditional nuclear reactor.
A linear accelerator (LINAC) was selected to generate the proton beam[11] and it is hosted in a separated accelerator building, as shown in Figure 2.6. The accelerator communicates with the reactor building by means of a LINAC tunnel (buried under a layer of sand), providing the proton beam in continuous wave mode from above the reactor vessel (Figure 2.7) through a dedicated central assembly via a beam window.

[11] At present, only LINAC and sector focused cyclotrons are able to provide megawatt level particle beams. The second ones, however, cannot guarantee any modularity in case of faults differently from a LINAC, which instead allows recovery times very small. For these reasons, a LINAC was preferred.

Figure 2.6: Panoramic view of MYRRHA project: reactor building (on the left), LINAC tunnel (centre) and accelerator building (on the right) [21].

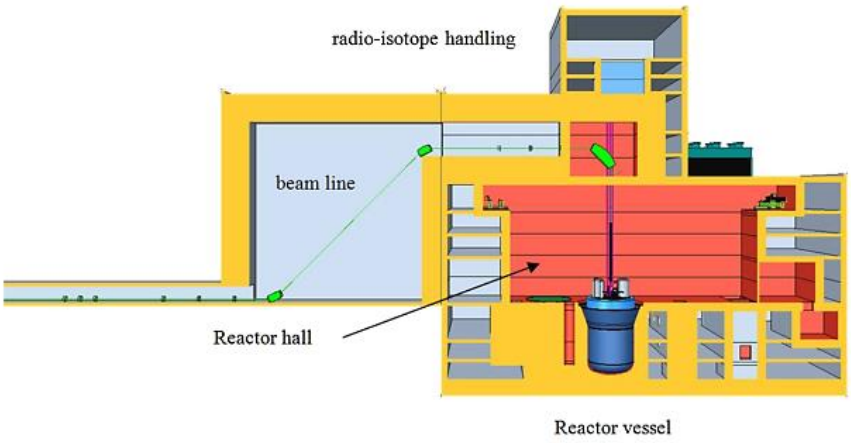

Figure 2.7: Vertical cross section of the MYRRHA building with the beam line entering the reactor vessel from above [22].

2.2.2.1 Cooling system

The reactor vessel is composed by an inner casing and an outer one which serves as secondary containment in case of breaks. Being of the pool-type category, the inner reactor vessel houses all the primary systems and so all the LBE inventory. A reactor cover closes the system from the top and supports all the in-vessel components, requiring to carry out the refuelling from below the core.

Inside the inner vessel (Figure 2.8) a diaphragm divides a hot LBE pool (upper part) from a cold one (lower part), which are in communication thanks to two axial pumps. These pumps circulate the coolant inside the pool: the cold LBE from the lower pool heats up passing through the reactor core and enters the upper pool; here, two shell-and-tube, single-pass, counter-current type primary heat exchangers per pump cool down the LBE which finally returns to the colder region. The secondary side of the heat exchangers employs saturated water as a coolant: it enters from the top of the central channel into the lower dome; then, it reverses its motion entering the bundle tubes, heats up and evacuates again from the top.

The main features of MYRRHA facility are reported in Table 2.2.

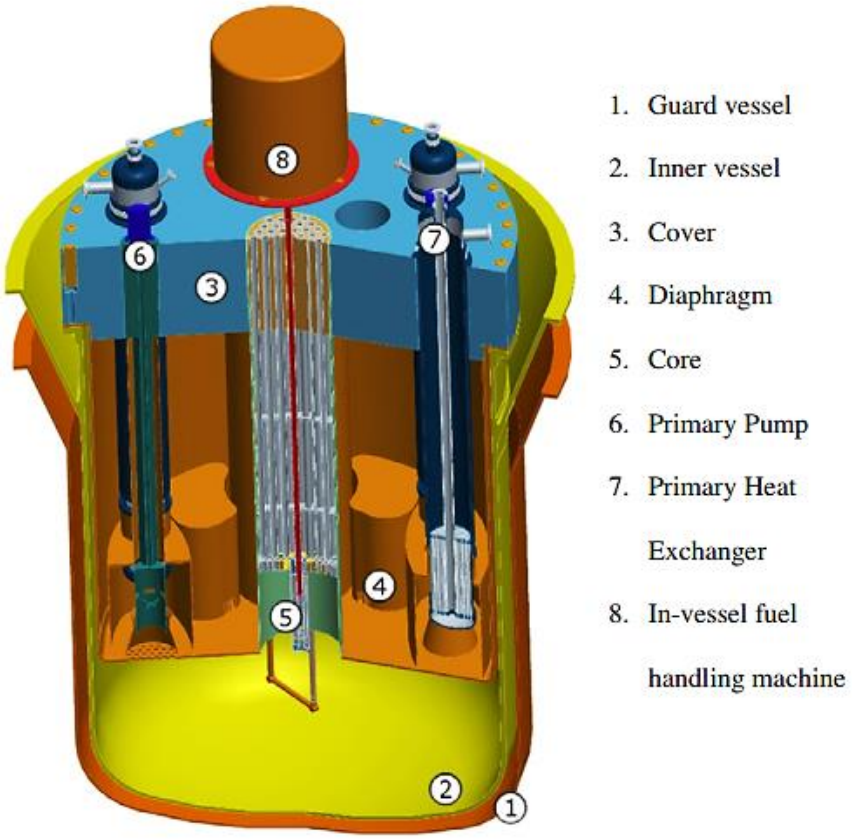

Figure 2.8: Vertical cut of MYRRHA reactor vessel [18].

Table 2.2: Main MYRRHA characteristics for accelerator, reactor and primary system [22].

Accelerator data	
Accelerated proton energy	600 MeV
Beam current[a]	3.2 mA
Reactor and primary system data	
Primary coolant	LBE
Secondary coolant	Saturated water/steam
Nominal power	100 MW_{th}
LBE mass inventory	4500 ton
Total primary mass flow rate	9500 kg/s
Average coolant velocity in core	2 m/s
Hot plenum temperature at full power	350 °C
Temperature of secondary coolant	200 °C
Total number of assemblies	151
Fuel pins per fuel assembly	127

[a] The proton beam current is the parameter to be tuned according to the desired reactor power: a higher current means that more spallation reactions take place inside the reactor core and so a greater amount of fissions is induced.

2.2.2.2 Reactor core

The MYRRHA core is constituted by fuel elements and other assemblies hosted during the operation depending on the core configuration (Figure 2.9). When the facility is set as ADS, the central position must accommodate the spallation target assembly which guides the proton beam into the centre of the core, inducing (p, n) reactions[12]. In addition, thirty-six in-pile test sections (IPSs) are present, allowing to perform experiments on materials inside a fast spectrum environment and to choose the desired neutron flux. In the critical configuration, instead, the spallation target is withdrawn whereas six control and three shutdown assemblies must be placed. All the remaining assemblies depicted in Figure 2.9 are dummy (serving as reflector) or fuel ones.

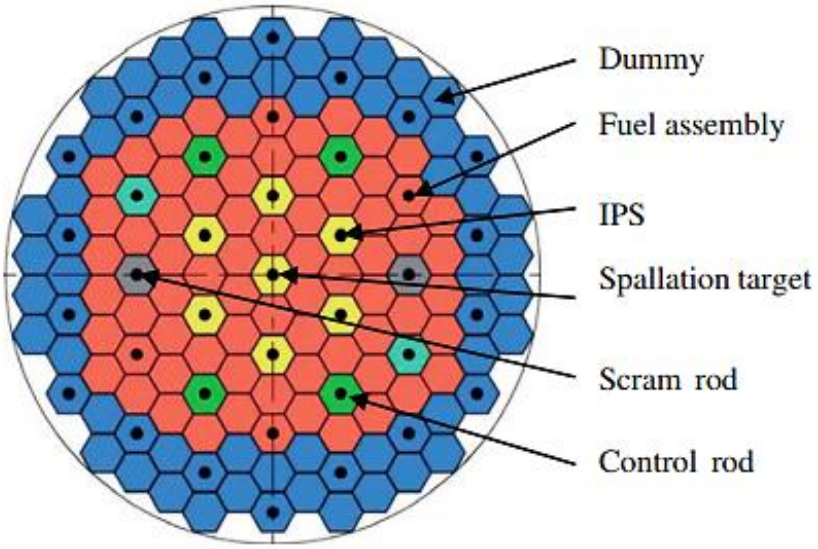

Figure 2.9: Assembly positions inside MYRRHA reactor; in-pile test sections (IPS) can be all those with an inside dot [18].

Fuel assemblies are constituted by a hexagonal bundle of 127 cylindrical fuel rods with a tight triangular arrangement, typical of fast reactors (while LWRs must optimize the fuel-to-moderator ratio to attain criticality, FRs do not need to moderate, thus the pitch can be reduced substantially). Each fuel assembly is encased and connected to an inlet and outlet nozzle to guide and control the LBE mass flow rate and to supply a continuum boundary during fuel handling.
Fuel rods are constituted by a stack of small diameter, U-Pu mixed oxide pellets (no blanket pellets are embedded), hosted by a support tube in the lower plenum and by a spring in the upper one and wounded by a spiral wire to keep them in place within the lattice. A below-core configuration is adopted to house the fission gases released by the fuel, with a comparable lower plenum and active fuel lengths (accounting for possible big releases induced by high fuel temperatures); on the contrary, the upper plenum is sensibly smaller[13]. As for the fuel, it is featured by 95%

[12] The spallation target assembly suffers harsher conditions with respect to fuel ones: severe heat and dose loads are induced by spallation reactions and by accelerated protons as well. The assembly, hence, must be designed to withstand such big doses and to efficiently remove the heat.
[13] Such configuration entails that fission gases accumulate to a larger extent in the colder region, allowing to limit the pin inner pressure.

theoretical density, an oxygen-to-metal ratio of 1.97 and it is 30% enriched in plutonium (required by the lower fission cross section at high energies), whereas the remaining uranium has the natural isotopic composition. Finally, a steel cladding is employed, but more details are provided in the next chapter, addressing the cladding material itself.
A schematic view of the fuel assembly structure is depicted in Figure 2.10. Table 2.3 and Table 2.4, instead, report fuel and geometrical characteristics of MYRRHA fuel pins.

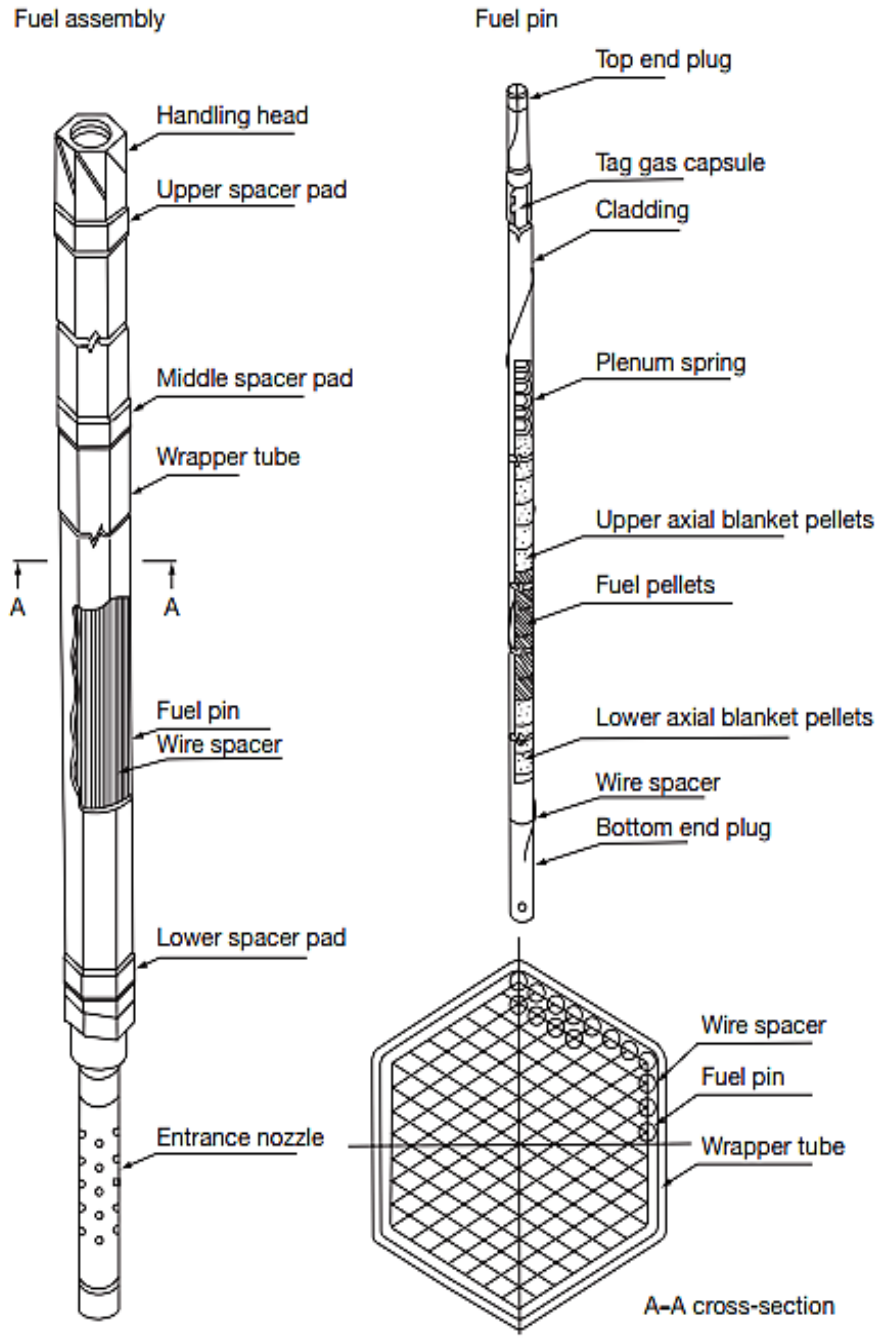

Figure 2.10: Fuel pin and fuel assembly for a typical liquid metal fast breeder reactor [1].

Table 2.3: Isotopic composition of fuel constituents [13].

Plutonium (weight %)	
^{238}Pu	0.23%
^{239}Pu	67.87%
^{240}Pu	26.07%
^{241}Pu	4.62%
^{242}Pu	1.2%
Uranium (weight %)	
Natural isotopic composition	
^{238}U	99.289%
^{235}U	0.711%

Table 2.4: MYRRHA fuel pin data [13].

Geometry	
Active fuel length	640 mm
Lower plenum length	580 mm
Upper plenum length	60 mm
Upper plenum volume	≈14500 mm^3
Fraction of volume occupied by the spring	0.3
Fuel outer diameter	5.42 mm
Cladding inner diameter	5.65 mm
Cladding outer diameter	6.55 mm
Pin pitch	8.4 mm
Fill gas initial pressure (He)	0.1 MPa
Fuel characteristics	
Fuel type	MOX
O/M ratio	1.97
Pu/M enrichment	0.3
U/M ratio	0.7
Fuel grain size	15 µm
Porosity	5%

Chapter 3

Review of 15-15Ti steel properties for MYRRHA cladding

To assess the thermo-mechanical performance of a fuel pin in a reliable way, correct physical models and experimental correlations are necessary, and they must refer to the specific materials employed in the design.

In the present chapter, the thorny topic regarding the cladding material for MYRRHA reactor is treated. In Section 3.1, the reasons leading to the choice of the DIN1.4970 steel, being part of the double stabilized 15-15Ti austenitic stainless steels family, are explained. The focus, then, shifts towards the development of a new version of the TRANSURANUS code addressed to the simulation of MYRRHA fuel pin performance: given that the starting *v1m1j18* code version contains many correlations developed for the *extended PoliMi* version and directed to AIM1 (a 15-15Ti steel employed by ALFRED reactor) not all the material properties are reviewed. In particular, only those which are most affected by the content of minor alloying elements and which play a crucial role in the fuel performance (i.e., creep and swelling) are investigated. On the other hand, thermo-mechanical properties, which are not very influenced by their content, are not examined, apart from yield stress and rupture strain.

As a first step, the correlations already implemented inside the *v1m1j18* version of TRANSURANUS code and referring to the properties and material of interest are reported in Section 3.2. Then, in Section 3.3, data found in the open literature are compared with TRANSURANUS models and are elaborated to improve the existing version of the code, allowing the treatment of DIN1.4970 austenitic stainless steel. The last step is the implementation of the new correlations, as described in Section 3.4.

The outcome of this part of the work is essential to simulate the MYRRHA fuel pin thermo-mechanical performance.

3.1 Introduction on cladding materials

The fuel rod cladding is one of the most important components to take care of inside a nuclear reactor core: it provides the basic structural integrity of the fuel rod itself and segregates fission gases, preventing their leakage into the primary coolant. It could be considered as the plant first safety barrier, given that it constitutes a physical separation between the fuel and the coolant; their contact, in addition to cause an increase in the coolant radioisotope inventory due to dispersion of fission products, could even lead to violent and undesired reactions depending on the two materials (this is one of the reasons justifying the adoption of an oxide fuel by LWRs).

The cladding tightness is put to a severe test during irradiation, owing to a large number of phenomena happening with increasing burnup: mechanical stresses due to internal and external pressure, thermal stresses due to temperature gradient, thermal expansion, thermal and irradiation creep, void swelling, helium swelling and embrittlement, neutron embrittlement, fuel-cladding mechanical and chemical interactions (FCMI and FCCI respectively), potential liquid metal embrittlement. All them have a detrimental effect on cladding structural stability and integrity: some may cause its collapse, other may induce deformations leading to an unacceptable geometry. Moreover, some phenomena are often enhanced by the effects of the others, triggering potentially dangerous feedback mechanisms (primarily thermal).

In light of its key safety role, the choice of a proper cladding material is crucial in order to avoid rapid deterioration and rupture, leading to release of radioactive fission products to the reactor environment. In this regard, the typical core material requirements hold [23]:

- Minimum interference with neutron population;
- Dimensional stability under irradiation and applied stress (irradiation creep and swelling);
- Acceptable mechanical properties even after ageing under neutron exposure;
- Low activation features to facilitate disposal and maintenance;
- Compatibility with other components (i.e., with the coolant);
- Cost of fabrication and assembly.

Finding the best compromise between these selection criteria is not an easy task, especially considering cladding conditions: the proximity to the fuel, indeed, exacerbates all the material loadings, making more difficult to fullfill all the requirements.

A comparison between the possible material options suitable for FRs is briefly discussed below, followed by a more detailed analysis on the final choice adopted for the MYRRHA facility.

3.1.1 Cladding material for fast reactors

Despite the decades of experience gained through the operation of LWRs, the selection of a cladding material for FRs must face new challenges, originating from the harsher irradiation environment in terms of reactor power rates and prolonged exposure to fast neutrons (factors becoming even more challenging owing to the high burnup requested by FRs for economic reasons [14]), and the necessity to interfere as little as possible with the neutron population: new materials must be specifically tested and licensed.

[14] Both SFRs and LFRs aim at reaching a peak linear power close to 400-500 W/cm, against the 200 W/cm for LWRs. Furthermore, a burnup of the order of 120 MWd/kg (12 at.%) is the objective of FRs; as a frame of reference, fuel in a standard LWR reaches an average burnup of 45-55 MWd/kg (4.5-5.5 at.%)[4].

First of all, a material with a low neutron capture cross section in the fast energy region is desirable, allowing to withstand the required fast neutron flux conditions. As it could be seen from Table 3.1, such prerequisite immediately makes Zircaloy, the historically employed LWR cladding material, unattractive[15]. Instead, the cladding material choice for FRs typically falls on steels.

Table 3.1: Neutron capture cross sections for typical metals [4].

Metal	σ_c (100 keV) [mb]	σ_c (thermal) [mb]
Ti	6	5.8
Fe	6.1	2.53
Cr	6.8	3.1
V	9.5	15.1
Si	10.0	0.16
Co	11.5	37.0
Ni	12.6	4.8
Zr	15.1	0.18
Cu	24.9	3.77
Mn	25.6	13.2
Mo	71.0	2.7

Once neutronic requirements have been fulfilled, temperatures up to 600 °C and fast neutron fluences of the order of 10^{23} cm^{-2} must be faced. The problem shifts to the selection between an austenitic stainless steel and a ferritic-martensitic one. Although both are steels, the different microstructure (face centred cubic for austenitic stainless steels versus body centred cubic for ferritic-martensitic ones) makes their behaviour totally different. As for the previously mentioned loadings and phenomena featuring the cladding, the following qualitative rules hold:

- Ferritic-martensitic steels suffer more the embrittlement caused by neutron irradiation with respect to austenitic steels;
- Ferritic-martensitic steels develop lower thermal stresses than austenitic steels at equal geometry and linear power, owing to the generally higher thermal conductivity;
- Ferritic-martensitic steels are more susceptible to thermal creep than austenitic steels, but resist more to irradiation creep;
- Ferritic-martensitic steels show a significantly lower void swelling effect with respect to austenitic steels;
- Ferritic-martensitic steels exhibit less He-swelling and embrittlement than austenitic steels thanks to their lower Ni and Cr content (being the principal players of (n, α) reactions);
- Ferritic-martensitic steels suffer less liquid metal corrosion and internal cladding corrosion (FCCI) than austenitic steels.

[15] Another reason why Zircaloy cannot be employed for fast spectrum reactors is related to its insufficient strength at high temperatures, both from the mechanical and the integrity point of view. Above 350 °C, indeed, the break-away phenomenon displays: the oxide layer (ZrO_2) which typically forms on the outer cladding surface changes microstructure becoming more porous. In LWRs, this means allowing water to reach the metal surface carrying on corrosion reactions; in LMFBRs, instead, it would mean to give the possibility for alloying elements to continue the dissolution process towards the liquid metal coolant.

From the number of advantageous features, it seems that ferritic-martensitic steels should be the best choice for FRs and, hence, they should be the first current candidates to be adopted as cladding material. As a matter of fact, however, the material response to creep and swelling (the most important cladding features) supports both the opposite alternatives, making the individuation of the best one not straightforward.

As far as swelling is concerned, austenitic steels typically exhibit a consistent swelling effect (both in terms of duration of the incubation period and in terms of steady-state swelling rate), turning out to be their principal weak point: geometrical constraints and the loss of mechanical ductility[16] limit so much the burnup that the fast reactor economic objectives cannot be pursued anymore. Cladding deformation due to swelling, indeed, has always been the main limiting factor for the performance of fuel pins adopting austenitic stainless steels [1]. Ferritic-martensitic steels, on the other hand, display an outstanding resistance to void swelling: their incubation period is so high that it would not be a problem to reach the 180 dpa burnup goal, at least as far as swelling is concerned. A comparison between the swelling behaviour of the two steels is reported in Figure 3.1: it is undeniable how austenitic steels (i.e., AISI 316 and 15-15Ti) are more sensitive to swelling enlargement than ferritic-martensitic ones.

Nevertheless, austenitic steels are preferred for high temperature applications (as Generation IV systems in general) because of their better behaviour in terms of thermal creep and creep fatigue [23]. Such statement is valid all the more whether LMFBRs are of interest, given that the major stress in their cladding arises from the progressive inner pressurization due to fission gas release, leading to an additional contribution to the gradual fuel pin outer diameter increment.

Material compatibility

Another key issue to be considered when selecting the cladding material is material compatibility, especially adopting a liquid metal coolant such as lead or LBE. Three are the main mechanisms to be faced: general corrosion, thermal gradient induced mass transfer and liquid metal embrittlement (LME).

General corrosion is due to a non-negligible solubility in lead alloys of typical steel components such as Fe, Mn and especially Ni, causing a severe dissolution mechanism [24]: the principal effect is a material loss which may compromise the cladding structural integrity. Possible countermeasures are the adoption of a proper coating layer on the outer cladding surface or to blend alloying elements such as Si, Cr and Al able to promote the formation of a protective oxide stratum[17].

[16] An excessive swelling deformation alters so much the steel microstructure to become a further contributor to cladding embrittlement: as an example, a 6% volumetric swelling increment has turned out to be a valid threshold for 15-15Ti austenitic stainless steels [71], treated in details in Section 3.1.2. Once the embrittlement limit is reached, a further exposition to neutron irradiation results in the so-called "channel fracture", a non-ductile type of failure which has been observed in austenitic steels at volumetric swelling values in excess of 10% [25][72].

[17] To command the protective self-healing phenomenon, an active oxygen control mechanism was implemented in Russian LBE-cooled nuclear reactors (the first to note and to oppose the problem), consisting in the oxygen content monitoring inside the coolant to avoid a too low concentration, which prevents the development of an efficient oxide layer, but also to avoid the formation of a too thick wall, hindering the heat transfer from the fuel to the coolant.

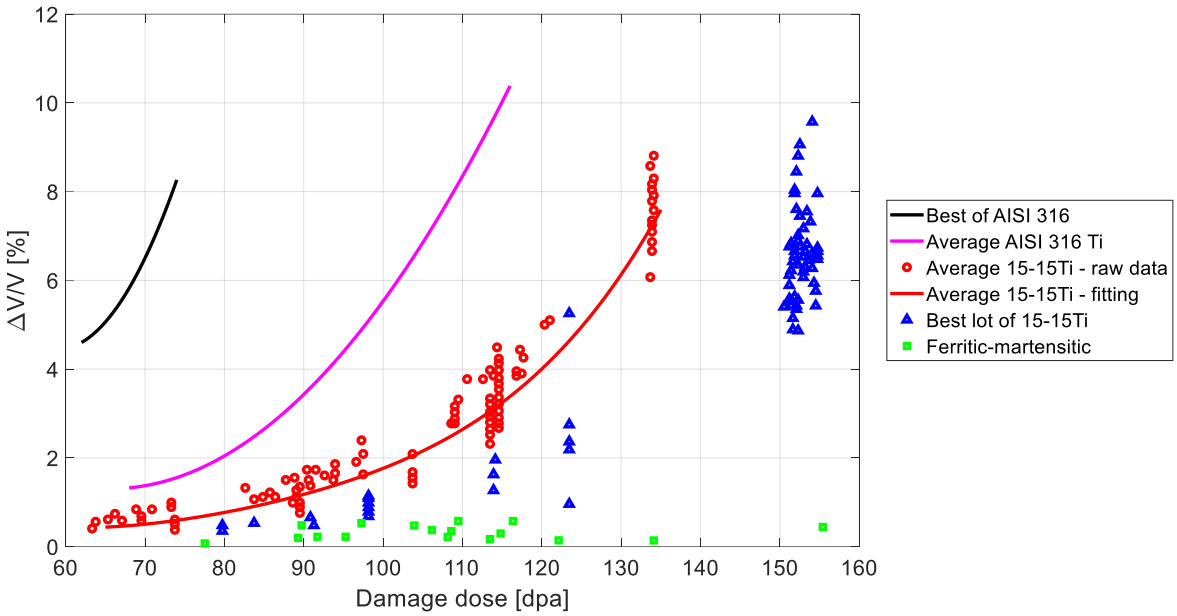

Figure 3.1: Comparison between the swelling effect on austenitic stainless steels (Phénix) and ferritic-martensitic steels [23].

Thermal gradient induced mass transfer originates from the previous problem, despite the consequences are not the same. Owing to temperature differences existing between distant regions inside the reactor, non-uniform dissolution mechanisms are triggered: it is possible to dissolve more where temperature is higher and to redeposit where temperature decreases, causing a transfer of mass able to block the coolant flow. Historically, such issue has unveiled to be the primary concern in liquid metal systems.

The third mechanism is the most unclear and debated [25]: when a normally ductile steel gets in contact with liquid lead (or LBE), a loss of ductility for the steel itself takes place, even resulting in a brittle fracture [17]. Such material behaviour was studied performing creep tests in air or in lead [26], showing that steel specimens tested in lead came to rupture with a final creep strain lower than the one obtained in air at a lower stress (but at the same temperature), a trend which is unusual (the rupture strain should be higher at higher stresses). This means that the specimen has suffered an embrittlement staying in contact with the liquid metal.

Despite the physical processes behind the three corrosion mechanisms have been understood, current qualified materials are able to withstand just the flow conditions of the past Russian reactors: a significant amount of R&D is still necessary to obtain a cladding material capable to survive for a long time in the liquid metal environment of future LMFBRs [24].

3.1.2 MYRRHA cladding material: DIN1.4970

3.1.2.1 Double stabilized austenitic stainless steels 15-15Ti

Among the two material possibilities previously discussed, austenitic stainless steels have been typically preferred to ferritic-martensitic ones as cladding material in Generation IV reactors as well as in MYRRHA facility [14], meaning that their excellent mechanical behaviour at high temperature wins over their swelling weakness[18].

The high swelling suffered by austenitic steels has been partially solved with the development of double stabilized 15-15Ti steels: TiC precipitates, together with other minor alloying elements (such as Si), allow improving a lot the swelling resistance (besides the improvement of high temperature mechanical properties)[27]. Vacancies and interstitials (the fundamental players of void swelling), indeed, remain trapped at the precipitate outer surface and are unable to escape unless an opposite point defect annihilates the blocked one [28]; in this way, the number of point defects capable to join is drastically reduced, limiting the volumetric growth.

Additionally, if cold work manufacturing is carried out, the austenitic stainless steel swelling endurance grows further: the increased density of the dislocation network raises the sink term of point defects, since their interaction is able to decrease the local lattice stress state near the dislocation itself [28]. Being trapped, vacancies and interstitials can hardly collect, reducing the swelling effect. For this reason, double-stabilized 15-15Ti austenitic stainless steels are usually cold-worked at around 15-20%.

Several versions of 15-15Ti austenitic stainless steel have been developed over the years, differing each other for the content of minor alloying elements. The principal ones are the French AIM1, the Japanese JPCA/PNC316, DIN1.4970 developed by the DeBeNe (German-Belgian-Netherlands) consortium and D9 by US. The maximum dose for safe operation of fuel pins employing such steels (in a cold-worked form) is limited to 120-130 dpa for excessive swelling embrittlement [23][27], significantly lower than the upper limit offered by ferritic-martensitic steels but substantial.

The following section deals in detail with the precise 15-15Ti steel version adopted as cladding material for MYRRHA reactor.

3.1.2.2 DIN1.4970

The cladding material choice to be applied in MYRRHA facility was driven by the necessity to have the reactor working within 2036. Starting from this requirement, only industrially available and qualified options were considered. Based on available data on mechanical properties, irradiation performance, fabricability and availability, the 15-15Ti steel version developed by the DeBeNe consortium, the cold-worked DIN1.4970, was finally selected as first core cladding material [14].

Double stabilized 15-15Ti has been extensively used in SFRs and various data are even public, whereas for other promising steels like the ferritic T91 one, long term irradiation experiments are still ongoing. Hence, T91 ferritic steel, which seems to have great properties concerning both

[18] Being the class of materials which are deeply analysed in the following, a review is carried out about the meaning of their name. First of all, they are “steels” because the C content is typically between 0.03% and 0.15%. Then, “austenitic” means that they have a face-centred cubic crystal lattice, which is the natural structure of iron between 910-1400 °C, and this structure is stabilized at room temperature adding Ni to the alloy. Finally, they are “stainless” because they contain high quantities of Cr (>13%), providing surface passivation for corrosion resistance.

swelling and creep (with the last one being the historical weak point of ferritic-martensitic steels), was chosen, for the moment, just for components who suffer minor neutron exposure (e.g., core support plate – see Table 3.2). The availability of data, especially concerning long-term exposure to fast neutrons, was one of the most important argument to select the steel for the fuel cladding in MYRRHA reactor.

The last obstacle to tackle before the adoption of DIN1.4970 steel in MYRRHA, remains the interaction with the harsh LBE environment, causing corrosion and liquid-metal embrittlement. The existing experimental data seem promising, but they are not enough to assess the problem in MYRRHA conditions and for long exposure times, so additional dedicated experiments are necessary. In any case, an active oxygen control for the coolant will be certainly implemented to handle the problem.

In conclusion, it has been previously said that 15-15Ti steels limit the fuel pin exploitation to doses belonging to the range 120-130 dpa. This means that, whether higher burnups would be achieved, the cladding material should be substituted: current previsions affirm that the next MYRRHA cores will rely either on T91 ferritic steel or on ferritic oxide-dispersion strengthened (ODS) alloys, since ferritic-martensitic steels seem to be the only way to achieve doses as high as 180 dpa [23]. However, the first ones require further assessment on their endurance under neutron irradiation, whereas the others show limitations in terms of internal corrosion, difficult fabrication and too limited experience.

Table 3.2: Selection of MYRRHA materials for major components [14].

Component	Material	Temperature range [°C]	Damage dose at end life [dpa]	Minimum lifetime
Vessel	316L	200-270	$<10^{-3}$	40 years
Core support plate	T91	200-460	~17	10 years
Assembly wrapper	T91	235-420	~60/90	3 years
Cladding	DIN1.4970	235-470	~60/90	3 years

Composition

DIN1.4970 steel pertains to the double stabilized 15-15Ti austenitic stainless steel family, thus it is characterized by a percentage of Ni and Cr around 15% and an amount of Ti around 0.5%. The content of major alloying elements (those ones with the highest percentage) establishes the thermo-mechanical behaviour of 15-15Ti steel family, whereas the one of minor alloying elements does not influence them, but rather the material response to fundamental phenomena such as creep and swelling. It is the last characteristic (i.e., the minor alloying elements content) which discriminates among the possible 15-15Ti steel versions (DIN1.4970, AIM1, D9 and so on).

In the following, unless otherwise specified, DIN1.4970 steel with the composition reported in Table 3.3 will be considered. Note that the percentage of alloying elements can slightly vary within this version of the steel. However, fluctuations should be sufficiently small not to transform DIN1.4970 into another 15-15Ti steel version (i.e., to keep the steel creep and swelling characteristics almost unaltered). The reference state of the steel, moreover, is 20% cold-worked, being crucial in the definition of the void swelling resistance.

Table 3.3: Chemical composition of DIN1.4970 alloy [27]

Element	weight %
B	0.0030-0.0080
C	0.080-0.120
Ca	<0.010
Co	<0.030
Cr	14.5-15.5
Cu	<0.050
Mn	<2.0
Mo	1.0-1.4
N	<0.015
Nb	-
Ni	14.5-15.5
P	<0.015
S	<0.015
Si	0.3-0.6
Ti	0.3-0.55
Ta	<0.02
V	<0.05
Fe	~66.0

3.1.3 Aim of the review

The analysis of MYRRHA fuel pin performance is carried out in this work by means of the integral fuel performance code TRANSURANUS. The reference *v1m1j18* version of the code embeds some of the correlations which were developed inside the so-called *extended PoliMi* version [29] (created starting from TRANSURANUS *v1m1j14*) with the aim to perform the thermo-mechanical analysis of ALFRED reactor, adopting lead as coolant instead of LBE and AIM1 as cladding material in place of DIN1.4970.

Objective of the present part of the thesis work is to review the correlations already implemented in the reference version of TRANSURANUS code, exploiting data obtained from open literature to evaluate possible updates. In particular, final aim is to draw up new correlations addressed to MYRRHA cladding simulation, allowing a more reliable assessment of its fuel pin performance. Hence, data research in the literature is directed towards DIN1.4970 austenitic stainless steel, whereas the correlations and models already included inside the reference TRANSURANUS code version will be exploited to evaluate fuel and coolant behaviours.

Not all the cladding material properties are reviewed. In order to understand the rationale of the choice, a fundamental aspect should be recalled: minor alloying elements play a crucial role in determining the material response to creep and swelling, whereas they have a limited influence on thermo-mechanical properties (i.e., all the steels pertaining to the 15-15Ti family have the same behaviour)[30]. This is relevant because some of the starting *v1m1j18* models refer to AIM1, which belongs to 15-15Ti steel family but differs from DIN1.4970 for the content of minor alloying elements.

Accordingly, as for thermo-mechanical properties, the correlations already implemented in the TRANSURANUS code are maintained. Furthermore, they were subjected to validation by *Sobolev* [31], revealing that they fall within his error band, so there are no reasons to make further investigations. The only exceptions being for yield stress and rupture strain which disagree with Sobolev models: for such reason, these material properties are re-examined.
Creep (both thermal and due to irradiation) and void swelling behaviour, on the other hand, are deeply analysed. These phenomena have the most important role in determining the evolution of the cladding geometry, so of temperatures and mechanical loads[19]. Moreover, despite the importance to accurately evaluate the material behaviour under conditions similar to the one it will face inside the reactor core, few data are currently available for such phenomena, hence uncertainties are still big (particularly concerning creep models for low stress and temperature conditions, owing to the long time required to perform tests). The centrality in the fuel pin performance, joint to high uncertainties on data, have been the primary reasons leading to the choice of the material properties to focus on.

3.2 *v1m1j18* TRANSURANUS version

In the following, the cladding correlations of interest for this work and that are part of the starting *v1m1j18* version of TRANSURANUS code are presented.
The next step is the construction of new models based on data found in the open literature to cover the deficiencies of this initial version of the code, which is the topic of Section 3.3.

3.2.1 Thermal creep

The *v1m1j18* version of TRANSURANUS code allows predicting the thermal creep behaviour of AIM1 steel and of DIN1.4970 as well. Here below, only the correlations addressed to DIN1.4970 steel both for the creep strain rate calculation and for the evaluation of the time-to-rupture to compute the cladding cumulative damage function are discussed, being the cladding steel of interest for MYRRHA.

3.2.1.1 Creep strain rate

The *Többe* correlation [32] applies: a Nabarro-Herring structure (a temperature dependence inside an exponential and a hyperbolic sine) discriminates it from the typical Arrhenius-type equation (just the exponential dependence on temperature). The presence of TiC precipitates (commensurate with point defects), indeed, tends to produce a creep mechanism comparable to diffusional creep already at low temperatures and such creep mechanism is exactly modelled with the Nabarro-Herring equation.

[19] Both creep and swelling have a crucial influence on the fuel pin gap dynamics. Especially for irradiation creep and swelling, indeed, the MYRRHA fast reactor conditions (i.e., the prolonged exposure to fast neutrons) enlarge them dramatically, whereas they were just of secondary importance in LWRs.
Not only, creep has also a strong influence on the stress suffered by cladding when the gap closes and the cladding itself starts working under imposed deformation (by the fuel pellet). In such situation, creep stress relaxation contributes to relieve the cladding stress, influencing positively the problems related to FCMI.

Többe correlation (thermal creep) [32]	$\dot{\varepsilon}_{th}\ [h^{-1}] = 7.49\ 10^{13} \exp\left(-\frac{91000}{1.986\ T}\right) \sinh\left(\frac{57.46\ \sigma_{EQ}}{1.986\ T}\right)$ σ_{EQ} [MPa]: applied equivalent stress T [K]: temperature	(3.1)

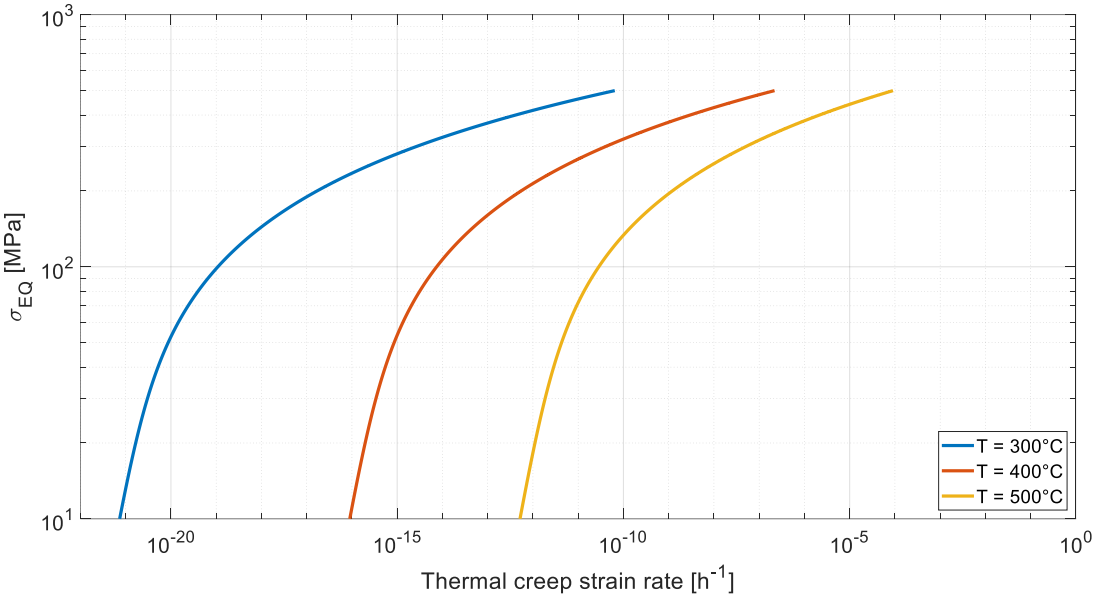

Figure 3.2: *Többe correlation* (thermal creep) for representative temperatures.

3.2.1.2 Cumulative damage function

A cumulative damage function approach is contained in TRANSURANUS to evaluate the cladding failure due to the action of creep [4]:

$$\text{CDF}\ [/] = \sum_i \frac{\Delta t_i}{t_{R,i}} \tag{3.2}$$

Δt_i [h]: i-th timestep

$t_{R,i}$ [h]: time to rupture correspondent to the existent stress and temperature at the i-th timestep

when the CDF exceeds unity, it is assumed that the steel has accumulated enough strain to cause rupture. Nevertheless, although a CDF value smaller than one indicates that cladding does not fail because of thermal creep, generally a maximum value of 0.2–0.3 is considered acceptable [33].

The time-to-rupture in Equation (3.2) is computed through a time-temperature parameter approach. Usually, Larson-Miller (LM) parameter, acquired from a flow law of the Arrhenius type, is employed (see Equation (3.13).). Considering the creep mechanism of 15-15Ti steels, however, the P parameter defined starting from a Nabarro-Herring equation is exploited in TRANSURANUS *v1m1j18* because more physically correct [30].

The three required steps are the following: first of all, based on the applied stress, the time-temperature parameter is calculated through Equation (3.4) [30]; then, reversing the definition of the parameter itself in Equation (3.3) and known the temperature, the time-to-rupture is extracted and the CDF is updated.

P parameter correlation [30]	$P\,[/] = T \cdot \left(20 + \log \frac{t_R}{T}\right)$ $T\,[K]\,, t_R\,[h]$	(3.3)
	$P = \begin{cases} 0.01892153\,\sigma_{EQ}^2 - 24.19134\,\sigma_{EQ} + 21761.81 & \sigma_{EQ} < 395MPa \\ -6.017016\,\sigma_{EQ} + 17535.01 & \sigma_{EQ} \geq 395MPa \end{cases}$	(3.4)

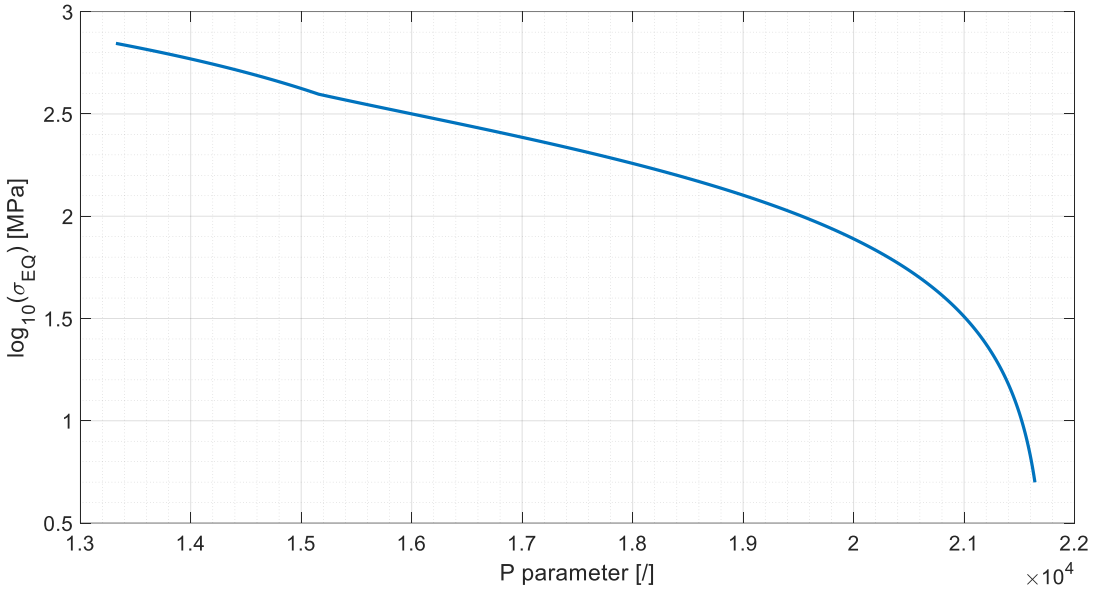

Figure 3.3: Relation between P parameter and applied stress to determine the time-to-rupture.

3.2.2 Irradiation creep

An irradiation creep model specifically addressed to DIN1.4970 is not contained inside the *v1m1j18* version of TRANSURANUS code.

A *Többe* correlation [32] for irradiation creep, developed for a generic 15-15Ti steel, is instead available in the code and models the creep strain rate as function of the applied stress and of the first power of the neutron flux. Because of the high uncertainty, the coupling of irradiation creep with swelling is not considered[20].

Többe correlation (irradiation creep) [32]	$\dot{\varepsilon}_{irr}\,[\,h^{-1}] = 3.2\;10^{-22}\;\bar{E}\;\phi\;\sigma_{EQ}$ σ_{EQ} [MPa]: applied equivalent stress $\bar{E}$ [MeV]: mean neutron energy ϕ [$cm^{-2}s^{-1}$]: neutron flux	(3.5)

[20] The coupling arises from the fact that swelling means precipitation of vacancies as voids, leaving an excess of interstitials within the lattice. This surplus is absorbed mainly by dislocations causing their climb around the obstacle [39]. The macroscopic effect turns out to be creep.

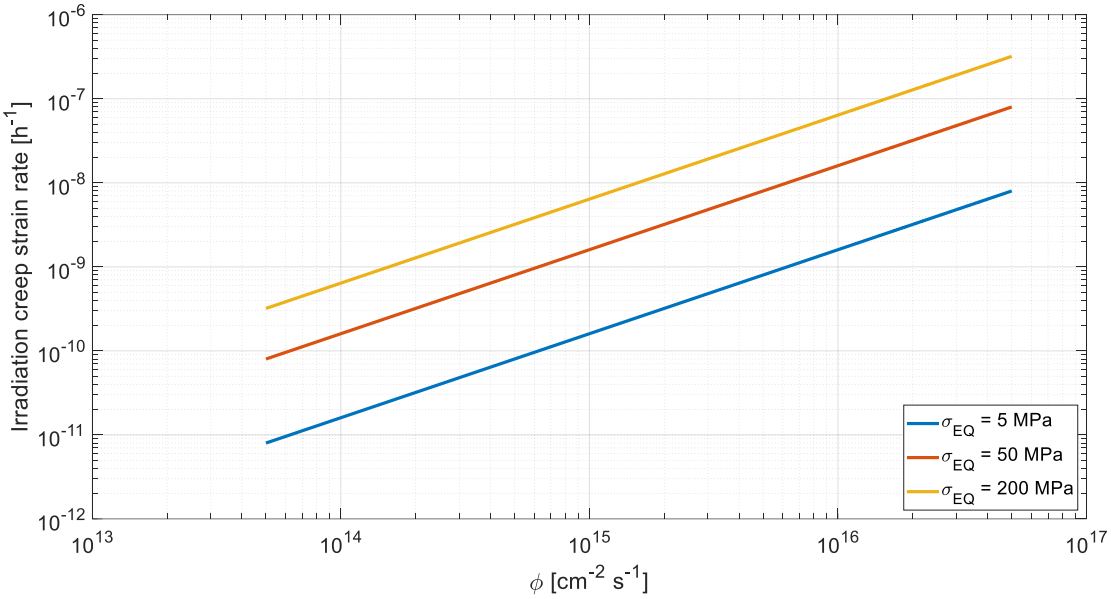

Figure 3.4: *Többe correlation* (irradiation creep) for representative stresses.

3.2.3 Void swelling

Void swelling is treated in TRANSURANUS *v1m1j18* through two correlations built on experimental data in [34], characterized by the typical dependence on temperature (which influences vacancy motion allowing them to join each other) and on fast neutron fluence (which is the driving force of the phenomenon).

Specifically, a model valid for AIM1 steel (*Specific AIM1*) is embedded and should be a best estimate formula to quantify the phenomenon; then, a model for a non-optimized, older version of the steel (*Generalized 15-15Ti*) should be able to provide a conservative estimation of the void swelling effect.

Actually, a correlation addressed to DIN1.4970 is not already implemented in the code.

Specific AIM1 [34]	$\frac{\Delta V}{V}\,[\%] = 1.3\ 10^{-5} \exp\left(-\left(\frac{T-490}{100}\right)^2\right)\left(\frac{\Phi}{10^{22}}\right)^{3.9}$ (3.6)
Generalized 15-15Ti [34]	$\frac{\Delta V}{V}\,[\%] = 1.5\ 10^{-3} \exp\left(-2.5\left(\frac{T-450}{100}\right)^2\right)\left(\frac{\Phi}{10^{22}}\right)^{2.75}$ (3.7)
	T [°C] Φ [cm^{-2}]: fast neutron fluence[21] (E > 0.1 MeV)

[21] The conversion factor between damage dose and fluence is equal to 2 10^{21} $dpa^{-1}cm^{-2}$.

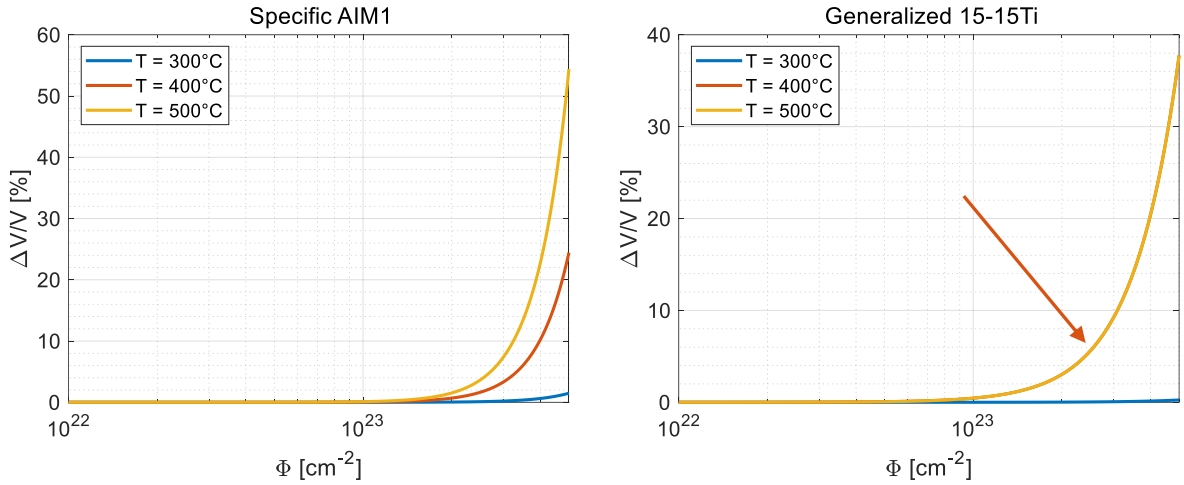

Figure 3.5: *Specific AIM1* and *Generalized 15-15Ti* correlations for representative temperatures.

3.2.4 Mechanical properties

As it has been said in Section 3.1.3, mechanical properties are deemed communal for any 15-15Ti steel, being the influence of minor alloying elements on them limited. Accordingly, the focus of the present review is just on such properties that were not in complete agreement with the *Sobolev* validation [31]. The little discrepancy might be attributed really to the different percentage of chemical elements [30].

Both correlations reported below were developed by *Többe* [32] and refer to a 20% cold-worked steel.

3.2.4.1 Yield stress

The following Equation (3.8) addresses unirradiated conditions[22]. It must be considered valid only below 1000 K, since the measured yield stress is higher than the ultimate tensile strength (which is calculated starting from the rupture strain) above such temperature, clearly an unphysical behaviour.

The comparison with *Sobolev* correlation is reported in Figure 3.6 (left).

Yield stress [32]	$\sigma_y\,[\mathrm{MPa}] = \begin{cases} 555.5 - 0.25\,T & T < 600\ °C \\ 405.5 - 0.775\,(T - 600) & 600\ °C < T < 1000\ °C \\ 345.5 - 0.25\,T & T > 1000\ °C \end{cases}$ $T\ [°C]$	(3.8)

[22] The reference version of TRANSURANUS does not take into account the effect of irradiation on mechanical properties.

3.2.4.2 Rupture strain

Rupture strain is the only mechanical property modelled in TRANSURANUS considering the effect of irradiation, through a constant value adopted when a threshold fluence is reached (Equation (3.9)).

The formula strongly disagrees with *Sobolev* (who assigns to the proposed rupture strain a 20% uncertainty) and it proves to be not conservative, as it can be appreciated from Figure 3.6 (right).

Rupture strain [32]	$\varepsilon_R\,[\%] = \begin{cases} 8 + 0.00474\,(\,T - 500\,) + 0.000062\,(\,T - 500\,)^2 & \Phi < 10^{22}\mathrm{cm}^{-2} \\ 6 & \Phi \geq 10^{22}\mathrm{cm}^{-2} \end{cases}$ T[°C]	(3.9)

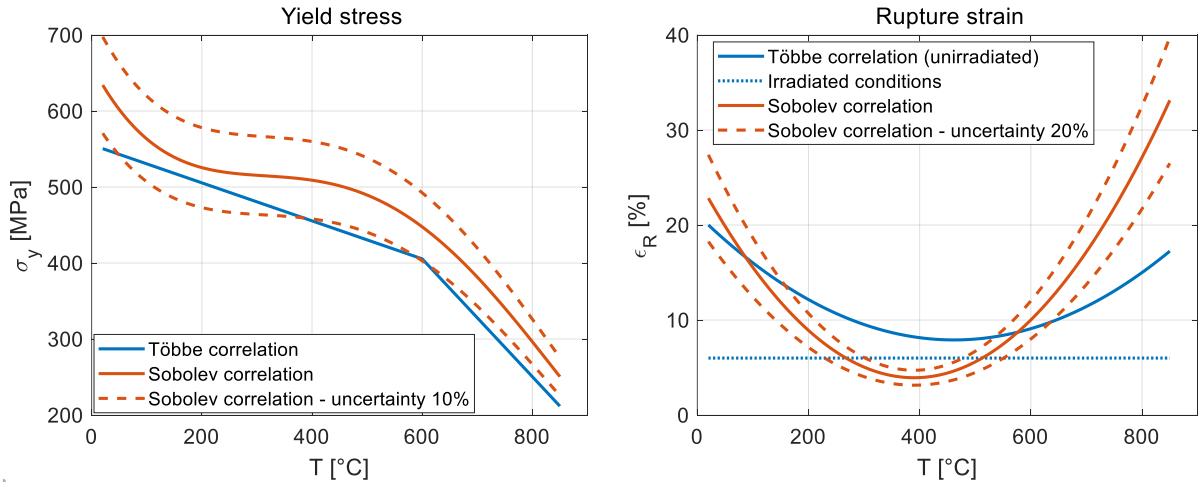

Figure 3.6: Comparison between *Többe* and *Sobolev* correlations for the mechanical properties of DIN1.4970.

3.3 Comparisons with literature data

3.3.1 Thermal creep

3.3.1.1 Creep strain rate

Results of creep tests on unirradiated DIN1.4970 cladding tubes performed by the DeBeNe consortium in the temperature range 600-750 °C were collected and processed in [27] to obtain suitable correlations to simulate their behaviour.

Two main families of mechanically treated tubes were tested during the experimental campaign:

- 1968-1980: annealed + cold-worked 15-25% + aged;
- 1975-1990: annealed + cold-worked 15-25%.

The reason of the subdivision is that aging was initially intended to allow secondary (very fine) TiC precipitation to take place (critical to improve creep properties). Later, it was found that such process occurred also under in-reactor conditions without initial aging and, moreover, the aging process worsens the swelling resistance of the material. The second part of the program, accordingly, focused on non-aged tubes, which remains the reference state for cladding tubes

today. Beyond the two big groups, tested tubes pertained to a lot of batches of the same steel, one different from the other in terms of annealing schedule, cold-working level, grain size, alloying elements and so on. Although the steel remains in principle the same, the affinity with a batch or another justifies the scatter in the dataset[23] (see Figure 3.7 and Figure 3.8).
Experimental creep strain rates were computed as the average value at 0.2% deformation[24]:

$$\dot{\varepsilon}_{th}\ [\%\ h^{-1}] = \frac{0.2\%}{t_{0.2\%}} \tag{3.10}$$

$t_{0.2\%}$ [h]: time needed to reach 0.2% deformation

With the aim of fitting the experimental data, three creep mechanisms were recognized exploiting the Ashby map and considering temperature and applied stress [35]. A power-law regime, described by the Norton law, dominates the dataset, dividing the experimental points in a first region with a stress exponent equal to 5 and a second region, at lower stresses, with stress exponent equal to 3; the large spread of data makes difficult to decide where transition occurs. At very high stresses (>200 MPa), then, the stress exponent is continuously increasing with the stress itself: a power-law breakdown (PLB) regime displays.
To overcome the obstacle arising from the spread of data joint to the changing stress exponent, a particular continuous function (Equation (3.11)) was selected to carry out the fitting: the stress dependence appears inside a hyperbolic sine (useful to deal with PLB), whereas temperature participates in an ostensible Arrhenius structure, given that the activation energy is a quadratic function of the temperature itself. The model coefficients were tuned on data just from the second part of the test program (non-aged tubes).

Original Delville correlation [27]	$\dot{\varepsilon}_{th}[h^{-1}] = \left(\sinh\left(\beta\ \sigma_{EQ}\right)\right)^{n} \exp\left(-\frac{E}{R\ T}\right)$ (3.11) $T[K], \sigma_{EQ}[MPa]$ R: universal gas constant $R = 8.314$ J/mol K E: activation energy $E\ [J/mol] = E_1 + E_2\ T + E_3\ T^2$ n [/]: stress exponent $n = 2.3319$ E_1, E_2, E_3, β: correlation coefficients $E_1 = -6.591\ 10^5$ J/mol $E_2 = 1.8211\ 10^3$ J/mol K $E_3 = -1.0513$ J/mol K^2 $\beta = 1.4994\ 10^{-2}\ MPa^{-1}$

Figure 3.7 shows the experimental dataset on which the *Original Delville* correlation was developed and the correlation itself. *Többe* correlation is reported on the same graph as well, displaying excellent predicting capabilities for the new dataset and good agreement with the

[23] The batch effect can be neglected, since it was observed that scatter within a single batch can be even larger than scatter between several batches.
[24] The instantaneous elastic deformation was subtracted but the primary creep strain was not, so data are overestimated.

Delville model especially at high stresses, whereas consistent differences may be observed at lower stresses.
Despite *Többe* correlation is already implemented inside TRANSURANUS code and its validity also for the new cloud of experimental points has been just confirmed, Equation (3.11) must be deemed equally reliable for such dataset, and hence applicable to predict the creep behaviour of DIN1.4970 steel.
Plotting the curves together at lower temperatures (i.e., 300-500 °C), a difference of many orders of magnitude has been discovered, with the *Original Delville* being very conservative (Figure 3.9). Moreover, whereas creep strain rates computed with the TRANSURANUS standard correlation continue to decrease as the temperature lowers (as expected), a strange behaviour can be noticed from the *Original Delville* correlation: at a temperature around 500 °C, the creep strain rate begins to slightly increase again. The reason of such trend is imputed to the polynomial shape expressing the activation energy as a function of temperature: when the temperature becomes too low, the first falls below zero[25]. Since final aim of the review is to contribute to the development of a new version of TRANSURANUS code suitable to be adopted for the simulation of MYRRHA fuel pins (designed to operate at low temperatures), the *Original Delville* model is judged not reliable for such a scope. Creep strain rate correlations, indeed, are typically extrapolated out of their validity range, being the creep experiments performed at high temperatures to accelerate the test.
In light of such considerations, a new correlation has been built: the structure of the *Original Delville* model has been preserved, except for the activation energy which has been assumed as a constant (since it is the contribution that makes the model weak at low temperatures), as it is valid for Arrhenius-type equations. The same dataset has been used, but both the cold-worked, non-aged specimens and the cold-worked, aged ones have been taken into account. The justification is to take advantage of the possibility to explore a wider dataset and this is legitimated since it has been observed that the aging process has a strong influence on swelling properties but not on creep ones.
The coefficients β, n, E have been taken as design variables and a least mean square optimization scheme has been employed, i.e., the sum of the square differences between model predictions and experimental data has been minimized. Those reported in Table 3.4 are the final outcomes of the optimization: the derived formula is named *Modified Delville* correlation.

Table 3.4: Optimized coefficients for the *Modified Delville* correlation.

Modified Delville correlation		
E [J/mol]	n [/]	β [MPa^{-1}]
1.2052 10^5	2.33189	0.01229

The standard deviation has been computed for the *Original Delville* correlation, *Többe* correlation and the new fitting to evaluate their ability to cover the experimental dataset. Equation (3.12) has been used for the calculation: the classical standard deviation definition has been modified

[25] The shape of the Original Delville correlation was chosen to fit at best the available data pertaining to a high temperature regime. Outside the region in which the correlation was developed, it is not astonishing to observe strange behaviours.

normalizing the square difference between the effective data and the prediction through the square of the true data itself. In this way, since data points are significantly spread, it is assured that every square difference weights equal, avoiding a major contribution to the error for the difference of those points which are bigger in absolute value.
The results are reported in Table 3.5. The comparison unveils that the *Modified Delville* model has an improved ability to cover experimental data with respect to the *Original Delville* one, hence its quality is satisfactory. Moreover, it has been built from a larger dataset, allowing the enclosure of more test cases. The *Többe* correlation, finally, proves to be even more accurate than the new one.

$$\sigma_{std} = \sqrt{\frac{\sum_i \left(\frac{\left(\dot{\varepsilon}_{exp,i} - \dot{\varepsilon}_{th,i}\right)^2}{\dot{\varepsilon}_{exp,i}^{\,2}} \right)}{N_{tot}}} \tag{3.12}$$

$\dot{\varepsilon}_{exp,i}$ $[h^{-1}]$: i-th experimental creep strain rate
$\dot{\varepsilon}_{th,i}$ $[h^{-1}]$: i-th theoretical creep strain rate
N_{tot}: number of dataset points

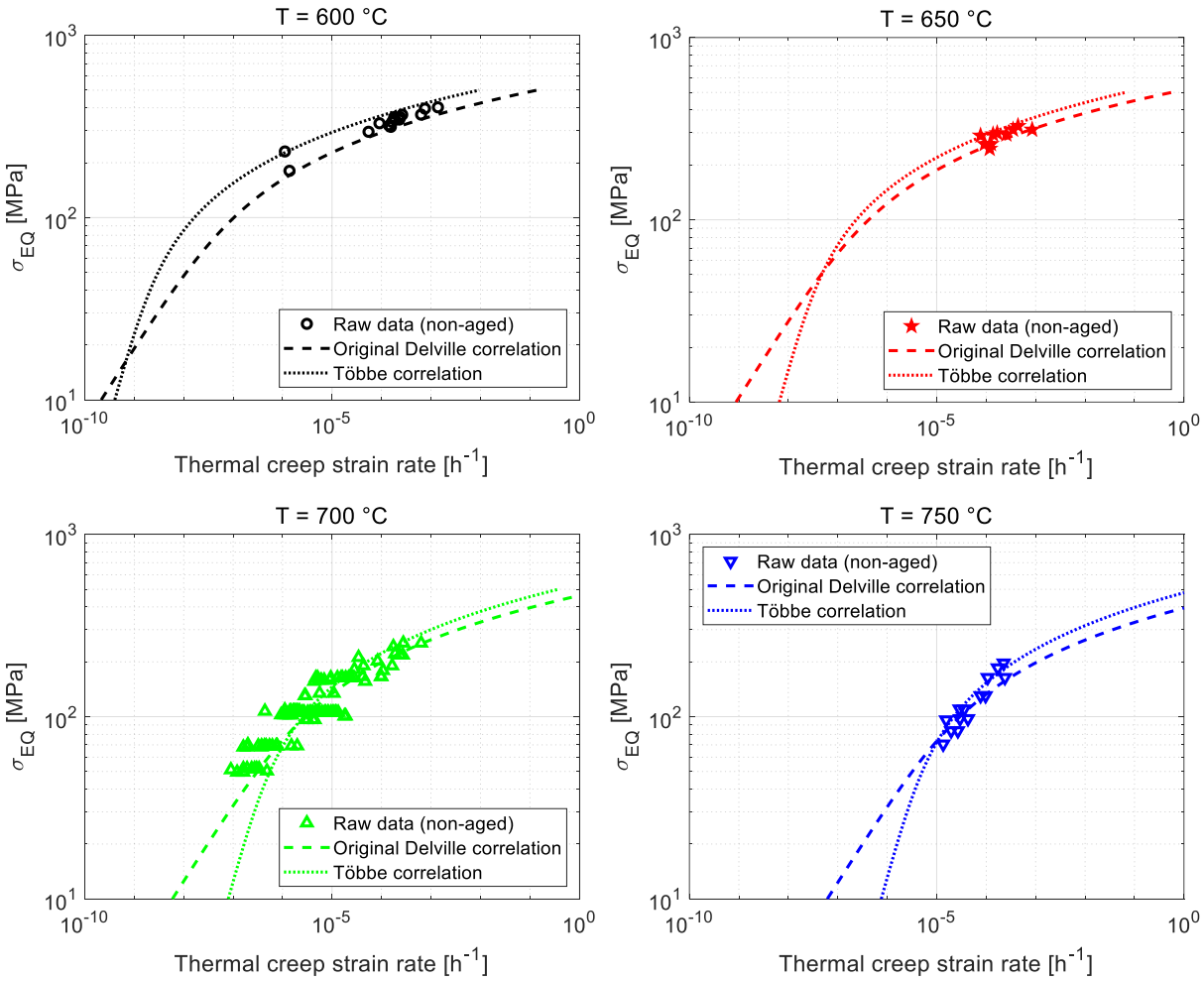

Figure 3.7: Comparison between *Többe* and *Original Delville* correlations on non-aged experimental data.

Table 3.5: Accuracy of *Többe*, *Original Delville* and *Modified Delville* correlations on experimental data.

Model	Standard deviation	Reference dataset
Original Delville correlation	0.3816	cold-worked, non-aged
Modified Delville correlation	0.3068	cold-worked, non-aged cold-worked, aged
Többe correlation	0.1952	cold-worked, non-aged cold-worked, aged

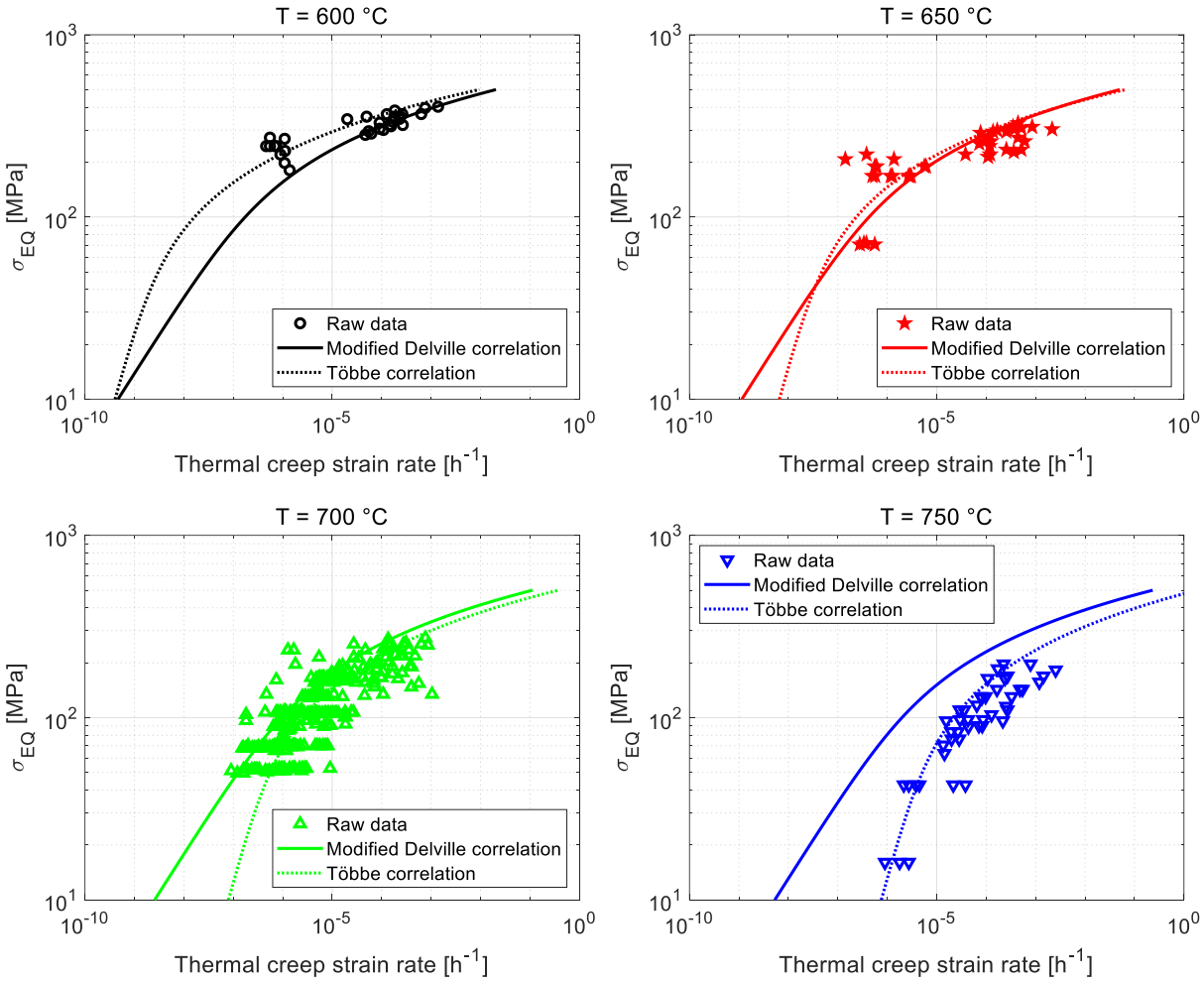

Figure 3.8: Comparison between *Többe* and *Modified Delville* correlations on aged and non-aged experimental data.

The assessment of the *Modified Delville* correlation against raw data (including both the non-aged and the aged ones) is reported in Figure 3.8 for some of the temperatures at which tests were performed; *Többe* model is shown as well, for the sake of comparison. In this respect, the *Modified Delville* formula better represents data at low temperatures, where it provides more conservative values of the thermal creep strain rate. Then, the additional dependence on temperature of the TRANSURANUS correlation (appearing as argument of the hyperbolic sine), allows it to supply more reliable predictions as the temperature itself grows up.

As for the low temperature regime, a comparison between the three models is shown in Figure 3.9. Note that no experimental data are present. This is because the three plots are made at out-range temperatures, where none of the three curves is applicable, in principle. However, the previously mentioned unphysical behaviour of the *Original Delville* correlation (confirmed by very high values of the creep strain rate even though the temperature is so low that creep should have a marginal contribution) is deemed as a sufficient reason to discard it for the MYRRHA fuel pin performance analysis. Considering just the *Többe* and the *Modified Delville* models, the difference between the curves is deep as the temperature goes down, whereas they are nearer towards the temperatures in which data are available.

For the purpose of the performance analysis for MYRRHA fuel pins, both the two models will be adopted in the following chapters. Indeed, even though the standard deviation for the *Többe* correlation testifies its better ability to represent the experimental data found, at low temperatures it is impossible to affirm which of the two is the correct expression for the creep behaviour. Given that the *Modified Delville* correlation provides more prudent estimations in this region, it is decided to exploit it for the performance analysis, requiring its implementation in the TRANSURANUS code.

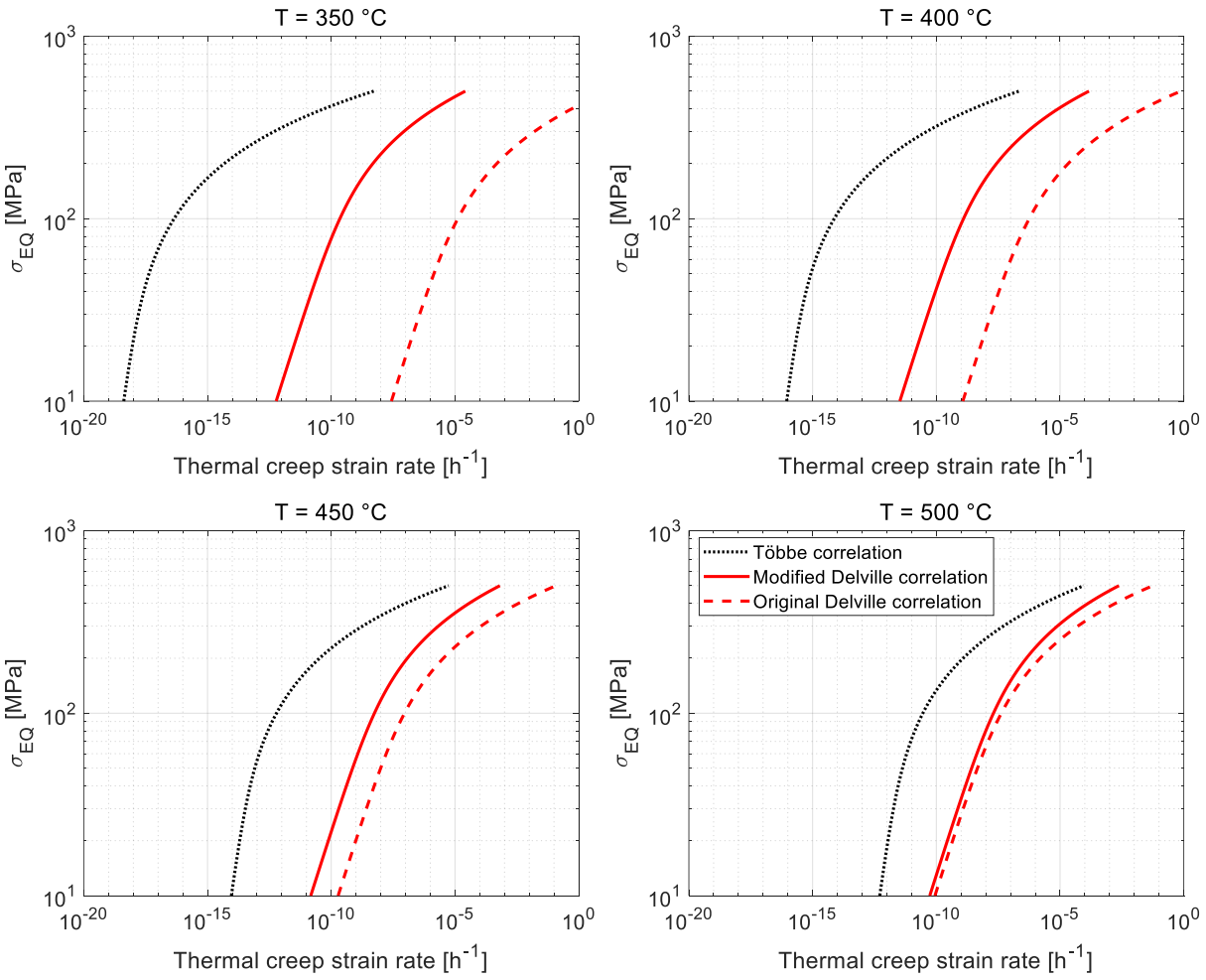

Figure 3.9: Comparison between *Többe*, *Modified Delville* and *Original Delville* correlations at representative low temperatures.

3.3.1.2 Cumulative damage function

Some of the creep trials performed by the DeBeNe consortium and used in Section 3.3.1.1 were continued until the specimen collapse to record the time-to-rupture, together with other dedicated tests at high temperature. Creep tests were performed also by Schroeder [36] to understand how He produced by (n, α) reactions inside the first wall and blanket of fusion reactors influences material properties. To simulate the irradiation conditions, fission reactors were used and the results were compared to unirradiated specimens (tested in conventional creep testing machines), with the latter being of interest for this review. The material under consideration was DIN1.4970, cold-worked at 13% and aged or just cold-worked. Yamamoto and Schroeder [37] performed similar tests on 13% cold-worked, non-aged DIN1.4970.
The slightly different degree of cold-working may cause some difference in creep resistance with respect to the standard 20% value; on the other hand, the aging process proved to be not so relevant on the creep behaviour, so data may be successfully treated together. Such two statements must be verified.

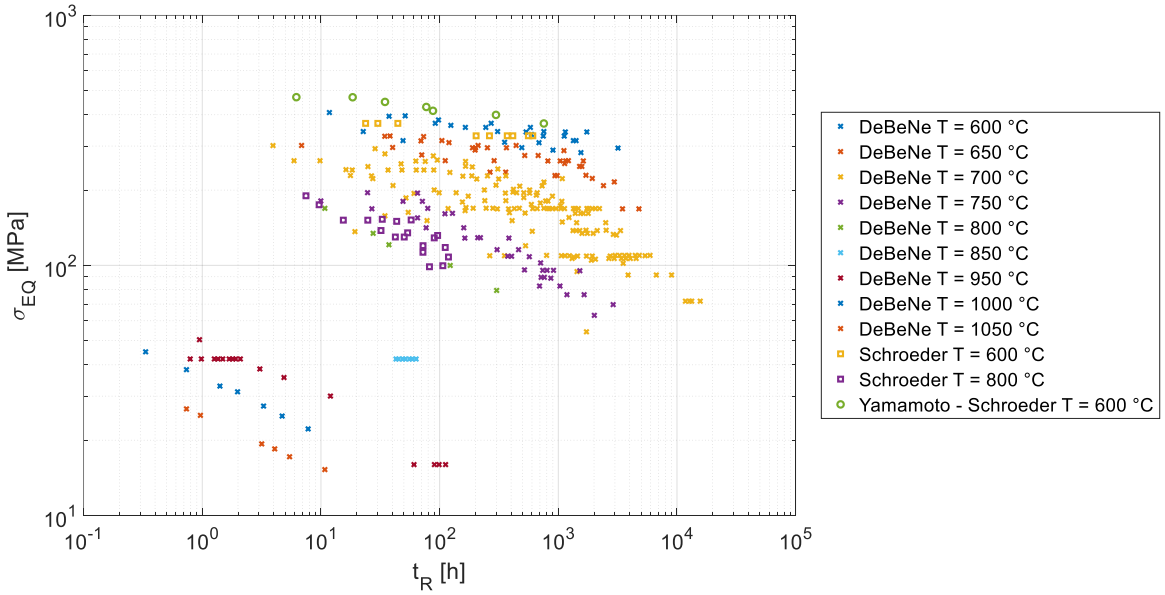

Figure 3.10: Experimental time-to-rupture data [27][36][37].

The experimental data are represented together in Figure 3.10. The most important observation which can be drawn from the graph is a confirmation of the correctness of treating aged and non-aged specimens together, since no differences are appreciable; the same could be said for the two degrees of cold-working. In addition, the plot shows how large is the dispersion of low temperature data: this is explained by the fact that those tests require more time to reach rupture, so all the uncertainties involved tend to spread consistently the specimen life spectrum.
With the aim to follow the time evolution of the cladding cumulative damage function, a time-temperature parameter is needed to predict the time-to-rupture, starting from known stress and temperature. The idea has been to represent the whole dataset (composed by the three sets of trials displayed in Figure 3.10) with P parameter, which should be more reliable for such steel with respect to LM. Then, the capability of the already embedded TRANSURANUS correlation to represent the same points given the corresponding stress has been evaluated.

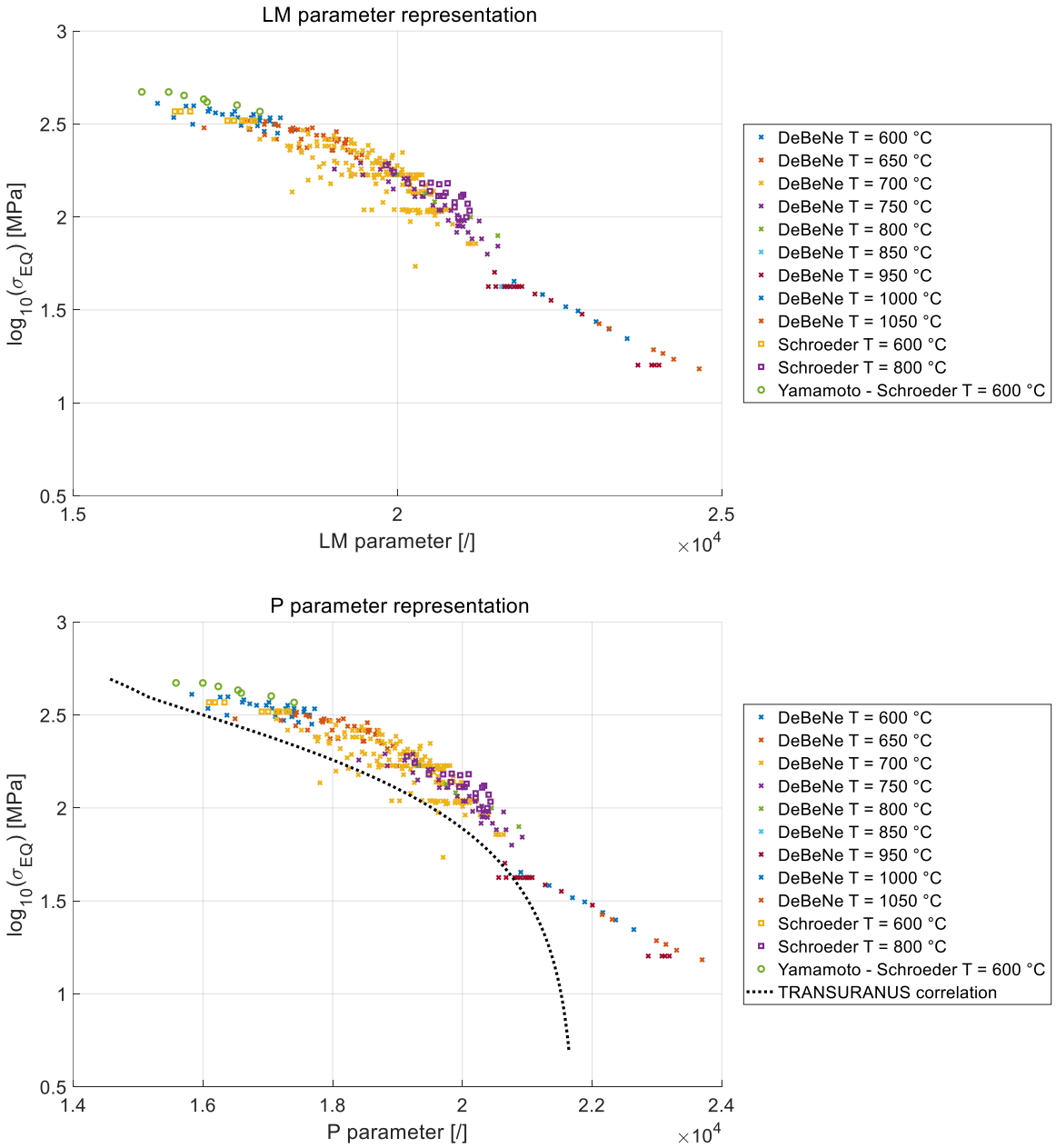

Figure 3.11: Representation of experimental time-to-rupture dataset with Larson-Miller and with P parameter.

Figure 3.11 shows the difference in data representation exploiting one parameter or the other. Differently from expectations, no significant improvements emerge exploiting the P parameter, since similar plots are obtained. The difficulty in the representation consists in the change of the creep mechanism at low temperature (from n=5 to n=3) and in the non-linear PLB regime at high stresses. As a matter of fact, the two transitions do not allow having a unique, straight line even though the P parameter should include the true creep flow law. As for the TRANSURANUS correlation, it supplies very conservative time-to-rupture values at a given stress[26], to the point that it becomes nearly impracticable at very low stresses.

[26] Remember that the definition of the parameters include the logarithm of the time-to-rupture, so a little difference becomes a huge temporal shift.

A new correlation reveals compulsory to fit at best the collected data, avoiding too conservative outcomes. Being the LM parameter the one generally adopted to compute the time-to-rupture and being the diversity between its adoption and the P one negligible (at least for the dataset under consideration), a new LM parameter approach has been selected for the scope of interest.
The whole dataset has been split into low temperature trials (up to 800 °C) and high temperature ones. The two functional shapes suggested by Delville in [27], then, have been selected to fit the two groups (Equation (3.14) and Equation (3.15)), but their coefficients have been tuned on the wider dataset selected in this part of the review (see Figure 3.10) through a least mean square optimization scheme. The optimized coefficients are reported in Table 3.6.

$$\mathrm{LMP}\ [/] = \mathrm{T}(\ 17.6 + \log_{10} \mathrm{t_R}\ ) \tag{3.13}$$

$$\mathrm{LMP}_{\mathrm{highT}} = \mathrm{A_1} \cdot \log_{10} \sigma_{\mathrm{EQ}} + \mathrm{A_2} \qquad \mathrm{T} > 800\ °\mathrm{C} \tag{3.14}$$

$$\mathrm{LMP}_{\mathrm{lowT}} = \left(\frac{\mathrm{B_1}}{\mathrm{B_3}} \cdot \left(\log_{10} \sigma_{\mathrm{EQ}} - \mathrm{B_2}\right) + 1\right) \cdot \cdot\ (1 + \mathrm{B_3} - \exp\left(\mathrm{B_4} \cdot (\log_{10} \sigma_{\mathrm{EQ}} - \mathrm{B_2})\right)) \qquad \mathrm{T} \leq 800\ °\mathrm{C} \tag{3.15}$$

$$\mathrm{T\ [K]}\ ,\ \mathrm{t_R\ [h]}\ ,\ \sigma_{\mathrm{EQ}}\ [\mathrm{MPa}]$$

Table 3.6: Optimized coefficients for the correlations derived from the *New Larson-Miller* approach.

High T correlation		Low T correlation	
A_1	$-6.4103\ 10^3$	B_1	2.6403
		B_2	1.2136
A_2	$-3.2205\ 10^4$	B_3	21.0068
		B_4	1.4597

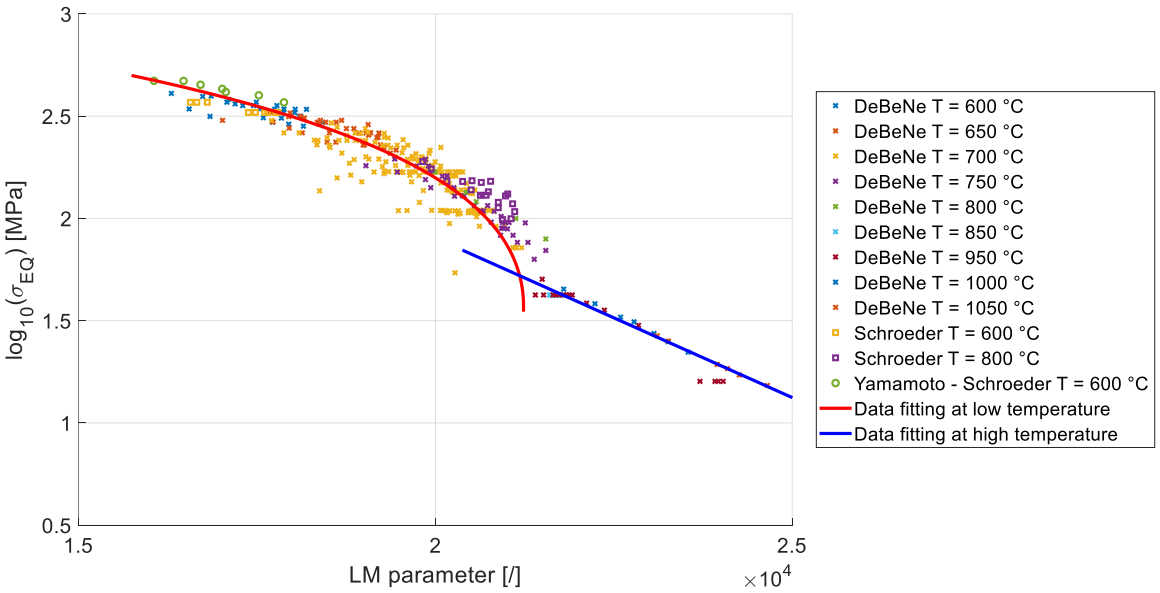

Figure 3.12: Time-to-rupture dataset representation with Larson-Miller parameter and data fitting correlations at high and at low temperatures.

As from Figure 3.12, it is evident how such two correlations provide more accurate predictions with respect to TRANSURANUS one. The transition region, however, must be treated with care since the discontinuity of the derivative could lead to convergence issues in the code. Thus, a unique, continuous function (in the following called *New LMP* approach) has been developed joining the previous two with a sigmoidal function in the form of a hyperbolic tangent [38], Equation (3.16).

$$\omega(\sigma_{EQ})\ [/] = \frac{1 + \tanh\left(\frac{\sigma_{EQ} - \sigma_0}{s}\right)}{2} \tag{3.16}$$

σ_0: intersection stress between high and low temperature correlations

$$\sigma_0 = 52.468\ \text{MPa}$$

s: smoothness parameter for the sigmoidal transition between 0 and 1

$$s = 6.51\ \text{MPa}$$

The s parameter has been found again through a least mean square optimization: it has been used as design variable to minimize the sum of the square differences between the whole dataset and the new continuous correlation predictions (with parameter A_1, A_2, B_1,.. etc fixed at the values defined in Table 3.6).
Equation (3.17) is the final continuous correlation to predict the LM parameter starting from the known applied stress; Figure 3.13 shows it against the whole experimental dataset.

New LMP approach	$\text{LMP} = [A_1 \cdot \log_{10}\sigma_{EQ} - A_2] \cdot (1 - \omega(\sigma_{EQ})) + \left[\left(\frac{B_1}{B_3} \cdot (\log_{10}\sigma_{EQ} - B_2) + 1\right) \cdot (1 + B_3 - \exp(B_4 \cdot (\log_{10}\sigma_{EQ} - B_2)))\right] \cdot \omega(\sigma_{EQ})$	(3.17)

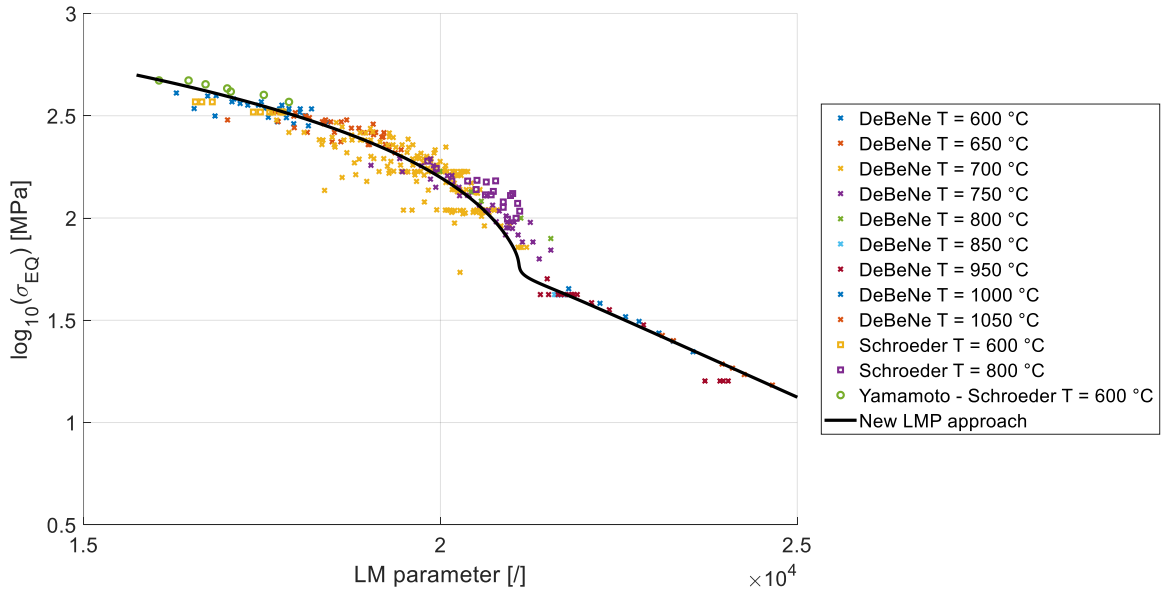

Figure 3.13: Time-to-rupture dataset representation with Larson-Miller parameter and the correlation of the *New Larson-Miller* parameter approach.

The developed *New LMP* approach here presented needs to be implemented inside the TRANSURANUS code (as explained later on) and will be used to evaluate the evolution with time of the cladding cumulative damage function for the MYRRHA fuel pins. In this way, both a conservative approach (the one already embedded inside TRANSURANUS) and a best estimate one (the *New LMP*) will be available for the performance analysis.

3.3.2 Irradiation creep

The irradiation creep phenomenon is treated inside the *v1m1j18* version of TRANSURANUS code without a correlation specific for DIN1.4970 (see Section 3.2.2), thus a deep review of available literature data is required.

Actually, few experimental measurements can be found regarding the steel of interest: this is not astonishing, being limited the knowledge about the phenomenon. Data exploited in the following refer to trials performed by SCK•CEN with the mixed spectrum reactor BR-2 [39], with the purpose to test the implications of He formation on materials. Precisely, a cold-worked and aged DIN1.4970 steel was employed in the experimental campaign[27].

Instead of fitting a bunch of data from scratch, a new flow law has been developed following the suggestion by Grossbeck in [39]: data have been interpolated exploiting a square root dependence on neutron flux of the irradiation creep strain rate. The error indicators have proven to be better with respect to the adoption of a linear dependence (as the one which appears in the TRANSURANUS model). As for the other variables, the same relation existing inside the *Többe* correlation has been adopted, i.e., linear with applied stress and mean neutron energy.

The developed correlation, named *Grossbeck* data fitting, is reported in Equation (3.18). In Figure 3.14, it is represented against the few experimental data available in the open literature as a function either of the dose rate or of the neutron flux.

A clarification is needed: a conversion factor between dose rate and neutron flux has been required, being the first the units in which experimental data are reported in the reference paper [39], whereas the TRANSURANUS correlation involves the neutron flux. Although a specific conversion factor is not reported inside the original document, a symbolic value equal to $1 \cdot 10^{21}$ dpa^{-1} cm^{-2} has been assumed for the BR-2 reactor, taking as reference the typical values valid for thermal and fast reactors suggested in [2].

As shown in Figure 3.14, *Többe* correlation underestimates the experimental dataset with a gap of three orders of magnitude. This means that the irradiation creep strain rates predicted by the *Grossbeck* data fitting may stand above the thermal creep ones in MYRRHA conditions, instead of being of secondary importance. In light of this big discrepancy, it is deemed essential to simulate the behaviour of MYRRHA fuel pins exploiting both the two models. The implementation of the new data fitting is required accordingly.

[27] As it has been said in Section 3.3.1.1, aging has not a crucial role in determining the creep response of the material, hence such data can be exploited to develop a new correlation for DIN1.4970 steels in general.

Grossbeck data fitting	$\dot{\varepsilon}_{irr}\ [h^{-1}] = 1.266 \cdot 10^{-15}\ \bar{E}\ \sigma_{EQ}\ \sqrt{\phi}$ $\sigma_{EQ}\ [MPa]\ ,\ \bar{E}\ [MeV]\ ,\ \phi\ [cm^{-2}s^{-1}]$	(3.18)

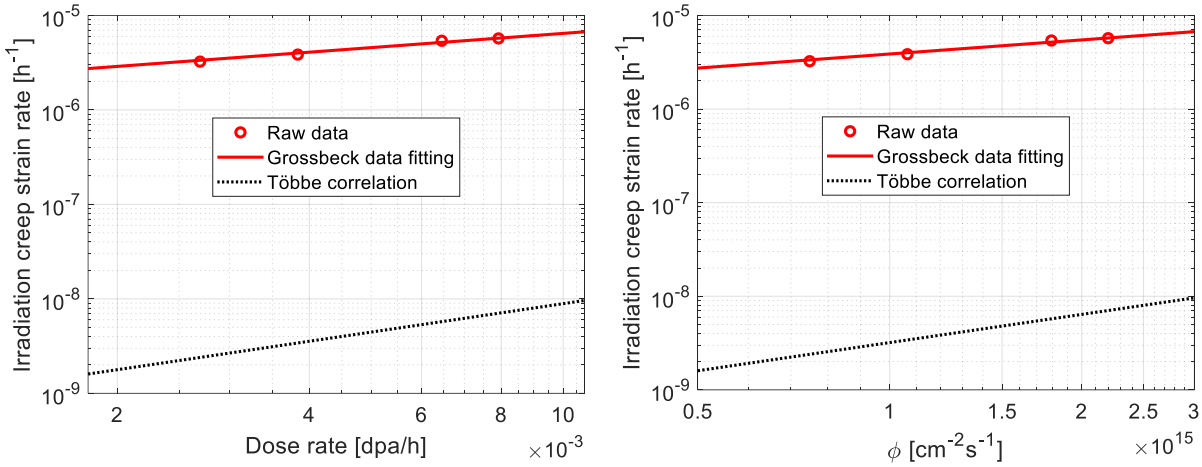

Figure 3.14: Comparison between *Többe* correlation and *Grossbeck* data fitting at $\bar{E}$=1 MeV and σ_{EQ}=100 MPa .

3.3.3 Void swelling

A specific correlation does not exist in *v1m1j18* version of TRANSURANUS code to treat the swelling response of DIN1.4970 steel, similarly to what hold for irradiation creep. A satisfactory source, however, can be found in the open literature.

In the development of the European Facility for Industrial Transmutation (EFIT), a subcritical ADS being part of the EUROTRANS (European Research Programme for the Transmutation of High Level Nuclear Waste in an Accelerator Driven System) integrated project, the fuel performance code MACROS (developed at SCK•CEN) was used [40]. In this code, a convenient correlation was employed to deal with the swelling of DIN1.4970 steel in fast reactor conditions. More precisely, four alternatives of the same steel are discriminated, whose compositions are reported in Table 3.7; on the basis of the material choice, the correlation coefficients change.

The new model (Equation (3.19)), in the following called *Lemehov* correlation, is an elaboration of the original expression: whereas the last one supplies the increment of the swelling effect $\delta(\Delta V/V)$ due to an accumulation of damage dose during a timestep, the first displays a dependence on fast neutron fluence[28], being more rapidly comparable with the TRANSURANUS models. Table 3.8 shows the correlation parameters for the four versions of the steel.

[28] To translate the damage dose dependence into a fast (E>0.1 MeV) fluence dependence, all parameters and variables originally expressed in dpa have been multiplied by the conversion factor adopted in the reference paper and equal to $1/2\ 10^{-22}\ dpa^{-1}\ cm^{-2}$ [40].

Lemehov correlation [40][29]	$$\delta\left(\frac{\Delta V}{V}\right)[\%] = \dot{S}_0(T)\left(\delta\Phi + \alpha\cdot\ln\left(\frac{\left(1+\exp\left(\frac{\Phi_0(T)-\Phi-\delta\Phi}{\alpha}\right)\right)}{\left(1+\exp\left(\frac{\Phi_0(T)-\Phi}{\alpha}\right)\right)}\right)\right) \quad (3.19)$$ $$T\,[K]\,,\ \delta\Phi\ [cm^{-2}]$$ $$\alpha\text{: constant}\quad \alpha = \left(\frac{1}{0.15}\right)\cdot\frac{1}{2\ 10^{-22}}\ cm^{-2}$$ $$\Phi\ [cm^{-2}]\text{ : neutron fluence before the increment }\delta\Phi$$ $$\dot{S}_0\text{: swelling rate}$$ $$\dot{S}_0\ [cm^2] = \dot{S}_{0,max}\cdot\frac{\tanh\left(\frac{T-T_S^i}{2\,\Gamma_S^i}\right)-\tanh\left(\frac{T-T_S^v}{2\,\Gamma_S^v}\right)}{2\ \tanh\left(\frac{T_S^v-T_S^i}{4\,\Gamma_S^*}\right)}\cdot 2\ 10^{-22} \qquad \Gamma_s^* = \min\left\{\Gamma_s^i, \Gamma_s^v\right\}$$ $$\Phi_0\text{: incubation fluence}$$ $$\Phi_0\ [cm^{-2}] = D_{0,max}\cdot\frac{\tanh\left(\frac{T-T_D^i}{2\,\Gamma_D^i}\right)-\tanh\left(\frac{T-T_D^v}{2\,\Gamma_D^v}\right)}{2\ \tanh\left(\frac{T_D^v-T_D^i}{4\,\Gamma_D^*}\right)}\cdot\frac{1}{2\ 10^{-22}} \qquad \Gamma_D^* = \min\left\{\Gamma_D^i, \Gamma_D^v\right\}$$

Table 3.7: Weight composition (%) of the four DIN1.4970 alternatives [40].

Element	DIN1.4970 B	DIN1.4970 I	DIN1.4970 K	DIN1.4970 L
C	0.083	0.089	0.086	0.086
Si	0.420	1.010	0.990	0.960
Mn	1.600	1.160	1.600	1.640
Cr	14.950	15.150	15.060	15.150
Ni	14.730	15.000	14.860	14.900
Mo	1.190	1.450	1.460	1.460
V	0.010	0.010	0.020	0.020
Ti	0.470	0.310	0.490	0.500
Co	0.017	0.018	0.016	0.017
B	0.002	0.003	0.002	0.002
N	0.018	0.016	0.017	0.017
P	<0.015	<0.015	<0.015	<0.015
Fe	66.496	65.769	65.384	65.233

[29] Note that, differently from the original reference [40], the minus sign in front of the fraction at both the two exponential arguments has been omitted. In this way, the trend of the diameter change as a function of the accumulated damage dose is coherent with the figures included in the original work, implying an error in the formula there presented.

Table 3.8: *Lemehov* correlation coefficients for the four DIN1.4970 alternatives [40].

Parameter	DIN1.4970 B	DIN1.4970 I	DIN1.4970 K	DIN1.4970 L
$\dot{S}_{0,max}$ [%/dpa]	0.25	0.115	0.185	0.185
T_s^i [K]	698	688	698	698
Γ_s^i [K]	25	25	25	25
T_s^v [K]	718	713	718	713
Γ_s^v [K]	25	25	25	25
$D_{0,max}$ [dpa]	60	60	60	60
T_D^i [K]	698	643	643	623
Γ_D^i [K]	25	25	25	25
T_D^v [K]	773	788	788	793
Γ_D^v [K]	25	25	25	25

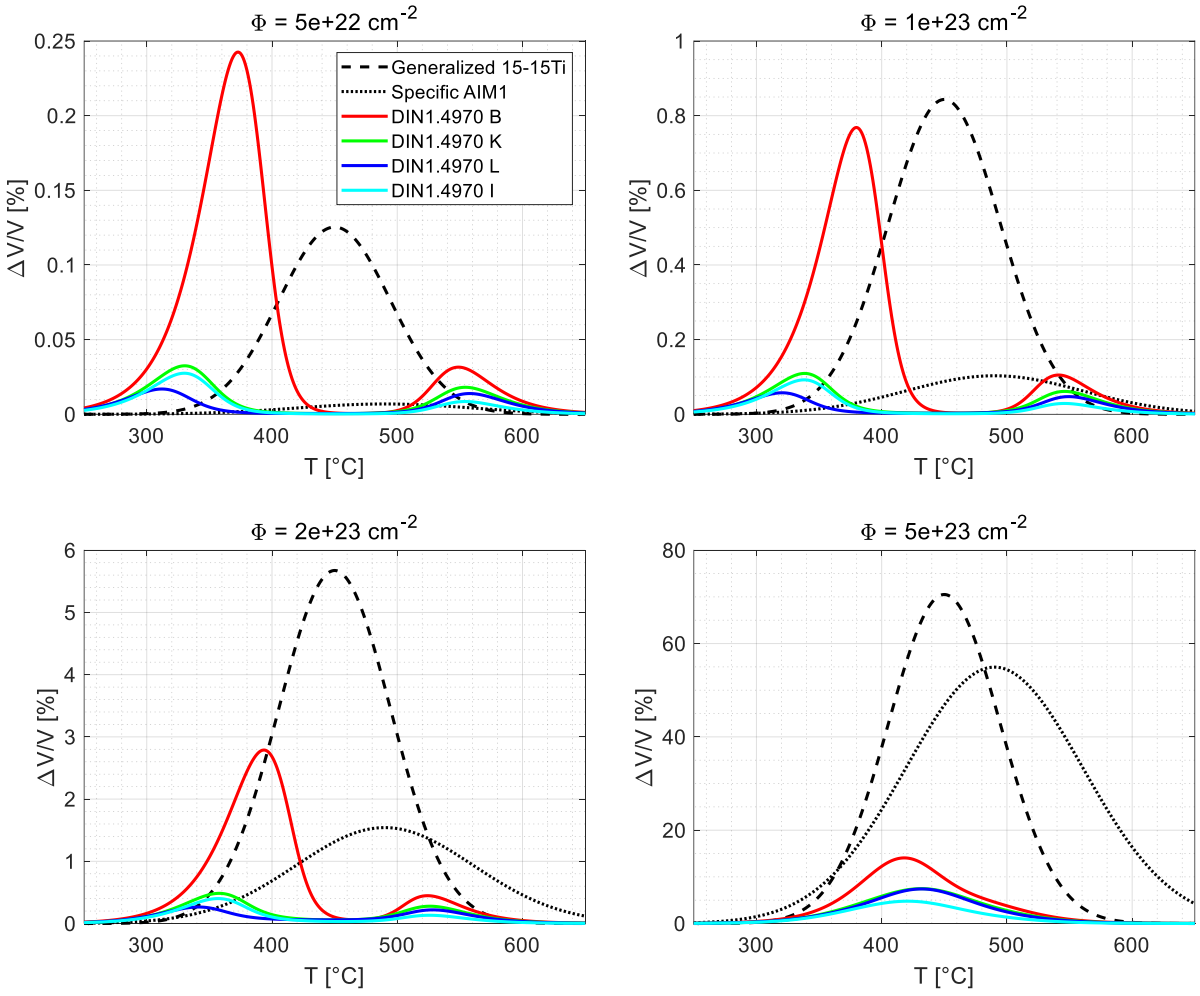

Figure 3.15: Comparison between TRANSURANUS and *Lemehov* correlations at fixed neutron fluences.

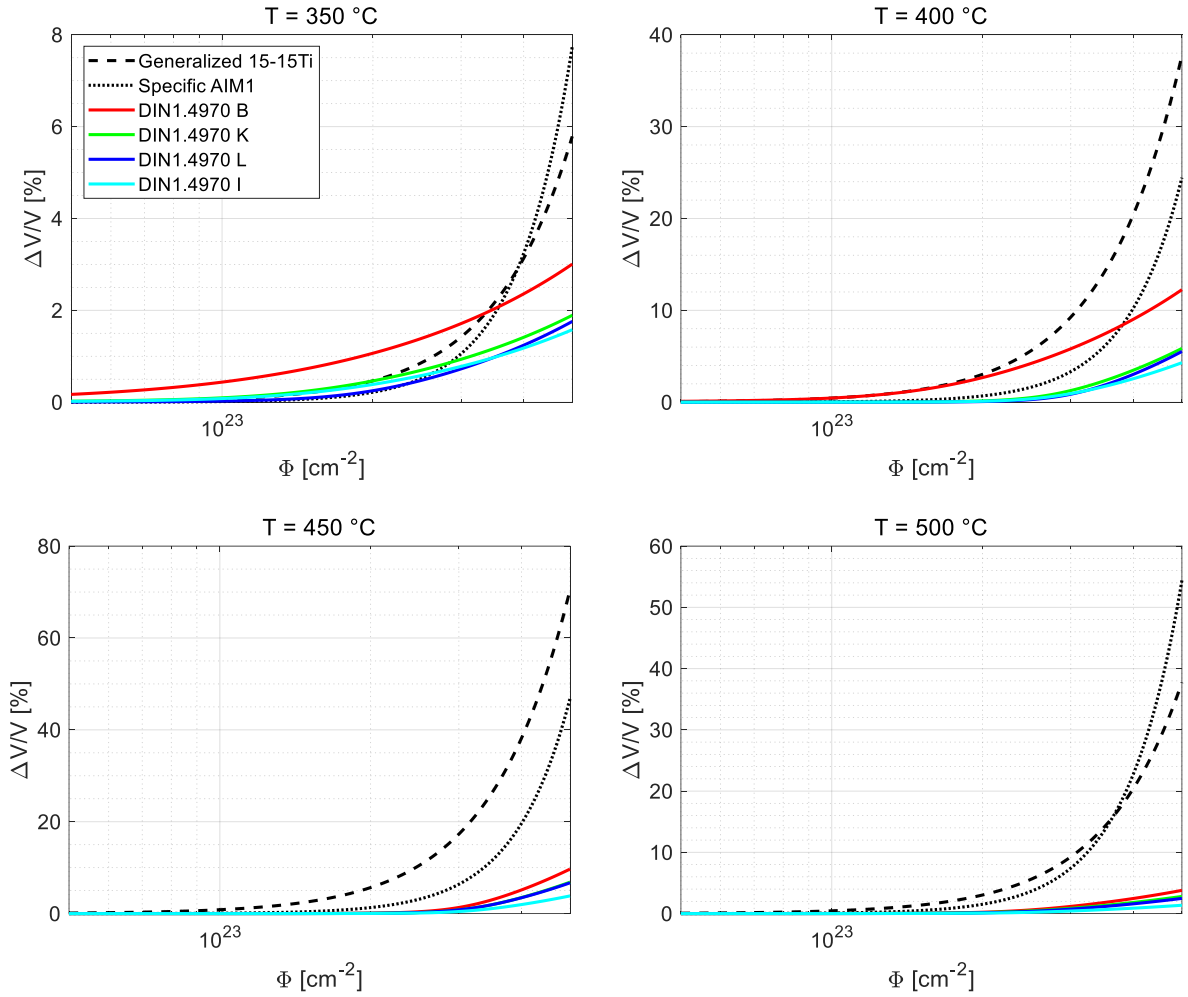

Figure 3.16: Comparison between TRANSURANUS and *Lemehov* correlations at fixed temperatures.

In Figure 3.15 and Figure 3.16, a comparison between the already embedded TRANSURANUS correlations (*Generalized 15-15Ti* and *Specific AIM1*) and the *Lemehov* ones is reported, differentiating from the material choices as well. The volumetric swelling effect as a function of temperature at fixed neutron fluence is displayed in Figure 3.15; the swelling effect as a function of neutron fluence at fixed temperature in Figure 3.16.

From Figure 3.15, it is possible to verify the typical bell shaped dependence of swelling against temperature (due, in turn, to the temperature driven vacancy motion mechanism), despite the presence of two maxima sometimes observed for cold-worked steels. The two TRANSURANUS correlations are reported just with the intent to compare the magnitude of the swelling effect for the two versions of the 15-15Ti steel (i.e., AIM1 and DIN1.4970), and the conclusion is that DIN1.4970 displays a much better resistance to the phenomenon especially at high fluence values. Concerning the steel chosen for MYRRHA cladding, the most important observation on this set of graphs is that the first swelling maximum reveals around 350-400 °C for any neutron fluence, which is very close to MYRRHA operating range: swelling will exhibit at its highest extent working such facility.

Very interesting is Figure 3.16, considering the TRANSURANUS simulations and the application to MYRRHA fuel pins: whereas temperature remains nearly constant in time (depending on the

power cycle), the neutron fluence increases. The existing code models underestimate the swelling effect at low temperatures and fluence; on the other hand, at higher temperature or neutron fluence, DIN1.4970 seems to behave much better than AIM1 steel, turning out to be much more robust, at least as far as void swelling is of concern. This implies the importance to embed the *Lemehov* correlations inside the TRANSURANUS code, avoiding too conservative estimations (i.e., a swelling up to one order of magnitude higher).

As for the specific alloy, in the open literature is not reported which will be the exact cladding composition to be adopted for MYRRHA, rather an indication about the choice of the DIN1.4970 steel and characteristic ranges for the percentage of the alloying elements (Table 3.3). Hence, as a tip for the design, it could be said that a higher Si percentage would be preferred from the point of view of swelling resistance under irradiation, as inferred from the optimal response of the "I version" of the steel. On the other hand, from the point of view of the fuel performance analysis, the unknown exact composition is a source of uncertainty, which is tackled investigating the behaviour of the pins with more than one swelling model and finding the worst possible performance scenario (see Section 4.4).

Precisely, the idea is to retain just two of the available correlations for DIN1.4970 steel and to discard the already implemented ones, since they refer to a different cladding material. The first model to be kept is the one addressed to the "B version" of DIN1.4970 which shows the worst response among the four at all the temperatures. Afterwards, only one among K, L and I is desirable as proponent for a tougher behaviour, since the predictions are very similar to each other and so it is impossible to discriminate them because of the uncertainties: the "L version" is selected, being in the middle between the three curves (Figure 3.16). The implementation of the two *Lemehov* correlations in the TRANSURANUS code is hence necessary.

3.3.4 Mechanical properties

3.3.4.1 Yield stress

Data for the yield stress of unirradiated DIN1.4970 austenitic stainless steel, 15% cold-worked and aged were collected in [41] and are reported in

Figure 3.17 together with the *Többe* correlation for the yield stress itself. Final aim is to verify if the TRANSURANUS model (Equation (3.8)), addressed generically to 15-15Ti steels, is able to predict the experimental points concerning the specific steel version of interest for MYRRHA.

From

Figure 3.17, it can be noticed that the TRANSURANUS correlation, with assessed 10% uncertainty, is not capable to reproduce well the mechanical properties for DIN1.4970 available data. However, whereas *Többe* correlation refers to a 20% cold-worked steel, experimental data derive from a 15% cold-worked and aged steel, and the different degree of cold-working, along with the aging process, may be the cause of the discrepancy. It can be argued that, at equal manufacturing state, the experimental data would fall inside the error band of the correlation.

To conclude, it is confirmed that the influence of minor alloying elements on yield stress is not so relevant and that the TRANSURANUS model can be deemed reliable to the purpose it was implemented for. No further improvements are thus necessary.

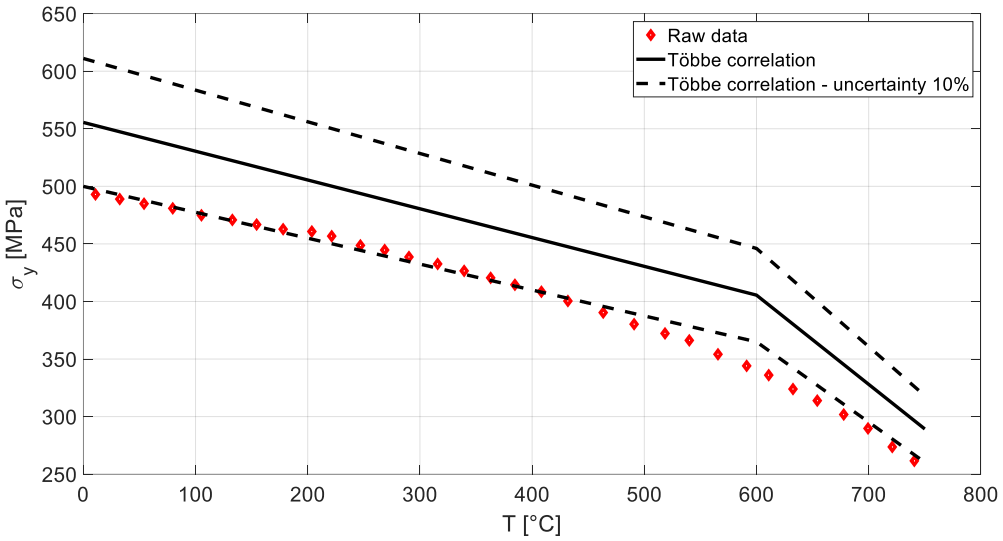

Figure 3.17: Validation of *Többe* correlation for yield stress with DIN1.4970 experimental data.

3.3.4.2 Rupture strain

Data for rupture strain were collected again in [41] referring to the same unirradiated material. Figure 3.18 shows the validation of the *Többe* correlation for the rupture strain (Equation (3.9)) on those data. As it can be noticed from the plot, the TRANSURANUS correlation provides rather conservative estimations for the rupture strain as a function of temperature. Nevertheless, the trend of the two curves is similar, with a minimum near the MYRRHA operating range. The discrepancy is again ascribed to the dissimilarity in the thermo-mechanical treatment featuring the two references. Probably, the difference would be partially reduced considering, together with the cold-working and aging difference, the error band accompanying the model. The uncertainty, however, is not reported in the reference document.

A similar conclusion holds for rupture strain as well as for yield stress: the already embedded correlation is deemed reliable and no further implementations are carried out in this review.

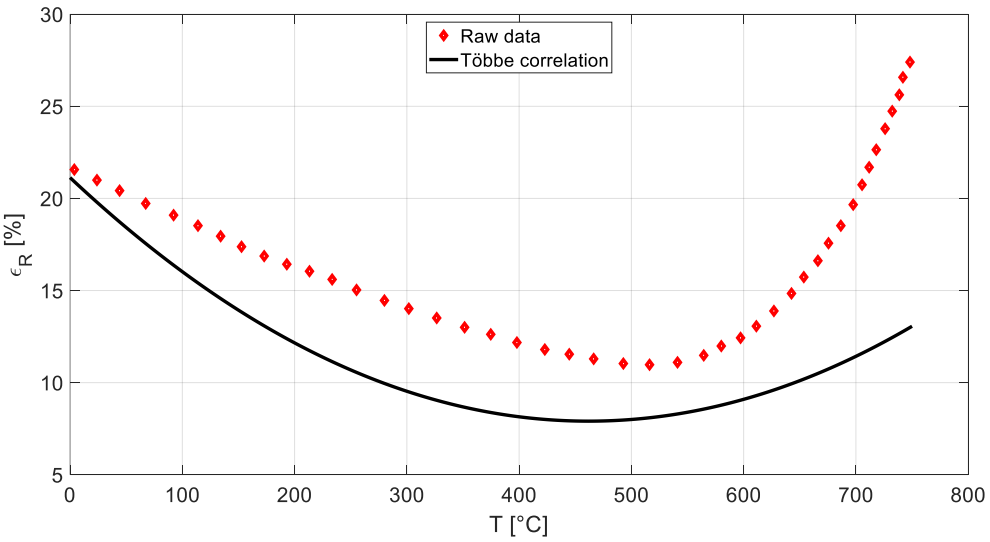

Figure 3.18: Validation of *Többe* correlation for rupture strain with DIN1.4970 experimental data.

3.4 Implementation

The outcome of the comparisons carried out in Section 3.3 suggests that five correlations require the implementation inside the TRANSURANUS code, specifically:

- *Modified Delville* correlation for thermal creep;
- *Grossbeck* data fitting for irradiation creep;
- *New LMP* approach to evaluate the evolution of the cumulative damage function as indicator for the rupture of the cladding;
- *Lemehov* correlations addressed to "B version" and "L version" of DIN1.4970 for void swelling.

Table 3.9 sums up the investigated models, together with the routines embedding them and how to select the desired option in the input file.
A deep description about the rationale at the basis of the implementation of the new routines is discussed in details in Appendix A.

Table 3.9: Summary table for the routines implemented in TRANSURANUS.

Correlation	Routine	Input file
Thermal creep		
Többe (thermal creep) - default	`crpc02`	`ModClad(7)=0`
Többe (thermal creep) - implemented	`crpc43`	`ModClad(7)=43`
Modified Delville	`crpc44`	`ModClad(7)=44`
Irradiation creep		
Többe (irradiation creep) - default	`crpc02`	`ModClad(7)=0`
Többe (irradiation creep) - implemented	`irrcrpc`	`iiii1=1`
Grossbeck data fitting	`irrcrpc`	`iiii1=2`
Cumulative damage function		
P parameter approach (conservative)	`cdfc`	`iiii3=0`
New LMP approach (best estimate)	`cdfc`	`iiii3=3`
Swelling		
Specific AIM1 – default	`sweloc – option 202`	`ModClad(4)=0`
Lemehov "B version"	`swec43`	`ModClad(4)=43`
Lemehov "L version"	`swec44`	`ModClad(4)=44`

Chapter 4

MYRRHA fuel performance analysis in base irradiation conditions

The starting point of the fuel performance assessment for a new reactor concept is the analysis of fuel pin behaviour in normal operating conditions. Understanding the evolution of the phenomena occurring inside the fuel rod in normal operating conditions, indeed, is essential to figure out how the same mechanisms would take place in off-normal scenarios, which must be considered in order to establish the final pin design.

This chapter aims at studying the performance of MYRRHA fuel pins under base irradiation conditions, assessing the corresponding design limits and providing a foundation to better understand the criticalities of the following accidental scenarios.

Accordingly, Section 4.1 describes the operating schedule characterizing MYRRHA reactor and reports the conservative hypothesis leading to the "hottest pin" individuation, together with simulation inputs and indicative design limits assumed as guidelines for the performance assessment. Being the analysis performed with the TRANSURANUS code, the modelling issue is presented in Section 4.2, starting from the geometry discretization until the selection of the standard models employed to describe all the phenomena taking place inside the fuel pin during its in-reactor life.

TRANSURANUS simulation results are discussed in Section 4.3, focusing on the slices suffering the harsher conditions in terms of temperature or deformation and verifying the compliance with design limits. Such results are under the name of "reference case", given that they are obtained through the code standard models. To account for different possible modelling of the same material properties/phenomena, a sensitivity analysis on models is performed to get the most pessimistic view of the MYRRHA fuel performance. A complete description of the followed rationale and the choices adopted to carry out the analysis is the topic of Section 4.4, and it will be useful also in the next chapter analysing the fuel response to accidental conditions. The outcome of the sensitivity analysis, i.e., the "worst case" scenario, is disclosed in Section 4.5, which reanalyses the MYRRHA fuel performance considering as input the combination of models leading to the worst conditions in terms of fuel temperature and cladding deformation.

4.1 Base irradiation conditions

The operating schedule of MYRRHA consists in irradiation cycles. Each fuel assembly spends about 90 days inside a specific position (*batch*) of the core, then the reactor is stopped, inspections or maintenance are carried out for 30 or 90 days respectively, and eventually the assemblies are reshuffled in an outermost position, whereas the slot they leave is occupied by another assembly one batch fresher (Figure 4.1) [14].

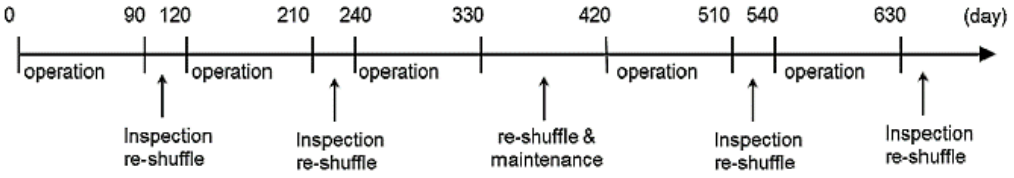

Figure 4.1: MYRRHA operating schedule [14].

Considering the symmetry of the core, 12 batches are identified, at the end of which one fuel assembly has accumulated more than 1000 days under irradiation and a total lifetime of 5 years. Inside each batch, different irradiation conditions exist, depending on the position: on average, getting farther from the core centre makes the neutron flux lower and so the power produced by the fuel assembly itself. Figure 4.2 shows the position of the 12 batches and the power produced by a fuel assembly within each batch.

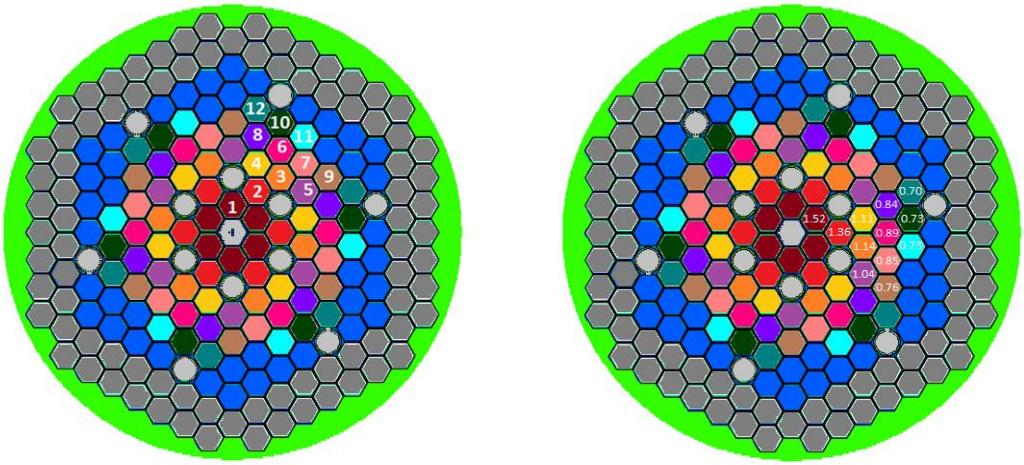

Figure 4.2: Batch positions in MYRRHA core (left) and total power in MW_{th} produced by each fuel assembly (right) [13].

At the same time, different rods undergo different conditions within the fuel assembly itself. The core performance, however, is not limited by the average situation, rather by the most severe one considering the whole fuel pin irradiation history: whether the thermal-mechanical limits are respected in this spot, then the design is adequate. Considering a specific fuel assembly starting from its insertion inside the MYRRHA core until the extraction, it is possible to appreciate that the position of the hottest pin changes from one batch to another, as testified in Figure 4.3. Speaking about fuel temperature, indeed, even though the neutron flux changes radially, at corner and edge sub-assemblies the coolant mass flow rate varies as well, thus it can happen that the maximum

fuel temperature displays either in peripheral rods or in central ones. Such aspect has positive implications on fuel pin design, as those fuel pins which are heavily loaded during the first batches can relax during the final ones or vice-versa.
A conservative hypothesis, conversely, is maintained for all the fuel performance analysis which follows: the worst conditions have been recognized within each batch and they have been attributed to a fictitious *hottest pin* herein investigated. That is, despite the real hottest pin changes between one batch and another, according to the hypothesis there exists one critical fuel rod that is localized in the hottest pin position during every batch. Such assumption clearly overestimates the final situation of the most loaded pin, but may be useful to conservatively adjust its design, in order to develop a safer reactor core.

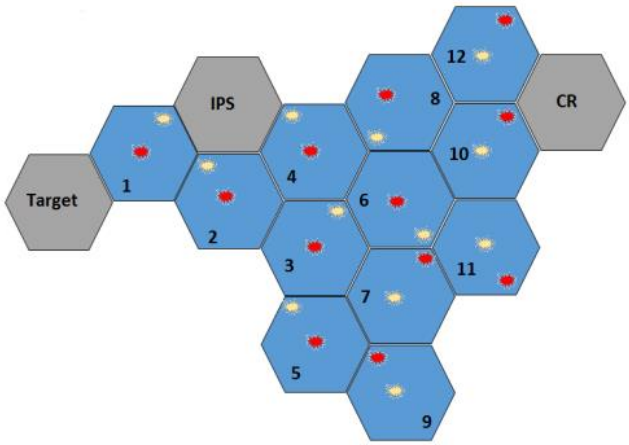

Figure 4.3: Position of hottest (red) and coldest (yellow) pin in each batch [13].

4.1.1 Power history and thermal-hydraulics input data

Overall data about the MYRRHA hottest pin are reported in Table 4.1.
In Figure 4.4 and Figure 4.5, the axially averaged evolution in time and the axial profiles at the beginning-of-life (batch 1) and at the end-of-life (batch 12) of linear power and fast neutron flux, respectively, are reported, as they are fundamental inputs for the simulation of base irradiation. The two figures allow verifying what it has been previously mentioned about the real MYRRHA irradiation conditions throughout the different batches: starting from the first one, both the linear power and the neutron flux gradually decrease moving towards outer positions (instead, they have been kept as constant within the same batch according to the current reactor design).
The magnitude of both the linear power and the fast neutron flux envisaged for MYRRHA reactor, must be highlighted: whereas the first one it is expected to reach peak values in excess of 400 W/cm for future Generation IV FRs, in MYRRHA it is limited to about 230 W/cm, close to typical LWR conditions. On the other hand, the fast neutron flux is much higher than in a commercial water reactor, being the MYRRHA facility a fast spectrum one. In light of these observations, it is expected to find performance results neither compatible with LWR conditions, nor with FBR ones, but rather between the two.
Reactor shutdown has been finally considered after batch 12. To avoid LBE solidification, however, it has been supposed that the coolant remains at its nominal inlet condition (both in terms of temperature and pressure), while power and flux are reset.

As for the coolant hottest pin boundary conditions considered for the TRANSURANUS simulations, a constant inlet temperature equal to 245 °C has been assumed at a constant pressure of 0.6 MPa (bigger than the initial fill-gas pressure, Table 2.4).
Similarly to LBE inlet temperature and pressure, the coolant mass flow rate has been assumed constant in time, but different according to the considered pin within the fuel assembly: 0.48 kg/s holds for inner pins, 0.56 kg/s for average pins and 0.76 kg/s for edge and corner pins[30]. Therefore, for simulating the hottest pin behaviour, it has been necessary to identify from Figure 4.3 its position inside the fuel assembly during each batch, and then to attribute the correspondent value of the coolant mass flow rate.
The main MYRRHA thermal-hydraulics data for the hottest pin are summarized in Table 4.1.

Table 4.1: MYRRHA hottest pin and coolant thermal-hydraulics input data [13].

Hottest pin data	
Total pin power	7.88 kW
Average linear power	123.1 W/cm
Axial peak factor at BoL (batch 1)	1.218
Axial peak factor at EoL (batch 12)	1.137
Average fast neutron flux	8.054 10^{14} n/(cm^2 s)
Total burnup	62.05 MWd/kg
Thermal-hydraulics data	
Coolant inlet temperature	245 °C
Coolant pressure	0.6 MPa
Coolant mass flow rate	
- Inner pins	0.48 kg/s
- Average pins	0.56 kg/s
- Edge and corner pins	0.76 kg/s

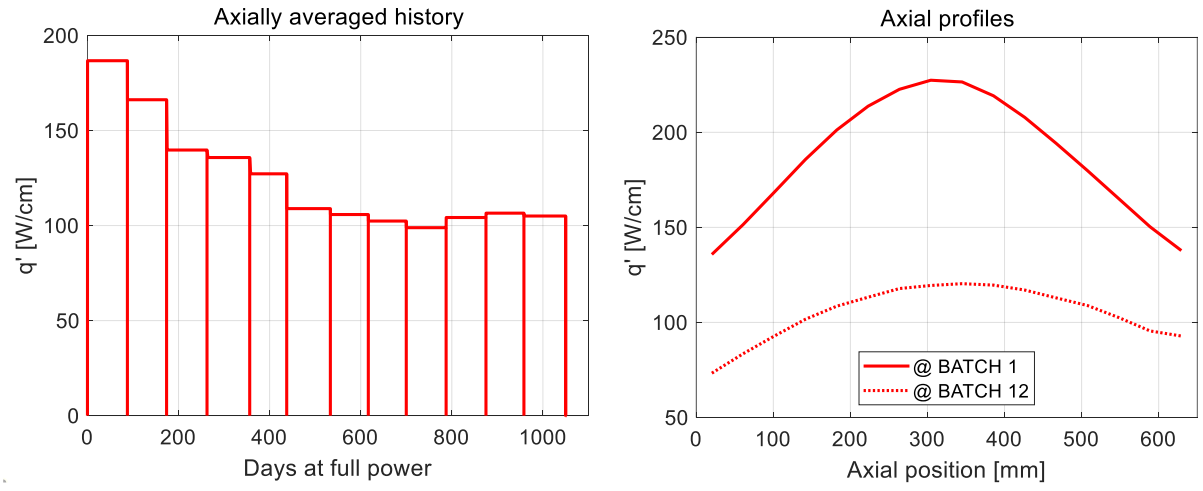

Figure 4.4: Linear power history and axial profiles at BoL (batch 1) and at EoL (batch 12).

[30] The corresponding flow areas are 25 mm^2, 37.5 mm^2 and 42.5 mm^2 respectively.

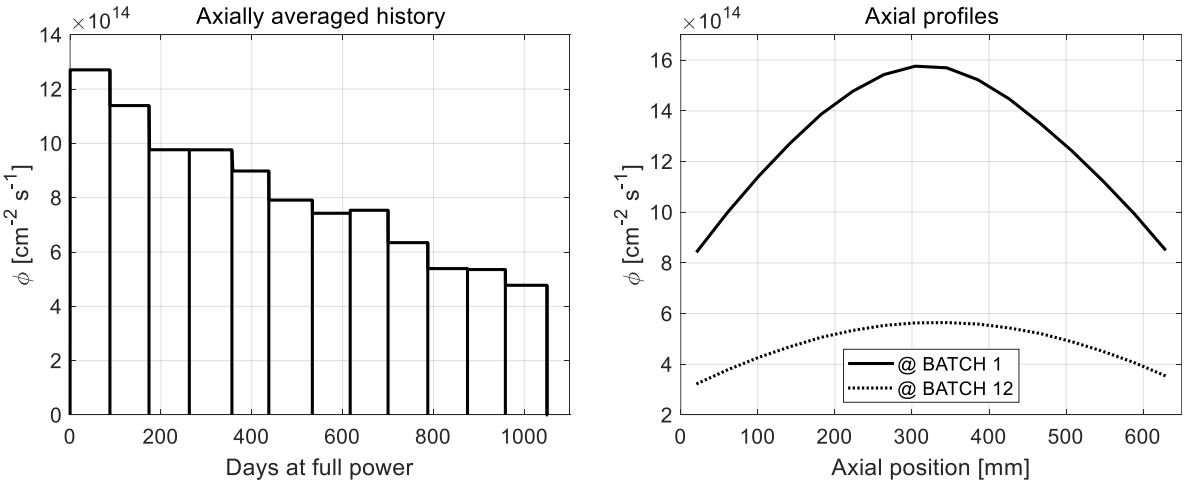

Figure 4.5: Fast neutron flux history and axial profiles at BoL (batch 1) and at EoL (batch 12).

4.1.2 Design limits for base irradiation conditions

In order to critically assess the current MYRRHA fuel pin design performance in base irradiation conditions, it is necessary to evaluate the safety margins with respect to suitable design limits. Unfortunately, such specific information regarding the MYRRHA fuel pins are still not available.
In this work, the design indications valid for ALFRED reactor [42] and for LMFBRs in general [33][43][44] are taken as reference and are presented in Table 4.2. Given that they are not tailored on the facility of interest (i.e., on the specific fuel and cladding material choices for MYRRHA), they are used merely as a rough guide to assess the pin design[31]. That is, they are not used to affirm whether the current pin specifications are certainly adequate or not, rather to select the most important figures of merit among the available outputs calculated by the TRANSURANUS code, and to draw attention to some potential design weaknesses.

Table 4.2: Indicative design limits for MYRRHA base irradiation conditions.

Quantity	Design limit	Reference
Peak fuel temperature	2000 °C	[42]
Peak cladding temperature	550 °C	[42]
Inner gas pressure	5 MPa	[42]
Cladding ΔD/D	7%	[33]
Cladding thermal creep strain	0.2%	[33]
Cladding total creep strain	3%	[43]
Cladding swelling strain	3%	[33]
Cladding plastic strain	0.5%	[44]
Cladding cumulative damage function	0.2/0.3	[33]

[31] An example of a figure of merit for which the limit reported in Table 4.2 could be inadequate, is the cladding ΔD/D. The steel corrosion-resistance performance against LBE, indeed, has not been assessed yet, and it is possible that oxide protective coatings will be employed for such a scope. In this perspective, smaller cladding radial deformations, even in the order of 1-2%, would probably be enough for the detachment of the protective layer.

4.2 Modelling

4.2.1 Fuel pin discretization

The TRANSURANUS code solves the fuel pin performance problem discretizing the domain by means of a selectable number of axial and radial nodes (1.5D approach, see Chapter 1). Specifically, the first step is to decide the number of axial slices to represent the fuel pin. Each axial slice is subdivided radially into coarse zones, i.e., into macro-regions sharing the same material properties. Finally, the coarse zones are split into a finer mesh where the solution is computed (i.e., the fine zones).

The pin discretization with TRANSURANUS is more matter of user experience than the result of a complex procedure of grid independence. The solution schemes of the code, indeed, change for different parts of the pellet computational mesh, resulting in different subdivision criteria in the radial direction. Considering, then, the presence of two superimposed radial zones, it is clear that to optimize the discretization is not a straightforward task[32]. In any case, the computational cost of a standard TRANSURANUS simulation is not as expensive as a CFD one (thus, saving simulation time is not of primary importance in TRANSURANUS) and, unless an excessively scarce number of nodes is selected, the results are not sensibly influenced by the grid choice.

In light of this discussion, the computational mesh adopted in this work has been selected as a good compromise between problem resolution needs and a sufficiently high number of total nodes.

Table 4.3 reports the discretization choices that have been applied to simulate the MYRRHA hottest pin.

First of all, concerning the axial direction, 16 slices of equal dimensions have been selected, which means one slice covering 4 cm of the fuel rod length (Figure 4.7)[33]. A axial slice representation has been employed, meaning that the mesh node is placed in the middle of each subdivision and all axial quantities are constant along the slice itself [7].

As far as the radial discretization is concerned, the same subdivision has been chosen irrespectively of the axial position. The fuel has been discretized into 5 coarse zones with an increasing number of fine nodes moving towards the pellet periphery: such choice, in case of FCMI, allows for a better resolution of the mechanical problem in the fuel region near the gap closure. As for the cladding, instead, only 1 coarse zone has been deemed sufficient, since the limited thermal gradient implies little variations of the material properties. On the other hand, 9 fine zones have been chosen, a number rather big considering the wall thickness (450 μm):

[32] The numerical architecture of the TRANSURANUS code is not consistent by definition (in the Courant's equivalence theorem sense [73]): that is, making the grid spacing tend to zero, the error between the numerical solution and the exact one does not approach zero; conversely, convergence errors may be encountered. There exists, rather, an interval of discretization parameters within which the numerical solution is verified.

The reason of such intrinsic characteristic is that TRANSURANUS was not developed as a thermo-mechanical simulator for any geometry, rather as a tool to provide fast and reliable results concerning nuclear reactor fuel pins through a dedicated numerical architecture.

[33] Data regarding the linear power and the neutron flux were provided for each centimetre of the pin. To condense them axially, an arithmetic averaging over the nodes pertaining to each slice has been applied.

nonetheless, cladding creep and swelling are significant phenomena to be properly modelled when dealing with FRs.
In Figure 4.7, a sketch of the fuel pin discretization is provided together with the centre position for every axial slice. Figure 4.6, instead, shows the axially discretized profile of the two main input quantities (i.e., linear power and fast neutron flux) for batch 1.

Table 4.3: Hottest pin discretization parameters.

Computational quantity	TU symbol	Nodes
Number of axial slices	`m3`	16
Number of coarse zones inside the fuel	`m1b`	5
Number of fine zones for each fuel coarse zone[b]:		
- coarse zone 1	`m2(1)`	5
- coarse zone 2	`m2(2)`	5
- coarse zone 3	`m2(3)`	5
- coarse zone 4	`m2(4)`	7
- coarse zone 5	`m2(5)`	9
Number of coarse zones inside the cladding	`m1h`	1
Number of fine zones for the cladding	`m2(6)`	9

[b] The coarse zone index enumeration starts with the inner one and proceeds outwards.

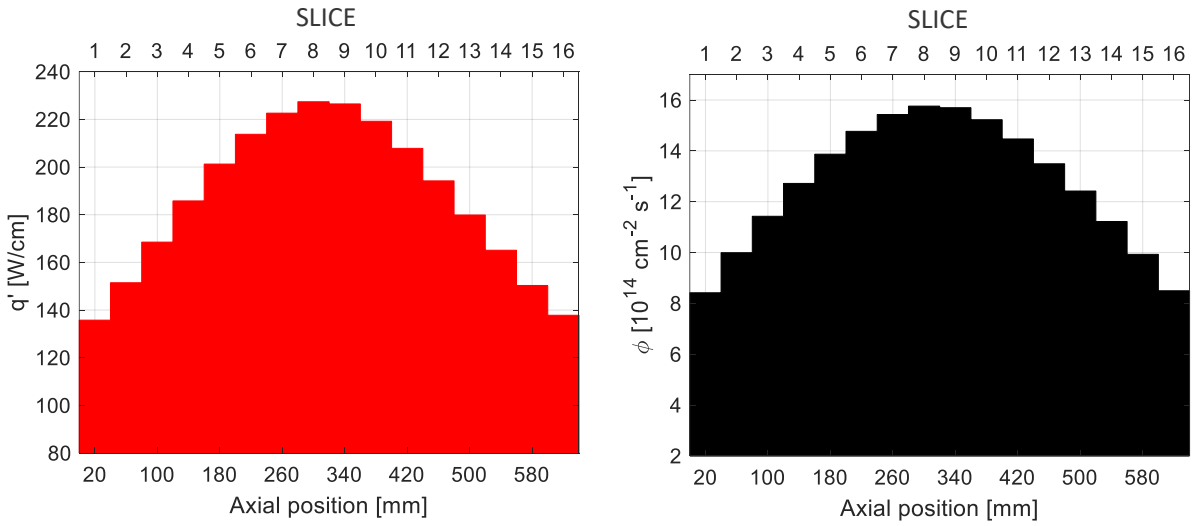

Figure 4.6: Axial discretization of linear power (left) and fast neutron flux (right) for batch 1.

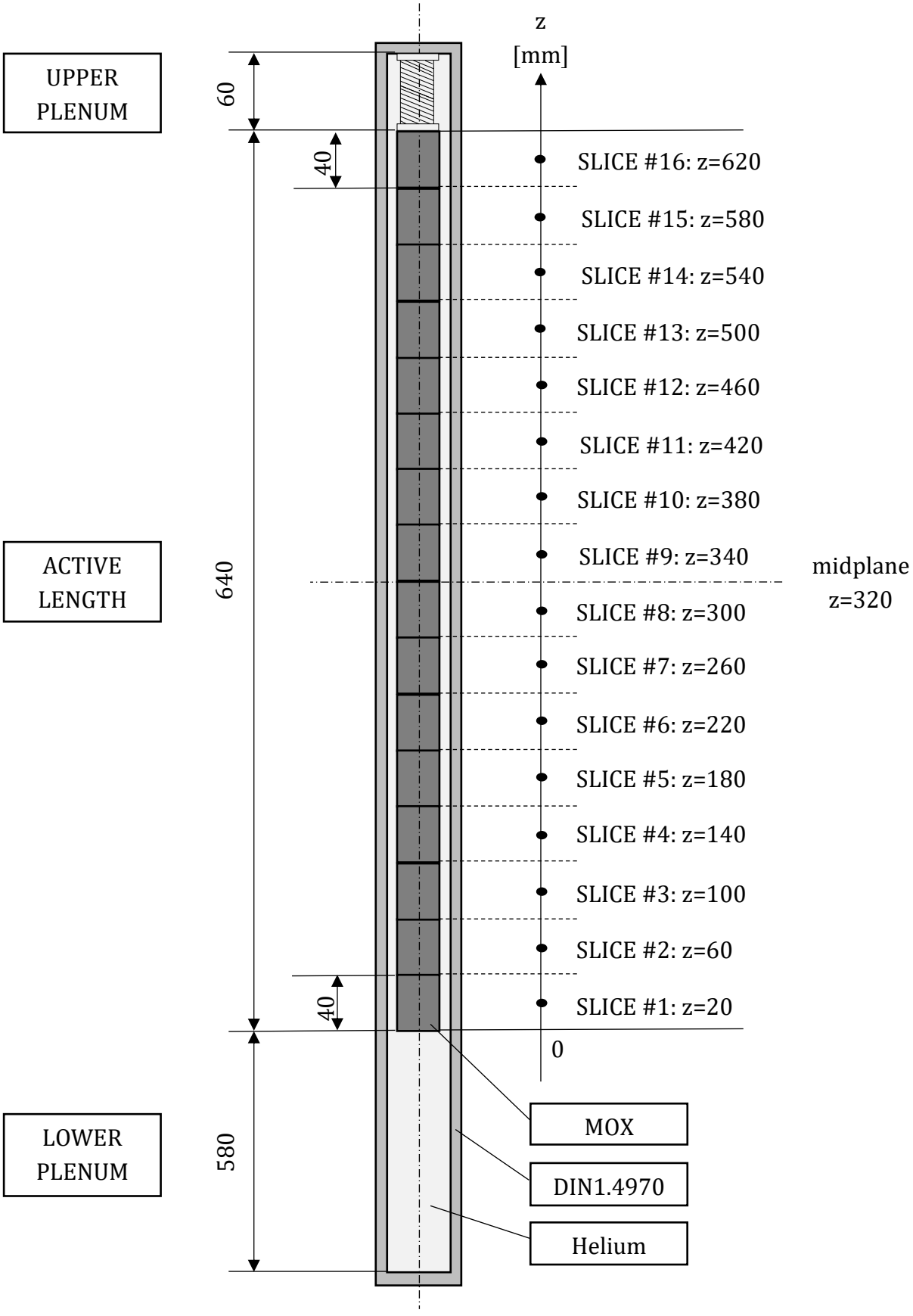

Figure 4.7: Fuel pin discretization sketch and centre position of the axial slices.

4.2.2 Simulation models

To describe the behaviour of an irradiated fuel pin in the most accurate way, a thorough selection of physical models and correlations is necessary. In this regard, TRANSURANUS offers a wide range of options to describe the same phenomenon or material property relevant for the simulation.

The first effort is to individuate all the alternatives suitable for the specific materials and irradiation conditions. Among all of them, an indication is provided in the code manual [7] about which is the recommended one, being the most reliable or more widely assessed. Some options, indeed, are not yet fully tested, suitable just for precise ranges and conditions, or simply less effective to fit the same experimental dataset. For this reason, the second step is to sort through all the model possibilities looking for the correspondent standard (or recommended) option.

This procedure has been followed to set up the input file for the MYRRHA hottest pin simulation and the main final choices are reported in Table 4.4 concerning the physical models and the treatment of the coolant, in Table 4.5 for the selection of material correlations.

The physical models that have been kept are mostly addressed to FBR conditions and cover all those phenomena which are typical for such reactors. An important exception holds for the cladding outer corrosion, a basic occurrence that currently cannot be accounted for, owing to the lack of an available option suitable for the MYRRHA cladding material.

As for the material properties, the general selection aimed at representing the LBE behaviour has been employed for the coolant without any exception. Likewise it has been done for the fuel, modelled with the set of correlations which better represents the MOX behaviour in FBR conditions; the only variation consists in the thermal conductivity model, for which the best estimate option dedicated to a MOX fuel in LWR conditions has been used, being confidential the one for FBR conditions.

In view of what has been done in Chapter 3, the selection of a correlation set for the cladding modelling required a dedicated strategy, at least concerning the reviewed properties. As for the thermal creep, the already existent *Többe* correlation has been chosen as reference equation for the creep strain rate, having shown good agreement also with the new dataset (Figure 3.8); to assess the CDF evolution, instead, the *New LMP* approach has been adopted. The *Többe* correlation has been exploited as reference for irradiation creep as well, being the uncertainties in the development of the *Grossbeck* data fitting considerable. Lastly, a comparison between the composition ranges reported in Table 3.3 regarding DIN1.4970 and that of the " B version" and "L version" of the same steel according to Lemehov (Table 3.7), has been carried out to decide which of the two can be deemed as more representative for the MYRRHA cladding steel response to void swelling. The "B version" has eventually been considered closer to a prototypic DIN1.4970 (the "L version" shows a higher content of Si, useful to increase its swelling strength) and hence it has been taken as reference.

Table 4.4: Physical models and coolant treatment choices for MYRRHA hottest pin simulation [7].

Phenomenon	Adopted model	Input file
	Main phenomena	
Intragranular FGR	URGAS algorithm [45] - single gas atom diffusion in a spherical grain: diffusion coeff. by H. Matzke [46]; constant athermal diffusion coeff. [7]	`FGDiff=6`
Intergranular FGR	Simple grain boundary fission gas behaviour model [7]	`igrbdm=1`
Densification	Pore migration model: model of Dienst et al. [47]; data according to Olander [28]	`idensi=5`
Relocation[c]	LMFBR model, Lassmann calibration [48]	`ireloc=1`
Grain growth	Model by Ainscough [49] and Olsen [50], reviewed by Botazzoli [51][52]	`igrnsz=1`
Fuel restructuring	Pore movement for columnar grains and grain growth for equiaxed grains; pore migration length 1 mm, grain size boundary 50 μm [7]	`istzne=1`
Corrosion on cladding outer surface	Not considered	`icorro=0`
He release	Fit to diffusion coefficients by Federici et al. [53]	`iHe=1`
Power density form factor	TUBNRP burnup model [7]	`iform=1`
Internal rod pressure	Calculated as a function of temperature and moles of fill gas and fission gas release [7]	`ivar1=2`
	Coolant modelling	
Coolant treatment	Treated by TRANSURANUS	*`ikuehl=0`*
Coolant heat transfer coefficient	Calculated by TRANSURANUS	*`ialpha=0`*
Gap thermal conductivity	URGAP model [54] with gas bonding, thermal conductivity of mixture by Lindsay and Bromley [55], accommodation coefficient	*`ihgap=0`*
Geometry of the coolant subchannel	Hexagonal	*`ikueka=1`*
Geometrical representation of coolant channel	Internal flow in pipe (coolant channel represented by an equivalent hydraulic diameter[d])	*`ihydd=1`*

[c] An input number of fuel cracks equal to six has been coupled with the relocation model (`nCracks=6`), according to the linear power produced by the MYRRHA fuel pin [56].

[d] In Section 4.1.1, the conservative hypothesis at the basis of all the TRANSURANUS simulations herein performed has been discussed. Owing to it, the hottest pin belongs to a different subchannel from one batch to another (it can be in an inner, average or corner/edge position), thus the hydraulic diameter should be modified accordingly. To simplify the construction of the input file, however, the same pitch value and arrangement have been used for all the batches, varying only the mass flow rate.

Table 4.5: Material property selection for MYRRHA hottest pin simulation [7].

Property	Correlation	Input file
	Fuel	
General fuel properties selection	MOX fuel for FBRs - Best estimate data by Preusser 1985 [7]	`MPgen_fuel=13`
Fuel thermal conductivity	BE-MOX according to Van Uffelen and Schubert [57]	`ModFuel(6)=31`
	Cladding	
General cladding properties selection	1.4970 austenitic stainless steel annealed and cold-worked according to Többe [32]	`MPgen_clad=2`
Cladding creep strain	Többe correlations: - Thermal creep[e] - Irradiation creep[e]	`ModClad(7)=43` `iiii1=1`
Cladding swelling	Lemehov "B version" [f]	`ModClad(4)=43`
Cladding cumulative damage function	New LMP approach[f]	`iiii3=3`
	Coolant	
General coolant properties selection	LBE	`MPgen_cool=8`

[e] Original implementation in TRANSURANUS code as explained in Annex A.
[f] Original correlation from the work presented in Chapter 3.

4.3 Fuel performance results

In this section, the main TRANSURANUS simulation results of the MYRRHA hottest pin in base irradiation (normal operating) conditions are presented. In the continuation of the analysis, such simulation run is named *reference case* (RC), since the recommended options suggested by the code manual itself have been exploited to model the pin behaviour, as described in detail in Section 4.2.2. For this reason, the following outcomes can be deemed as the most reliable ones at the state-of-the-art.
The simulation outputs are grouped into two distinct sections: one referring to the evolution of fuel and cladding temperatures (Section 4.3.1), the other referring to cladding deformations (Section 4.3.2). As from Table 4.2, indeed, the design limits assumed in this work for normal operating conditions refer either to maximum temperatures reached during the pin in-reactor life, or to maximum deformations suffered by the cladding.
The compliance with the design limits is finally assessed.

4.3.1 Fuel and cladding temperatures

Fuel and cladding temperature behaviours are investigated considering the hottest axial slice. To individuate it, the following considerations have been done: although it is not generally true, the maximum fuel temperature during the whole irradiation history is reached at the BoL, when the

fuel-cladding gap displays its maximum width (hence when it provides the maximum gap thermal resistance), restructuring induced phenomena are still not ongoing as well as oxygen redistribution, and the linear power is at its maximum level. Gap closure (principally induced by different thermal expansion between fuel and cladding, fuel swelling and relocation), restructuring and power lowering, afterwards, tend to produce a temperature decrease. Accordingly, the hottest axial slice (at least under the fuel point of view), has been searched for during the first two batches, as reported in Figure 4.8. The result is that slice 9 is the hottest one, both at the end of batch 1 and at the end of batch 2, and for such reason the following plots refer exactly to that axial slice[34].

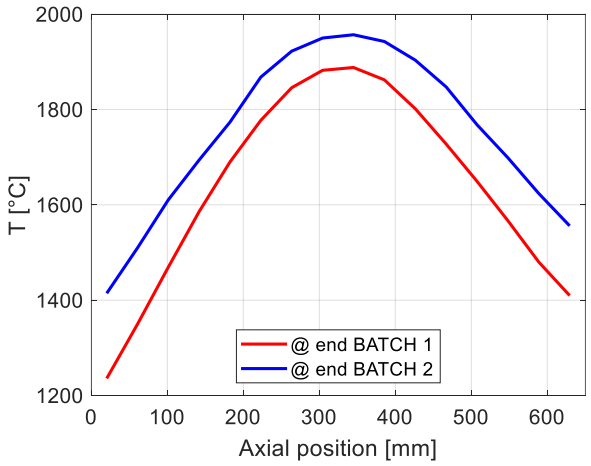

Figure 4.8: Axial profiles of the central fuel temperature during the hottest batches (1 and 2).

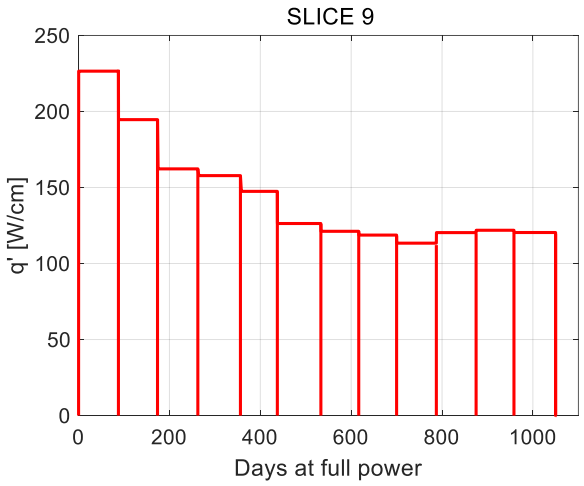

Figure 4.9: Linear power evolution in time at slice 9.

In Figure 4.9, the temporal evolution of the linear power at slice 9 is reported, displaying values higher than the average ones of Figure 4.4.
Figure 4.10 shows the evolution of fuel, cladding and coolant temperatures for the hottest slice. Starting from the coolant, its temperature evolution depends on the linear power and on the flow

[34] This is expected since the maximum linear power is reached at half the fuel length and the cladding temperature is increasingly higher with the axial coordinate (following the coolant evolution).

rate featuring the subchannel the fuel pin belongs to during each batch (according to the conservative hypothesis of Section 4.1). Correspondingly, whereas the temperature evolution at slice 9 strictly follows the shape of the linear power until batch 6, a sharp temperature drop occurs at batch 7, despite the linear power has just slightly lowered with respect to the previous batch. The hottest conditions, indeed, exist in correspondence of the inner pin (characterized by the lowest flow rate, see Figure 4.3) until batch 6, but at batch 7 they shift to a corner pin, cooled by the highest flow rate. Then, they move to an average position at batch 8 causing a rapid temperature rise, and again to a corner one at batch 9, with a new sharp temperature drop (despite, in the meanwhile, the linear power continuously decreases). Finally, at the last three batches, it comes back to the inner position and the temperature returns to strictly follow the linear power evolution.

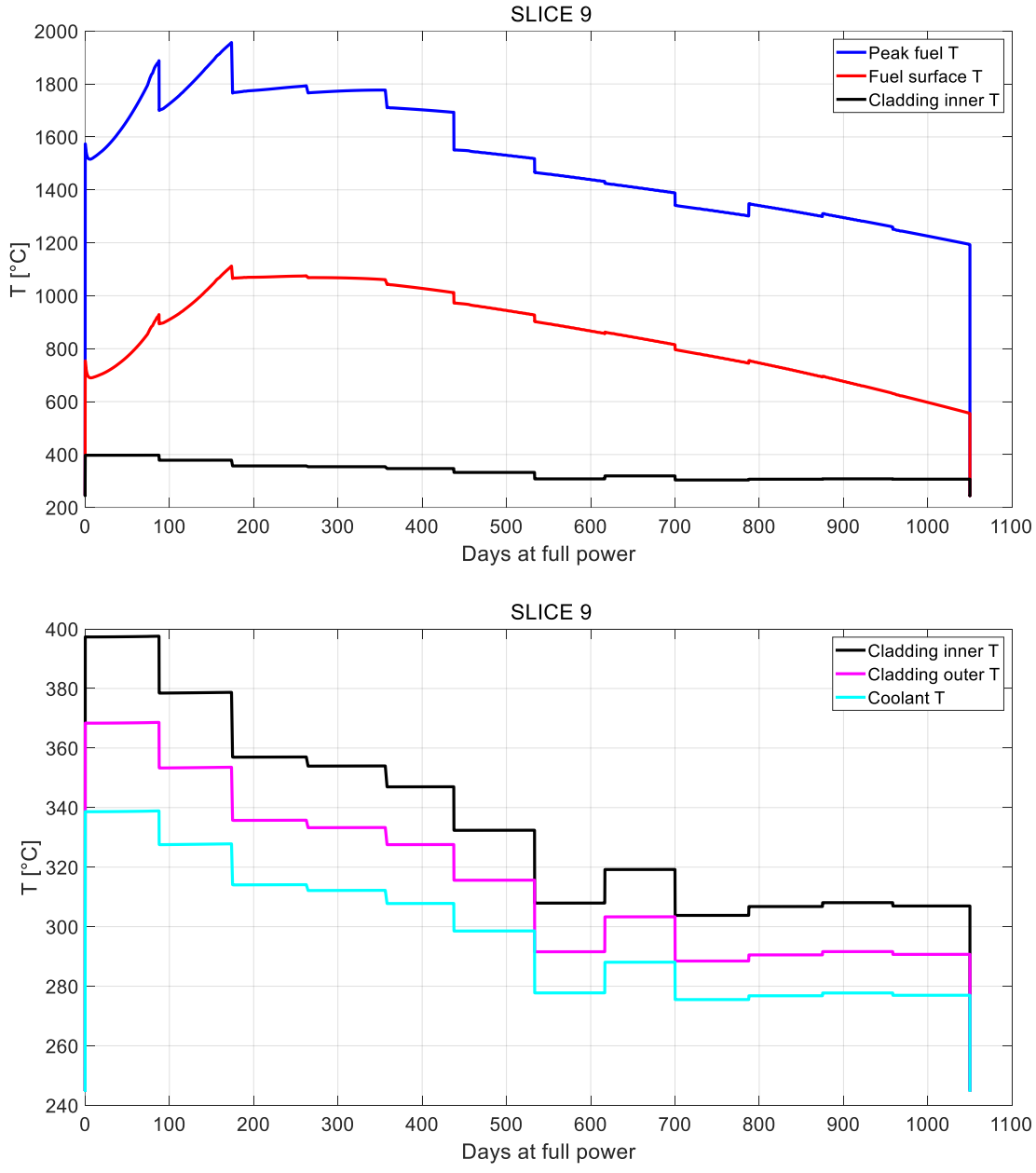

Figure 4.10: Evolution in time of fuel, cladding and coolant temperatures at slice 9.

The cladding outer temperature is derived computing the temperature drop across the coolant, which mainly depends on the calculation of the heat transfer coefficient carried out by TRANSURANUS (`ialpha=0`), exploiting Ushakov's correlation for liquid metals. The cladding inner temperature is eventually obtained adding the cladding temperature drop (dependent on the steel thermal conductivity) to the outer cladding temperature. The outcome is that the cladding inner and outer temperatures follow the same temporal evolution of the coolant one. It can be noticed from Figure 4.10, furthermore, how the maximum (inner) cladding temperature remains always lower than 400 °C (much lower than the operating limits indicated in Table 4.2), reaching little more than 300 °C at the last batch; the cladding temperature drop, instead, ranges from about 30 °C (batch 1) to less than 20 °C (batch 12).
To explain the evolution of fuel surface and fuel central temperatures in time at slice 9 (Figure 4.10), more complex mechanisms must be accounted for, i.e., the gap dynamics and the fuel thermal conductivity. These two effects are treated separately in the two following subsections.

Fuel-cladding gap dynamics

Figure 4.11 shows the temporal evolution of the gap conductance: in cold conditions (i.e., before the reactor start-up, with the coolant inlet temperature at its nominal value), the heat transfer coefficient is roughly equal to 2000 W/m^2K but it doubles right after the first power rise, owing to the partial closure induced by the differential thermal expansion between the fuel pellet and the cladding.
Afterwards, the gap conductance lowers very rapidly during batch 1 and still during batch 2, keeping nearly constant around its minimum value throughout the following two batches. This behaviour is attributed to the rapid accumulation of a considerable amount of fission gases (characterized by a thermal conductivity sensibly lower than the one of the initial fill-gas) inside the gap, prevailing over the progressive reduction of the gap width (Figure 4.12) caused by the ongoing fuel swelling. Figure 4.11, indeed, shows values of the fission gas release (FGR) up to 0.7 at the end of batch 2, meaning that the majority of the gaseous fission products are not retained by the fuel, due to the increasingly higher fuel temperatures.
After having reached its maximum value until batch 4 (i.e., until fuel temperatures begin to go down following the linear power reduction), the FGR starts to decrease in a continuous manner and accordingly the gap conductance grows. This means that, eventually, the progressive gap closure and the gap pressure increment prevail[35].
The evolution of the gap conductance throughout the irradiation history reflects on the behaviour of the temperature jump across the fuel-cladding gap (Figure 4.10), explaining why, after the little reduction following the reactor startup as a consequence of the partial gap closure, it enlarges until batch 4 and then contracts moving towards the final batch 12.

[35] All the mentioned effects contribute to the gap heat transfer coefficient, treated by the `urgap` routine when option `ihgap=0` is selected in the input file.

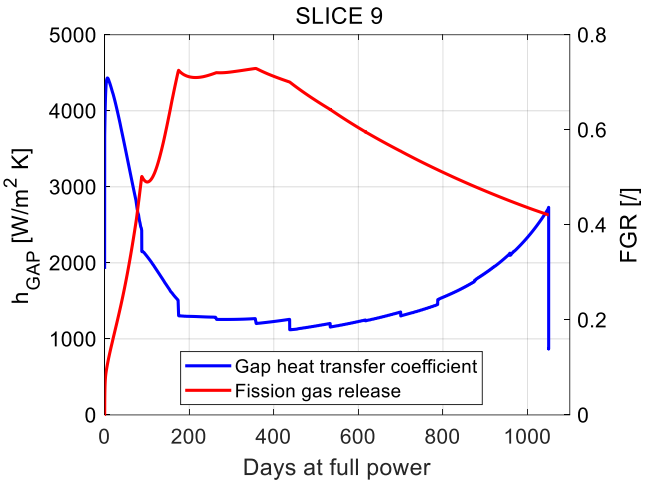

Figure 4.11: Gap conductance and fission gas release (FGR) evolutions in time at slice 9.

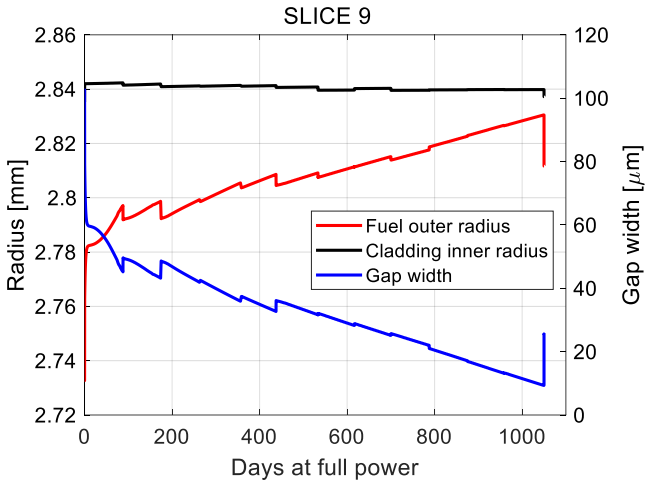

Figure 4.12: Gap evolution in time at slice 9.

Fuel restructuring

The second effect determining the evolution in time of the fuel temperature regimes, besides gap dynamics, is the fuel thermal conductivity, defining the temperature gradient across the fuel pellet.

Dealing with FRs (as MYRRHA is), generally featured by high fuel temperatures, a crucial role in the evolution of the pellet thermal conductivity is played by the restructuring phenomenon (together with all the related mechanisms). The simplest way to identify its occurrence with TRANSURANUS is looking at the evolution of columnar and equiaxed grains regions and the formation of a central hole, as shown in Figure 4.13 concerning slice 9. Considering the plot on the left, it is possible to appreciate that grain growth (causing the formation of equiaxed grains) at slice 9 starts right after the reactor startup and continues until the end of batch 4. On the other hand, the formation of columnar grains begins only towards the end of batch 1 and is accompanied by the build-up of a central hole, both ending with batch 5. The plot on the right, then, shows the axial profiles of the two regions at shutdown, proving that the central hole forms with a very small

radius (maximum radius ~ 0.15 mm), only around the pin mid-plane (i.e., around the axial peak power and temperatures).
The reason of the delay in the central hole and columnar grains region developments is attributed to the insufficiently high fuel temperatures after the first rise to power: indeed, 1600 °C are not enough to trigger the migration of pores across the pellet radius. Accordingly, before fuel restructuring starts, it is necessary that the release of fission gases inside the gap has been sufficiently high to drop the gap conductance consistently, increasing the fuel temperature in turn. When the fuel is hot enough (around 1800 °C), then the mechanism of pore migration can start, eventually building-up the central hole.
For an analogous reason, the process slows down after batch 2, owing to the insufficient fuel temperatures caused by the reduction of the linear power, and definitively ceases after batch 4.

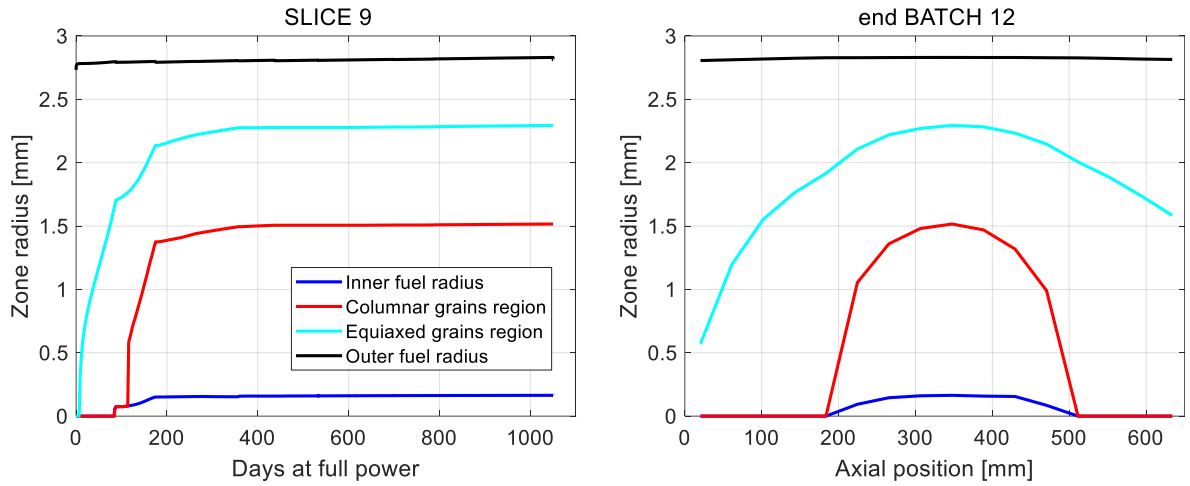

Figure 4.13: Fuel restructuring evolution in time at slice 9 (left) and axial profiles of the central void and grains regions at shutdown (right).

The main effects of fuel restructuring are displayed in Figure 4.14.
On the top left, the evolution of the radial profile of fuel porosity is reported. At the beginning of batch 1, the initial input value equal to 5% holds. The stockpile of pores towards the pellet centreline, consequence of their migration from the columnar grains region, is well visible at the end of batch 1: indeed, fuel porosity has a peak near the just formed central void, whereas a value lower than the initial 5% (and nearly constant) holds in the region they left. Fuel restructuring almost ends at the end of batch 3, when the columnar grains region (suffering a reduction of porosity) has extended and, at the same time, the pores previously accumulated near the centre of the pellet have disappeared, since they have joint each other enlarging the central void. Finally, at the end of the irradiation history, the reached fuel burnup level entails that porosity is increased on average, but its radial profile still displays the effect of the restructuring previously occurred.
Fuel porosity has a strong influence on fuel thermal conductivity, together with fuel temperature and burnup (see Figure 4.20); on the other hand, the reference model chosen for the simulation in TRANSURANUS does not account for the dependence on both the deviations from stoichiometry (oxygen redistribution) and on the plutonium content. As from Figure 4.14 (left), the two curves

are almost complementary, that is, when the porosity is high, the thermal conductivity is low and vice-versa[36].

Although the plutonium content effect is not included in state-of-the-art thermal conductivity correlations implemented in TRANSURANUS, plutonium radial redistribution is considered in the code and affects the power distribution. Its development can be seen in Figure 4.14, on the right. Starting from a uniform radial enrichment characterizing the fresh fuel, plutonium migration towards the centre of the fuel pellet occurs during restructuring, as displayed by the radial profile at the end of batch 1 and especially at the end of batch 3, reaching a peak content close to 31%. The fissile depletion explains the shift of the curve downwards at the end of batch 12.

Coming back to Figure 4.10, the temperature drop within the fuel is nearly constant during the whole irradiation history. This means that, concerning the initial batches, the effects of restructuring are too weak for having a significant influence on the fuel thermal resistance and, concerning the final batches, the degradation of the fuel thermal conductivity with burnup is compensated by the previous accumulation of fissile plutonium near the pellet centre.

The main conclusion, hence, is that gap dynamics is dominant in determining the fuel temperature profiles (being nearly constant the temperature drop within the fuel itself). Accordingly, the maximum peak fuel temperature is reached at the end of batch 2 when the minimum gap heat transfer coefficient is reached and before the linear power lowering becomes decisive, and approaches roughly 2000 °C.

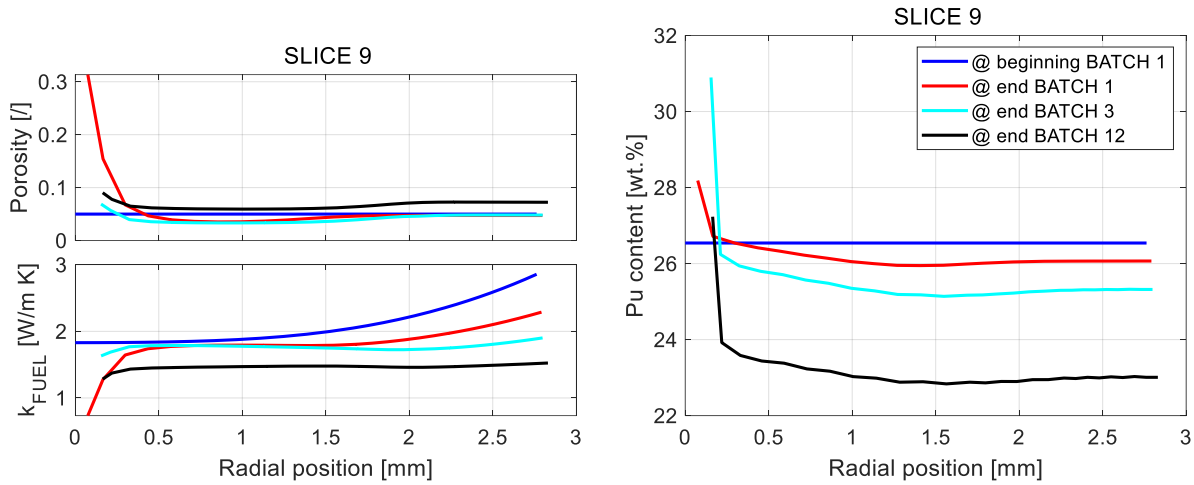

Figure 4.14: Effects of fuel restructuring at different irradiation times at slice 9.

[36] The temperature dependence, instead, causes the thermal conductivity to increase towards the pellet periphery (considering the temperature regime associated to MYRRHA normal operating conditions, i.e., ~1200-1900 °C for the hottest pin).

4.3.2 Cladding deformation

Fuel and cladding temperature trends have been investigated for the hottest slice (slice 9) to identify the worst possible thermal conditions (at least from the fuel point of view). A similar approach is chosen to analyse the MYRRHA cladding strain. The axial slice displaying the maximum permanent deformation has been selected as the one to focus on, being the majority of the design limits on strains reported in Table 4.2 referred to irreversible components (i.e., creep, swelling and plastic).

Figure 4.15 shows the outer cladding profile at different irradiation times and the correspondent instantaneous tangential strain. At the initial batches (batch 1 and batch 4), thermal strain dominates on the other components, therefore the cladding outer radius profile follows the variation of the cladding temperature, being progressively higher with the axial coordinate. Afterwards, the irreversible strain contributions become important, changing the shape of the outer cladding radius[37]. At shutdown, with the coolant still at its nominal inlet temperature, the fuel pin is in thermal equilibrium, so all the axial slices share the same thermal and elastic strain components. In these conditions, it is possible to identify slice 11 as the one suffering the highest permanent tangential strain. Accordingly, the following plots refer to such slice.

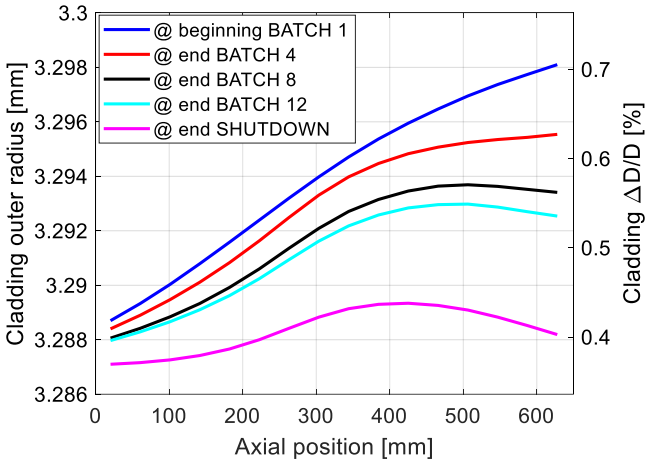

Figure 4.15: Axial profiles of the cladding outer radius at different irradiation times.

In Figure 4.16, the evolution of the three irreversible cladding strains is reported for slice 11, together with the total permanent one. First of all, it can be noticed that the permanent strain is very small, reaching a maximum value around 0.07%. Being the total cladding strain at shutdown roughly equal to 0.43%, this means that the three irreversible strain components are very limited in magnitude, since their sum is five times smaller than the reversible ones (thermal and elastic contributions). The largest part of the permanent cladding strain, then, is due to swelling, which actually can be considered as the only contributor, given that the equivalent creep deformation is nearly null throughout all the irradiation history, and no plastic deformation is observed.

[37] The final shape of the cladding outer radius is not easy to predict, especially owing to the void swelling contribution. Even though the highest neutron flux is reached at the pin mid-plane, indeed, its bell-shaped dependence on temperature makes difficult to identify where the maximum swelling occurs.

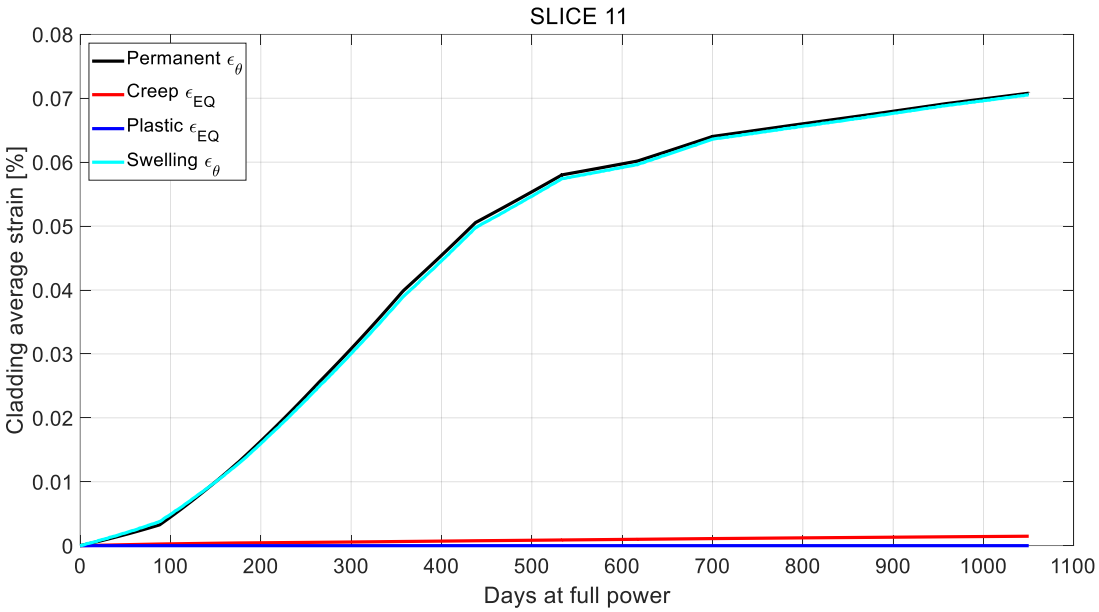

Figure 4.16: Evolution in time of the irreversible cladding strain components at slice 11.

Plastic strain component

Additional details are provided in this subsection concerning the behaviour in time of the plastic deformation, since it will be of particular interest dealing with the accidental scenarios (presented and analysed in Chapter 5).

In Figure 4.17, the temporal evolution of the gap size is shown for slice 11. Starting from its nominal value, a rapid gap width reduction happens at startup, owing to the differential thermal expansion between the fuel and the cladding. Afterwards, the outer fuel radius grows progressively due mainly to fuel swelling (3% at shutdown), causing the gap to move towards closure[38]. A complete gap closure, however, never verifies, neither at slice 11 (where the minimum width reaches 10 μm), nor in any other. In absence of FCMI, a contact pressure does not develop, thus no yielding is reached at slice 11 as well as in any other slice.

Without contact pressure, the only sources of cladding stress are thermal gradients and coolant/gap pressures[39]. Summing their effects, the resultant cladding average equivalent stress is very low, with a maximum under 30 MPa at the beginning of irradiation, as displayed in Figure 4.18. In addition, note from the figure that cladding works under external pressure until the half of batch 2 (remember the initial fill-gas pressure equal to 0.1 MPa, and the coolant one equal to 0.6 MPa); then, due to the fission gas release from the fuel, the working condition switches to internal pressure, reaching a maximum of about 1.6 MPa at the end of irradiation, before shutdown.

[38] The presence of small jumps in the gap size evolution is the consequence of the linear power changes between one batch and the successive one, causing a sudden fuel and cladding temperature variation and, eventually, affecting their thermal expansion.

[39] The gap pressure is determined by the sum of fill-gas pressure and the one of fission products gradually released by the fuel.

The magnitude of the cladding equivalent stress is useful to explain the low creep strain contribution as well. The low equivalent stress values, indeed, are insufficient to trigger an effective creep deformation, especially as far as the thermal mechanism is of concern (considering also the simultaneous low temperatures).

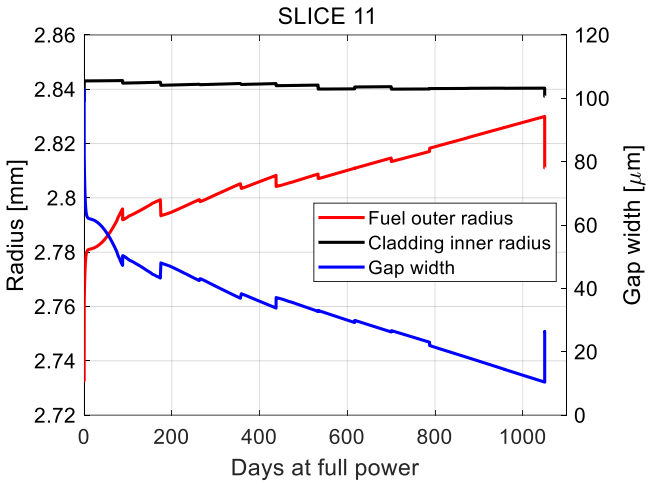

Figure 4.17: Gap evolution in time at slice 11.

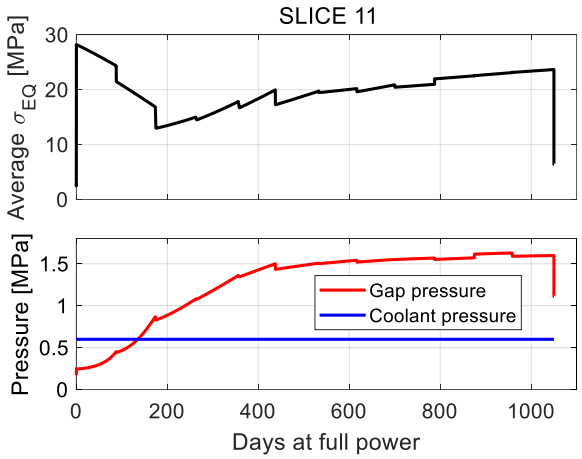

Figure 4.18: Cladding average equivalent stress and loading pressures at slice 11.

4.3.3 Assessment of design limits

Table 4.6 summarizes the maximum simulated values of the quantities to be monitored for the assessment of the design limits in MYRRHA normal operating conditions.

The outcome is a complete compliance with the design limits reported in Table 4.2. In particular:

- The maximum peak fuel temperature sets 40 °C below the indicative threshold, constituting the minimum margin from the design limits;
- The maximum peak cladding temperature is reached at the uppermost slice and during the batch with the highest linear power (batch 1);

- The maximum inner gas pressure does not occur at the end of the irradiation history, rather at the end of batch 11, meaning that the higher temperature existing at batch 11 wins over the further accumulation of gases in the gap happening during batch 12;
- Whereas the maximum permanent tangential strain displays at slice 11 at shutdown (as described in Section 4.3.2), the maximum instantaneous one verifies at slice 16 where the cladding temperature is the highest, owing primarily to the thermal strain contribution;
- Both the maximum thermal creep strain and the plastic one are always null as well as the cumulative damage function.

Table 4.6: Maximum temperatures and deformations for base irradiation – reference case.

Quantity	Maximum value	Position
Peak fuel temperature	1957 °C	slice 9 @ end batch 2
Peak cladding temperature	449 °C	slice 16 @ end batch 1
Inner gas pressure	1.63 MPa	@ end batch 11
Cladding ΔD/D	0.702%	slice 16 @ batch 1
Equivalent thermal creep strain	0.000%	-
Equivalent irradiation creep strain	0.005%	slice 8 @ shutdown
Swelling strain	0.077%	slice 11 @ shutdown
Equivalent plastic strain	0.00%	-
Cumulative damage function	0.000	-
Permanent tangential strain	0.08%	slice 11 @ shutdown

4.4 Sensitivity analysis

The reference results of the fuel performance analysis carried out on the MYRRHA hottest pin, reported and discussed in the previous section, correspond to a rather relaxed scenario, especially from the cladding deformation point of view, due to the low linear power and the low final fuel burnup featuring MYRRHA base irradiation.

Those outcomes have been obtained employing the reference TRANSURANUS correlations and models (reference case). Nevertheless, many uncertainties exist, especially concerning fuel properties like the thermal conductivity and key phenomena like creep and swelling (of both fuel and cladding). Whereas the former introduce an interval of plausible values, the latter may change remarkably with the experimental setup, producing correlations with huge differences between each other. Accounting for such uncertainties can lead to very different final scenarios in terms of fuel pin performance.

Hence, a sensitivity analysis on TRANSURANUS models is carried out, with two objectives:

1. To identify a *worst case* (WC), i.e., a set of input models leading to the worst possible situation in terms of fuel performance, according to selected figures of merit of interest;
2. To assess the worst case compliance with the considered design limits.

To be underlined is the deterministic approach adopted for the sensitivity analysis: that is, the worst case scenario obtained is seen as a threshold scenario, exploitable for evaluating the limit

conditions in which the hottest pin could work, based on the models available in TRANSURANUS. In this way, a conservative assessment of the MYRRHA pin performance is carried out[40].
Complying with the deterministic approach, a multivariate procedure is adopted to perform the sensitivity analysis, i.e., the TRANSURANUS code is run with every possible combination of selected correlations in the input file, and the figures of merit of interest are recorded.
In the following, the figures of merit chosen to direct the sensitivity analysis and the models included inside the multivariate scheme are presented.

4.4.1 Figures of merit

The selected figures of merit principally correspond to quantities involved in the design limits (see Table 4.2), with the purpose to research among all possible sensitivity scenarios those ones characterized by their maximum/minimum value.
Two worst conditions are looked for: one featured by the highest possible maximum peak fuel temperature, the other by the highest possible cladding deformation[41]. The first one has been chosen because fuel temperature is the quantity most approaching the design limits in the reference case, hence deemed as the most critical for MYRRHA in normal operating conditions. As for the second, instead, the highest permanent deformation is researched, summing up all the irreversible strain components.

4.4.2 Model options

The properties and phenomena most affecting the identified figures of merit and featured by the highest uncertainties are involved in the analysis.
From Section 4.3.1, the maximum peak fuel temperature is reached at the end of batch 2, that is rather at the beginning of the irradiation history. In such situation, fuel thermal conductivity has the dominant impact on the maximum fuel temperature, so it has been included in the sensitivity. Models affecting the FGR (so the pellet surface temperature and the central one) have not been considered, since the available options would not imply significant variations (especially because the observed fission gas release is already significant).
As for the cladding deformations, model options for thermal creep, irradiation creep and void swelling have been selected. In addition, fuel swelling has been included, having an important influence on gap dynamics and leading to potential cladding plastic deformations in case of gap closure with sufficient contact pressure. Fuel thermal conductivity itself is very important in this respect, affecting fuel temperatures and thus its thermal expansion. The same holds for fuel and cladding thermal expansion coefficients and cladding thermal conductivity; however, uncertainties on such parameters are typically negligible. The effects of pellet relocation, instead, have been assessed through a monovariate analysis (i.e., analysing the consequences on gap width

[40] Dealing with fuel performance, it is not easy to understand what is conservative and what is not, meaning that to keep inside the simulation all those correlations providing the most pessimistic results for each phenomenon/property taken singularly is not enough, since their interaction complicates the final outcome. For example, cladding creep is undesired since it contributes to cladding deformation; nevertheless, it is beneficial in case of FCMI, relaxing cladding stresses. The only way to overcome the problem is through the sensitivity analysis.
[41] Generally, it is not guaranteed that one single scenario envelops both the selected worst conditions. They can be reached by two distinct combinations of models.

varying only the relocation model with respect to the reference case), from which the relocation impact proved to be less influential with respect to the other aforementioned phenomena [42].
The considered options (all addressed to FR conditions) are summarized in Table 4.7 and briefly explained in what follows.

Table 4.7: Model options selected for the sensitivity analysis [7].

Phenomenon/Property	Options	Input file
Cladding thermal creep	- Többe correlation [32][g]	`ModClad(7)=43`
	- Modified Delville correlation[h]	`ModClad(7)=44`
Cladding irradiation creep	- Többe correlation [32] [g]	`iiii1=1`
	- Grossbeck data fitting[h]	`iiii1=2`
Cladding swelling	- Lemehov "B version" [h]	`ModClad(4)=43`
	- Lemehov "L version" [h]	`ModClad(4)=44`
Fuel thermal conductivity	- BE-MOX according to Van Uffelen and Schubert [57]	`ModFuel(6)=31`
	- CONSERVATIVE-MOX according to Van Uffelen and Schubert [57]	`ModFuel(6)=35`
	- MOX according to Carbajo et al. [58]	`ModFuel(6)=32`
Fuel swelling	- BE-MOX according to Preusser [48]	`ModFuel(4)=13`
	- MOX according to Freund et al. [59]	`ModFuel(4)=11`

[g] Original implementation in TRANSURANUS code as explained in Annex A.
[h] Original correlation from the work presented in Chapter 3.

Cladding phenomena

Thermal creep, irradiation creep and void swelling alternative options include the correlations deeply investigated in Chapter 3, i.e., the formulae developed fitting data found in the open literature. Adopting such other models, it is expected to obtain higher thermal creep and irradiation creep strains (Figure 3.9, Figure 3.14), while a lower swelling (Figure 3.16).

Fuel swelling

The alternative option has been selected, among all the available, as the one providing a greater swelling with respect to the reference case (*BE-MOX according to Preusser*), searching for possible gap closure scenarios.
Although both the correlations consider a constant swelling rate equal to 0.65 %/at.% when the gap closes, they differ when the contact pressure is still null (which is the usual condition for MYRRHA hottest pin, Figure 4.17): a constant rate of 2 %/at.% holds for the *MOX according to Freund et al.* model, whereas the *BE-MOX according to Preusser* one contemplates the same value for burnups lower than 1 at.%, while a constant 1.2 %/at.% otherwise.
The comparison is reported in Figure 4.19, supposing a gap closure happening at 5 at.%.

[42] To discard a negligible phenomenon, focusing on the primary ones, is useful to limit the number of scenarios to be analysed, especially whether it is already notable.

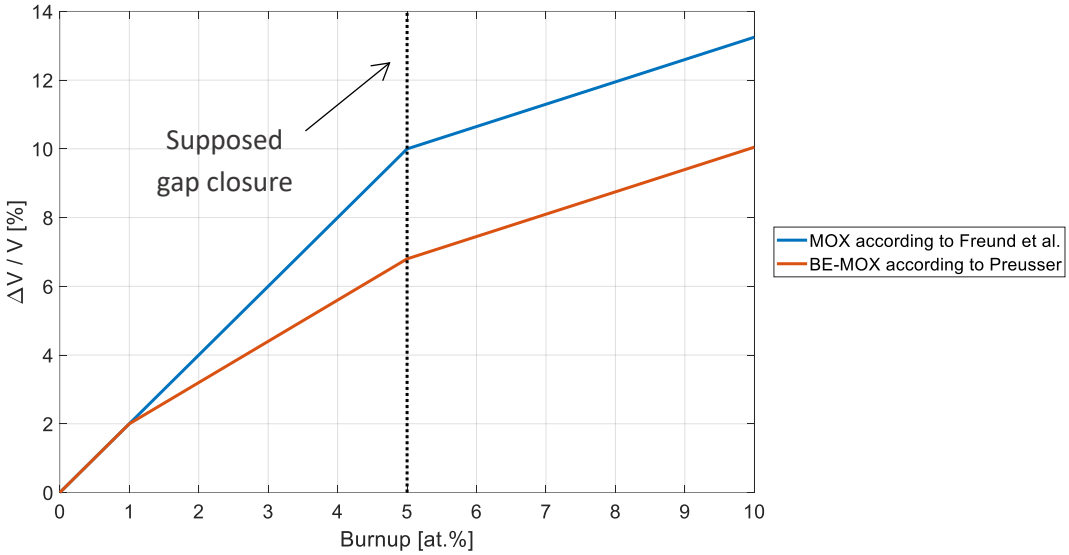

Figure 4.19: Comparison between the two fuel swelling options considered in the sensitivity analysis, as a function of burnup.

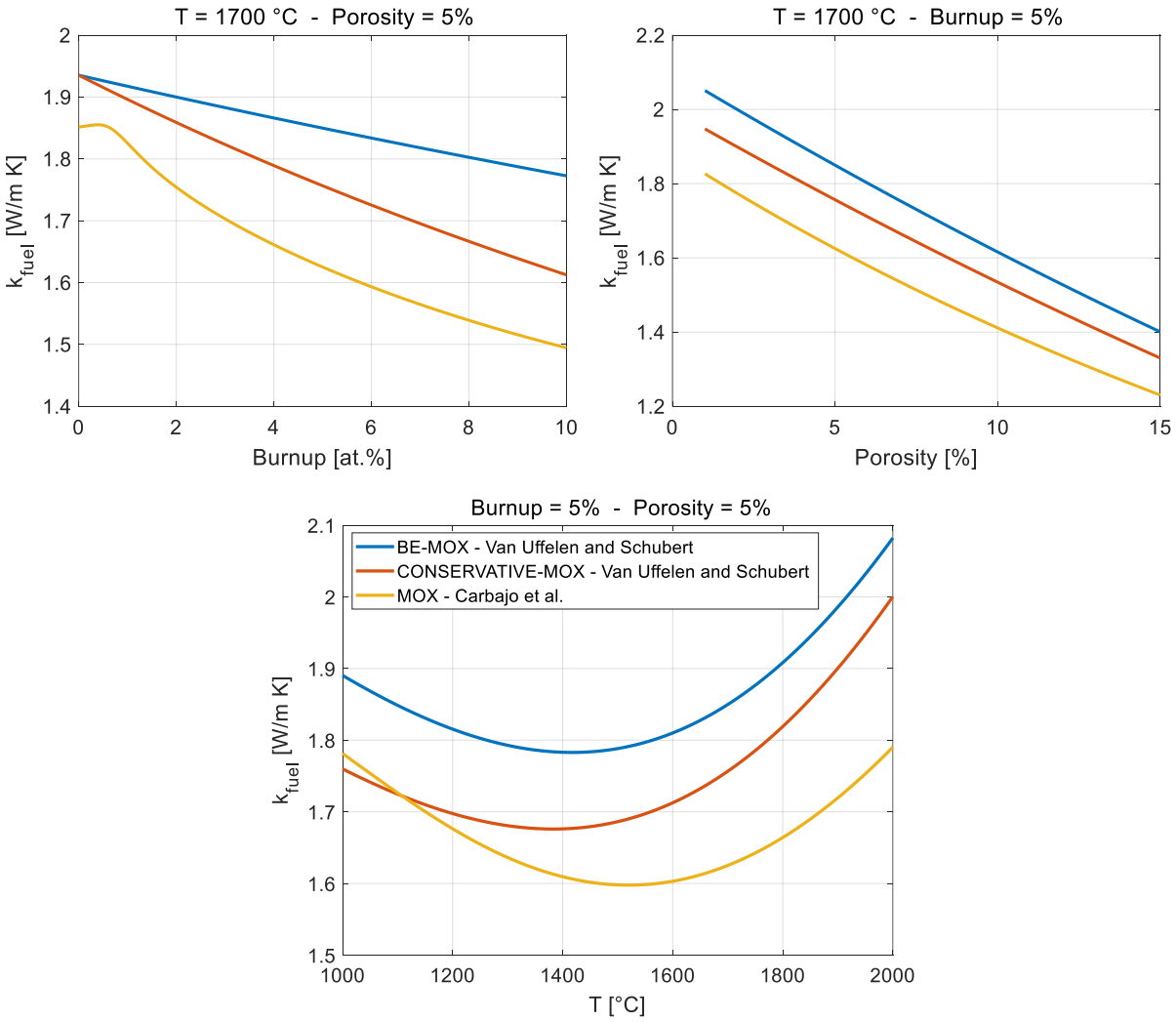

Figure 4.20: Comparison between the fuel thermal conductivity options considered in the sensitivity analysis at representative burnup, porosity and temperature, with fixed O/M=1.97 and Pu=30%.

Fuel thermal conductivity

Regarding the fuel thermal conductivity, only correlations supplying values smaller than the reference one have been taken into consideration, being of interest scenarios with higher temperatures.

The *BE-MOX according to Van Uffelen and Schubert* and the *CONSERVATIVE-MOX according to Van Uffelen and Schubert* models were developed starting from the same measurements, with the second one corresponding to the data lower bound. Both take into account the dependencies on porosity, temperature and burnup, while plutonium content and stoichiometry effects are not considered. The *MOX according to Carbajo et al.* correlation, instead, misses only the explicit effect of the plutonium content.

In Figure 4.20, the three correlations are compared varying one dependency between temperature, porosity or burnup at a time and fixing the other two, as well as plutonium and stoichiometry: the *MOX according to Carbajo et al.* model generally provides the lowest fuel thermal conductivity values.

4.5 Worst case fuel performance results

Considering the five phenomena/properties selected for the sensitivity analysis and the corresponding options (Table 4.7), 48 combinations of input models are gathered by means of the multivariate scheme. Each of the resulting scenarios have been simulated and the magnitude of the two figures of merit, chosen as guidelines for the analysis, have been evaluated. The outcome is that two worst cases leading to the highest peak fuel temperature exist, as well as two other worst cases leading to the highest cladding permanent deformation. The correlation sets characterizing all the worst cases are reported in Table 4.8.

A comparison between the reference fuel pin performance results and the worst conditions is discussed in the following sections. Note that just the figures more characterizing the correspondent worst case are reported: that is, only quantities related to fuel temperature are displayed for the worst case in terms of fuel temperature, whereas deformation trends, which are not of interest for that scenario (because they are not the worst conditions), are not shown. The same holds for the worst case in terms of cladding deformation, for which the fuel temperature evolution is not disclosed.

Table 4.8: Models leading to the worst cases (WC) in MYRRHA base irradiation conditions.

Phenomenon/Property	WC - Fuel temperature	WC - Cladding deformation
Cladding thermal creep	Not relevant	Not relevant
Cladding irradiation creep	*Grossbeck data fitting*	*Grossbeck data fitting*
Cladding swelling	*Lemehov "B version"*	*Lemehov "B version"*
Fuel thermal conductivity	*MOX according to Carbajo et al.*	*CONSERVATIVE-MOX according to Van Uffelen and Schubert*
Fuel swelling	*BE-MOX according to Preusser*	*MOX according to Freund et al.*

4.5.1 Worst case - Fuel temperature

Two equivalent worst cases in terms of peak fuel temperature have been obtained, as previously said. As from Table 4.8, they are characterized by the same correlations for modelling the cladding irradiation creep and void swelling response, the fuel swelling and thermal conductivity; the only difference between the two sets is the cladding thermal creep model, which does not play any impact in the simulation (its contribution to cladding deformation is null).

To justify the input set is not too difficult in this case. The model combination, indeed, supplies the widest possible gap and, hence, the minimum possible conductance (the fuel tends to swell a little, but the two cladding correlations provide the highest cladding diameter increment). Moreover, the fuel thermal conductivity is the lowest among the three options, affecting the temperature gradient across the pellet itself.

In Figure 4.21, the evolution in time of fuel and cladding temperatures is reported for slice 9, which has proven to be, as in the reference analysis, the hottest one. Comparing the reference and the worst scenarios, identical trends are followed by the cladding inner temperature. On the other hand, fuel surface temperatures are very similar during the first four batches, while they spread as irradiation proceeds towards the EoL. Peak fuel temperatures strongly differ as well, by a nearly constant difference throughout the irradiation.

Figure 4.22 provides a justification for the different temperature trends between the two scenarios. Considering the gap conductance (on the left), its value in the worst case is just slightly lower than in the reference case until batch 4, owing to the higher FGR (in turn caused by higher fuel temperatures). Afterwards, the heat transfer coefficient grows less than in reference conditions, partly because of the wider gap (as predicted by the alternative cladding models selected). Such behaviour reflects on the fuel surface temperature, higher than in the reference case of almost 200 °C before shutdown.

The increased temperature drop within the pellet is the offspring of the fuel thermal conductivity model characterizing the worst case. As from Figure 4.22 (right), its average value decreases with respect to the reference scenario, causing the peak fuel temperature rise of 65 °C indicated in Table 4.9, crossing the design limit for normal operating conditions considered for ALFRED reactor.

The peak cladding temperature, instead, does not change at all with respect to the reference scenario, whereas just a little difference is predicted for the inner gas pressure, owing to the increased fuel temperatures.

Table 4.9: Maximum temperatures for base irradiation – worst case.

Quantity	Maximum value	Position
Peak fuel temperature	2022 °C	slice 9 @ end batch 2
Peak cladding temperature	449 °C	slice 16 @ end batch 1
Inner gas pressure	1.87 MPa	@ end batch 11

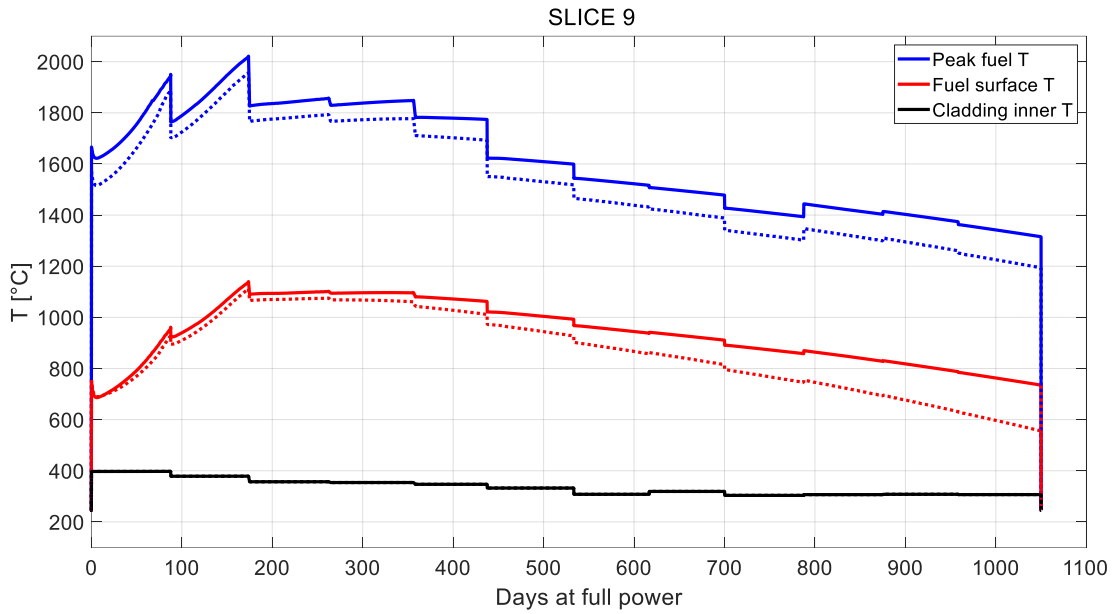

Figure 4.21: Evolution in time of fuel and cladding temperatures at slice 9 in RC (dotted line) and in WC (solid line).

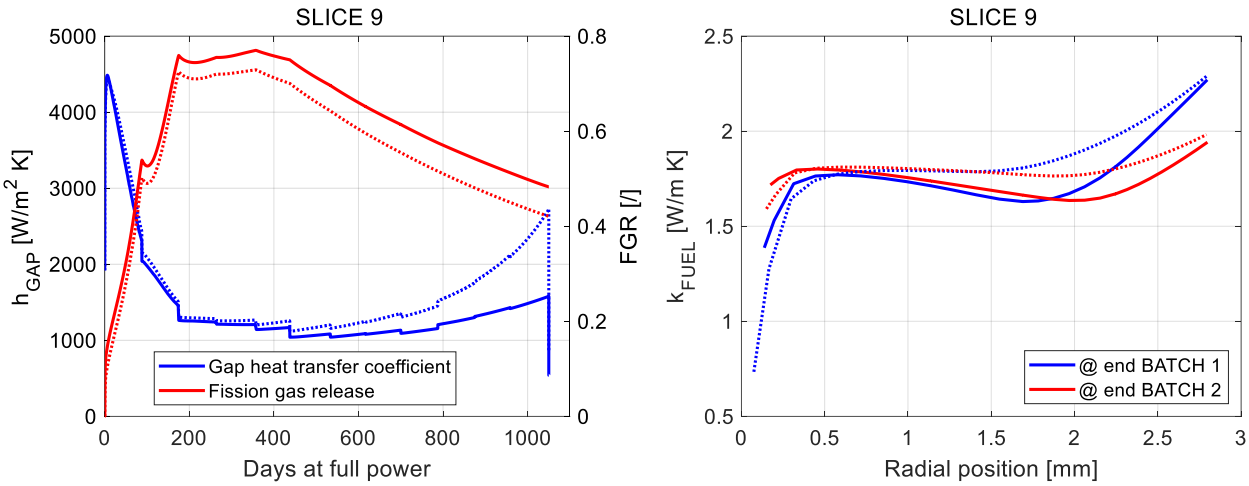

Figure 4.22: Gap conductance and fuel thermal conductivity influencing fuel temperatures at slice 9 in RC (dotted line) and WC (solid line).

4.5.2 Worst case - Cladding deformation

Two worst cases in terms of cladding deformation have been found (Table 4.8), again owing to the irrelevance of the thermal creep model. As regards the other phenomena/properties, *Grossbeck data fitting* and *Lemehov "B version"* are the main responsible for the identified scenarios, since they provide the highest irreversible strains for irradiation creep and void swelling respectively (Figure 3.14, Figure 3.16).

The *MOX according to Freund et al.* model for fuel swelling (predicting the highest fuel deformation) and the *CONSERVATIVE-MOX according to Van Uffelen and Schubert* for the fuel thermal conductivity complete the worst scenarios. This time, to understand the reasons leading

to the presence of such two fuel models is not straightforward: whereas in the worst case in terms of fuel temperature the phenomena affecting the peak fuel temperature display at BoL, here all the irradiation history contributes to determine the final cladding deformation, making the outcome difficult to be predicted.

Figure 4.23 shows the outer cladding profile in the worst case scenario, useful to locate the axial slice suffering the highest permanent tangential strain, as done for the reference situation (Section 4.3.2). It is clear from the plot how the scenario has changed with the new set of correlations: the slice suffering the highest permanent deformation has shifted to slice 9 (which is the hottest slice as well), displaying a shape quite similar to the neutron flux and the linear power one (Figure 4.4 and Figure 4.5).

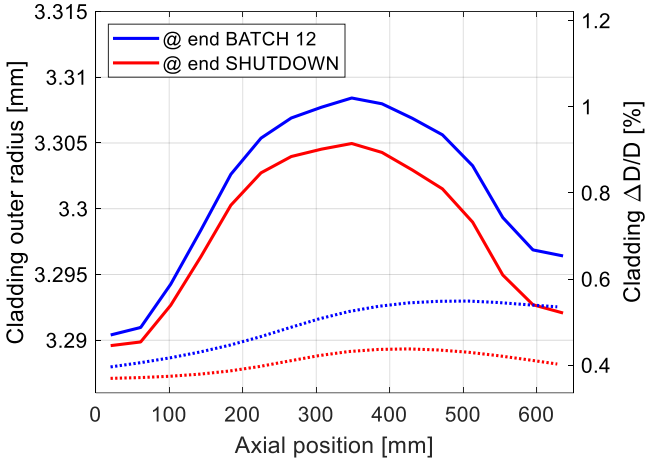

Figure 4.23: Axial profiles of the cladding outer radius at EoL in RC (dotted line) and WC (solid line).

Accordingly, the evolution with time of the irreversible cladding strain components is studied for slice 9, as in Figure 4.24. The total permanent strain reveals one order of magnitude higher than in the reference case, reaching 0.62% at shutdown (as reported in Table 4.10). Specifically, the creep strain contribution (previously very close to zero) has strongly increased, becoming dominant on the other strain components. The reason of the discrepancy lays in the irradiation creep model: as from Figure 3.14, the choice of the *Grossbeck data fitting* entails an acceleration of such creep mechanism by three orders of magnitude, becoming the driving force of the permanent strain. The void swelling effect, instead, is very similar to that characterizing slice 11 in the reference case (the swelling options are the same), and the plastic strain is still null[43].

Finally, thermal and elastic strains explain again the difference between the permanent and the instantaneous total cladding deformation (Table 4.10). The maximum for the second one displays towards the EoL instead of being at BoL (as in the reference case), underlining once more the importance of the irradiation creep contribution.

As for the design limits required in normal operating conditions, all of them are respected even in the worst case here considered, as inferred from Table 4.10.

[43] Given that the swelling strain is identical to the reference case and the plastic one remains null, irradiation creep justifies the presence of the maximum permanent strain in correspondence of slice 9. The irradiation creep flow law, indeed, shows a square root dependence on the neutron flux, which has its maximum exactly at the pin mid-plane.

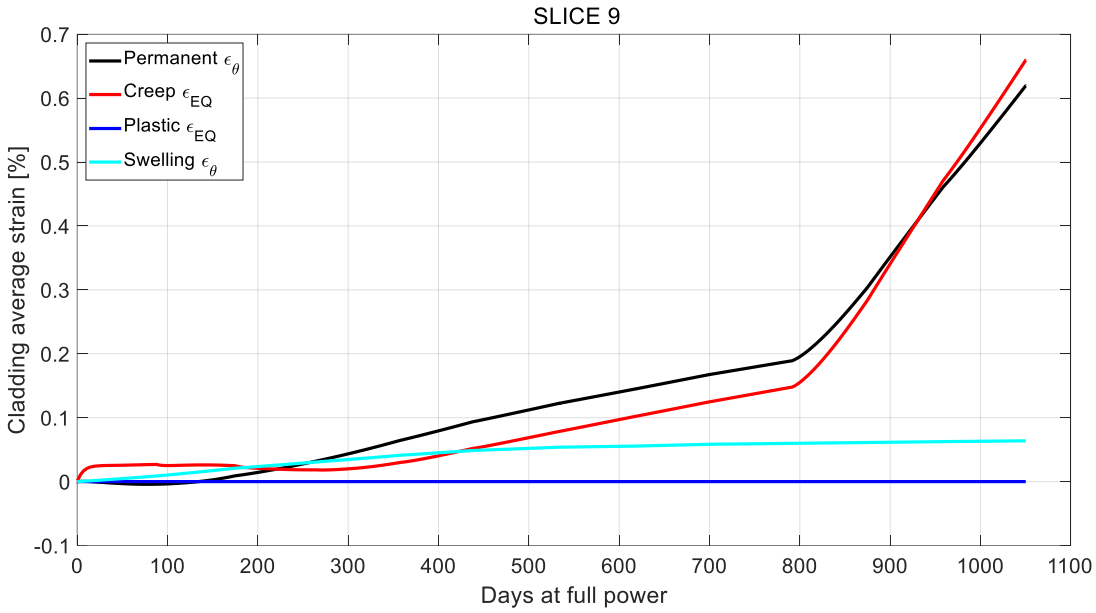

Figure 4.24: Evolution in time of the irreversible cladding strain components at slice 9 in WC.

Table 4.10: Maximum deformations for base irradiation – worst case.

Quantity	Maximum value	Position
Cladding ΔD/D	1.008%	slice 9 @ end batch 12
Equivalent thermal creep strain	0.000%	-
Equivalent irradiation creep strain	0.859%	slice 7 @ shutdown
Swelling strain	0.077%	slice 11 @ shutdown
Equivalent plastic strain	0.00%	-
Cumulative damage function	0.000	-
Permanent tangential strain	0.62%	slice 9 @ shutdown

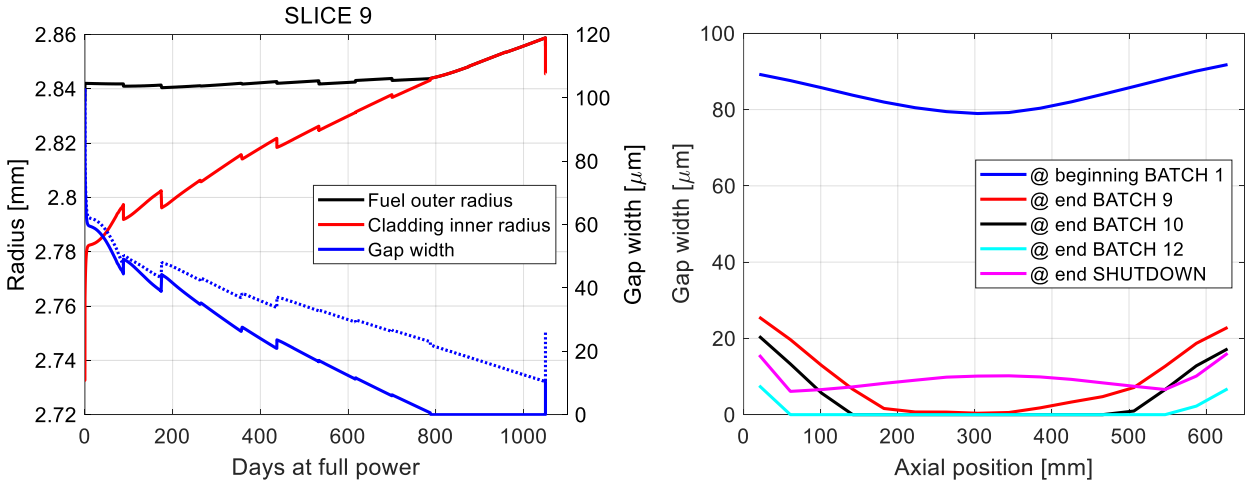

Figure 4.25: Gap evolution in time at slice 9 in RC (dotted line) and WC (solid line), and axial gap width at different irradiation times in WC.

Plastic strain component

Concerning the cladding plastic deformation, in the reference case its absence has been attributed to the open fuel-cladding gap throughout the entire base irradiation, so unable to induce a contact pressure by FCMI, deemed as the only way to reach yielding.

In the worst case, the faster fuel swelling provided by the *MOX according to Freund et al.* model (contributing to more than 4% of fuel tangential strain at EoL) is the primary origin of gap closure happening at the beginning of batch 10 for slice 9, as it is possible to see in Figure 4.25, on the left. The figure on the right, shows how gap closure axially extends to a big portion of the fuel pin already at the end of batch 10, until achieving almost complete closure just before shutdown. In every axial slice, however, no plastic strain is predicted by TRANSURANUS.

In correspondence with gap closure, a contact pressure between fuel and cladding develops at the beginning of batch 10 for slice 9 (Figure 4.26), since the pellet deformation is much faster than the cladding one. The outcome is a rapid increment of the equivalent cladding stress, although reaching a maximum value around 30 MPa, far from the yielding limit (which lies nearby 450 MPa, see Figure 3.6). The limited cladding equivalent stress value is partly attributed to a stress relaxation by irradiation creep: with gap closure, indeed, the cladding loading condition switches from imposed stress to imposed deformation, allowing the mechanism to occur.

Low cladding stresses and temperatures justify the irrelevancy of thermal creep on the worst case identification: the two conditions are not sufficient to trigger a creep mechanism fast enough to produce an irreversible deformation. Stress and temperature maxima, moreover, display at opposite time instants during the irradiation history: during the final batches for the first one (apart from the peak at batch 1, which however persists for a very small time), during the BoL for the second.

Being the thermal creep contribution null, it has been deemed useless to test other correlations to evaluate the cladding cumulative damage function, since the expected values are far below its design limit.

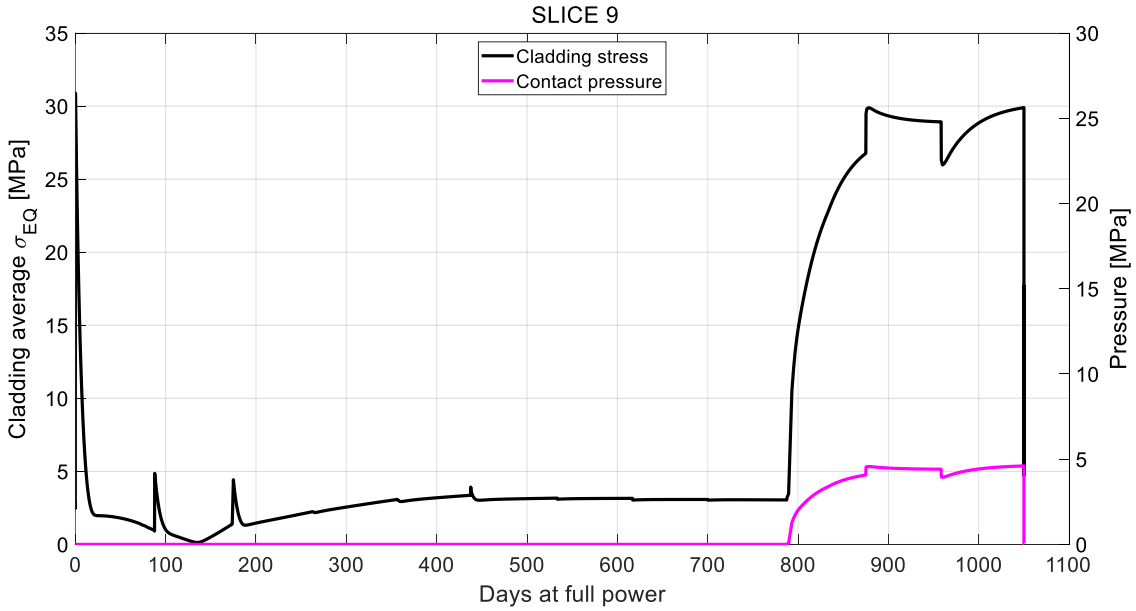

Figure 4.26: Evolution in time of cladding average equivalent stress and contact pressure at slice 9 in WC.

Chapter 5

MYRRHA fuel performance analysis in accidental conditions

After the extension of the TRANSURANUS code applicability to the simulation of DIN1.4970 cladding steel behaviour and the performance analysis of MYRRHA fuel pins in normal operating conditions, this part of the thesis work is devoted to the conservative assessment of eventual pin failures occurring during a particular overpower transient selected as one of the design basis accidents for MYRRHA reactor. Main goal is to investigate the MYRRHA hottest pin response under the selected transient conditions, assessing the compliance with specific design limits.

Firstly, the overpower transient and the identification of its worst possible development are addressed in Section 5.1, explaining also how the scenario are simulated in TRANSURANUS and which are the design limits suitable for such accidental conditions.

The following four sections report the outcome of the simulations considering the occurrence of the overpower transient at four different time instants during the base irradiation history, representative of BoL, mid-life and EoL conditions. Similarly to Chapter 4 (normal operating conditions), the fuel pin behaviour is studied considering the reference set of input correlations for fuel and cladding properties/phenomena as well as the worst case one, to account for the different modelling options. To such scope, the same sensitivity approach already applied for the normal operation analysis is employed.

In light of the results obtained, Section 5.6 investigates the power required to exceed the design limits, providing a useful indication both for the future licensing phase and also for the reactor design and its better exploitation.

5.1 Accidental conditions

The transient overpower scenario considered in this work is a *beam power jump* (BPJ)[13], happening during the operation of MYRRHA reactor in subcritical configuration (i.e., control and shutdown rods extracted, linear accelerator and reactor core coupled by means of the spallation target, see Section 2.2).

The transient initiating event is a sudden increase of the ion source, while the accelerator works in nominal conditions (Table 2.2). The accelerator control system reacts immediately increasing the feeding power, in order to keep the proton beam energy constant at its nominal value. Accordingly, the beam current increases, inducing a jump in the number of spallation reactions taking place inside the target and, eventually, an equivalent rise of reactor core power[44].

The maximum accelerator operating power is limited to 170% of the nominal value by the fault tolerance scheme implemented inside its high energy section. This means that an increase of the ion source by more than 70% (and similarly any other disturbance causing the power to exceed such threshold) would result in the immediate intervention of its protection system, shutting off the accelerator itself. On the other hand, power fluctuations lower than 70% are allowed. In such cases, however, a high neutron flux signal prolonging for more than 3 s triggers the accelerator shut-off[45].

Assessing MYRRHA fuel performance under a beam power jump accidental scenario, thus, the worst possible situation is the occurrence of an ion source jump by 70%, causing in turn an increment of the neutron flux (and so of the linear power) by an equivalent amount. To perform the most conservative evaluation, then, such conditions are attributed to the hottest pin identified in Chapter 4.

5.1.1 BPJ simulation in TRANSURANUS

The 70% beam power jump transient is supposed to happen after normal (base) irradiation conditions, at the end of different batches (see Section 5.1.3 for more details).

Specifically, three steps have been set to simulate the BPJ progression:

1. A time interval equal to 1 ms required to reach the new asymptotic neutron flux and linear power values, right after the accelerator beam trip (neglecting the effect of delayed neutrons);
2. 3 s of constant overpower conditions, with both the linear power and the neutron flux at 170% of their nominal values, without changing their axial shape;

[44] Remember from the point kinetics equations for a generic subcritical core, i.e., a system requiring an external neutron source to achieve a stable neutronic population (exploiting for example spallation reactions, as for an ADS like MYRRHA), that the steady state power level is directly proportional to the intensity of the external source itself.

[45] Accelerator availability is a crucial issue for the operation of an ADS. To achieve its target value, a long mean time between failures is necessary, and it can be accomplished only by means of an effective fault tolerance implementation. In the case of MYRRHA, it corresponds to failure a beam current trip prolonging for more than 3 s (and a limited number of them must happen during the whole fuel life), triggering reactor shutdown [22]. Otherwise, the facility continues to operate allowing the accelerator to recover the beam without impacting on its availability.

3. Reactor scram (meaning shutdown due to accelerator turn-off, being the core configuration subcritical), after the detection of the abnormal power fluctuation by the control system[46].

A qualitative sketch of the BPJ evolution is reported in Figure 5.1, allowing a better understanding of its temporal development.

The analysis of each of the investigated transients is presented in dedicated following sections.

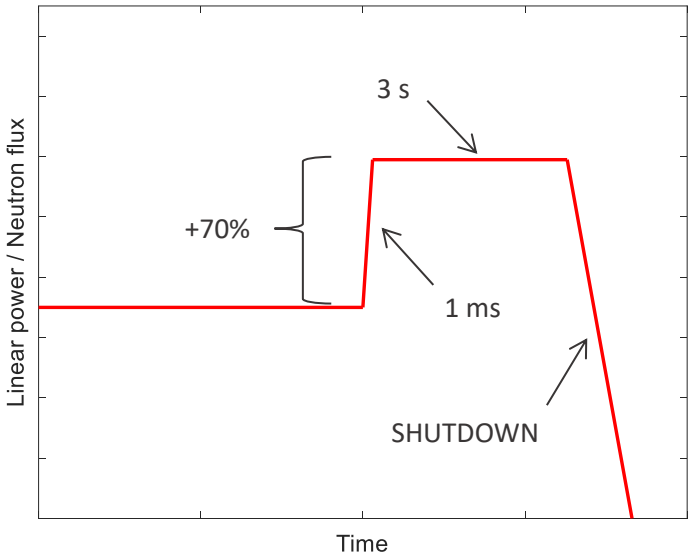

Figure 5.1: Qualitative representation of the BPJ transient scenario considered as design basis accident for the MYRRHA reactor.

5.1.2 Design limits for accidental conditions

In Chapter 4, indicative design limits addressed to ALFRED reactor and to LMFBRs in general have been taken as reference to assess the MYRRHA hottest pin performance under normal operating conditions. Accordingly, some thresholds were imposed on maximum values reached in any instant of time during the irradiation history (fuel and cladding peak temperatures, cladding instantaneous deformation), and on cumulative quantities resulting from the whole pin irradiation history (cladding irreversible strain components).

An accidental scenario as a beam power jump, consisting in a short time interval in which power and neutron flux show an exceptional increment, should have an impact on the instantaneous figures of merit and not on the cumulative ones. It is expected, hence, the maximum fuel temperature to grow very rapidly owing to the linear power jump, and similarly the cladding plastic deformation in case the gap closes and a sufficiently strong contact pressure develops (due to the differential thermal expansion pellet-cladding). On the other hand, cladding creep and swelling strains should not vary substantially, being the time in which the overpower conditions persist too short to cause their steep modification (although the two mechanisms are certainly speeded up).

[46] Note that the time assumed for reactor shutdown to take place does not affect the analysis outcome, at least from the fuel performance point of view.

In light of these considerations, it is deemed plausible to have failure occurring either by phenomena arising with fuel melting, or by cladding thermo-mechanical collapse [13]. Therefore, to assess the BPJ accidental transient, only a conservative margin from fuel melting and a maximum cladding plastic strain are set as design limits, as indicated in Table 5.1.

Table 5.1: Design limits for MYRRHA beam power jump accidental conditions [13].

Quantity	Design limit
Peak fuel temperature during BPJ	2870 K
Cladding plastic strain	0.5%

5.1.3 Investigated transients

The beam power jump transient can occur at any instant of time during the irradiation history, in principle. It has been decided, accordingly, to study its implications in three different moments along the fuel pin in-reactor life: BoL, mid-life and EoL conditions. The correspondent investigated scenarios are the following:

- BPJ at the end of batch 1 (BoL);
- BPJ at the end of batch 2 (BoL);
- BPJ at the end of batch 5 (mid-life);
- BPJ at the end of batch 12 (EoL).

The results for each of them are presented in four dedicated sections below. Following the same approach of Chapter 4, they have been simulated employing both the reference set of correlations and the set leading to the worst case, identified through a sensitivity analysis on models[47]. Maximum peak fuel temperature (during the BPJ) and cladding plastic strain have been considered as figures of merit to drive the worst case research, being the two quantities subjected by design limits in BPJ accidental conditions. The same phenomena/properties and associated model options considered in Section 4.4.2 have been included in the analysis, being the most influent on fuel temperature and gap dynamics (which reflects on cladding plastic strain).

The temporal position of the four BPJ transients has been selected based on the outcomes of normal operation analysis presented in Chapter 4.

As far as the margin from fuel melting is concerned, the end of batch 1 and batch 2 are the time instants at which maximum fuel temperatures take place. Hence, a BPJ transient at the end of batches 1 or 2 is expected to be the most critical with respect to the design limit on peak fuel temperature[48]. On the other hand, batch 5 and batch 12 display linear heat rates and fuel

[47] The worst case changes depending on the selected figures of merit and considered phenomena/properties, but also with the irradiation history itself. The worst correlation sets found in Section 4.5 for base irradiation conditions, thus, are not the same holding for the four beam power jump transients: a new multivariate procedure is required for each of the accidental situations, looking for the respective worst outcomes.

[48] Actually, the maximum peak fuel temperature verifies at the end of batch 2 in base irradiation conditions (owing to the gap conductance drop). The highest linear power, however, exists during batch 1, and its increment by 70% could make it win over the gap dynamics effects. For such reason, both the batches are accounted for.

temperatures which are too low to cause concerns about fuel melting in the occurrence of such overpower transient.
As regards the plastic strain limit, conversely, for batch 1 and batch 2 the stronger thermal expansion (consequence of the power jump) is believed as insufficient to bring the still wide gap to closure and to produce a significant contact pressure. Instead, at the end of batch 12 the gap width has reached its minimum in reference case, so that a further power boost could lead to its closure, giving rise to FCMI and possibly to cladding yielding; even more severe is the worst case in normal operating conditions, in which FCMI begins already at batch 10 (so any additional strain increment raises the contact pressure).
In what follows, for each of the analysed transients, the focus is on such quantities which more characterize the accidental scenario itself (and related phenomena). Correspondingly, only the results showing the evolution of fuel temperature are displayed dealing with the BPJ scenarios occurring after batches 1 and 2, while the cladding plastic strain and the associated worst case are investigated in details concerning the BPJ at the end of batch 12 (irrespective of the worst conditions in terms of temperature).

5.2 BPJ at batch 1

In Chapter 4, fuel and cladding temperature trends have been investigated for slice 9, which proved to be the hottest fuel axial slice. The occurrence of a beam power jump entails a sudden increment of linear power and neutron flux for the whole fuel pin, thus preserving their axial profiles. Accordingly, the hottest conditions still persist in correspondence of the same spot (i.e., slice 9), both at the end of batch 1 and at the end of batch 2 (see Figure 4.8): the margin from fuel melting is studied again for slice 9.
Figure 5.2 represents a scale model for the evolution in time of the linear heat rate, considering a beam power jump happening at the end of batch 1: the 70% overpower condition brings the power level to approach 400 W/cm, close to typical FR specifications.
Main consequence of the BPJ is a step of the peak fuel temperature by more than 400 °C following the linear power, as shown in Figure 5.3.

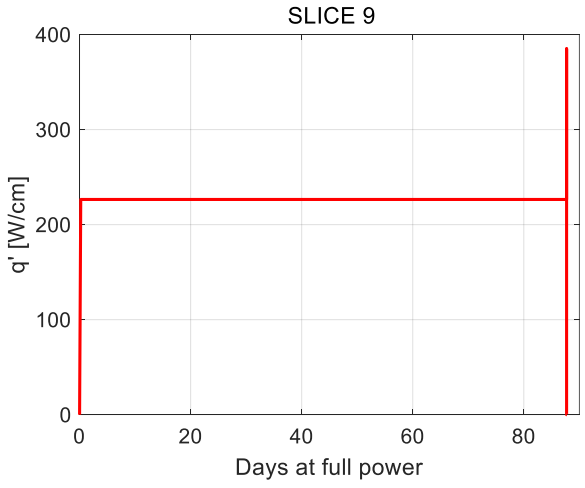

Figure 5.2: Linear power evolution in time at slice 9 -BPJ at batch 1.

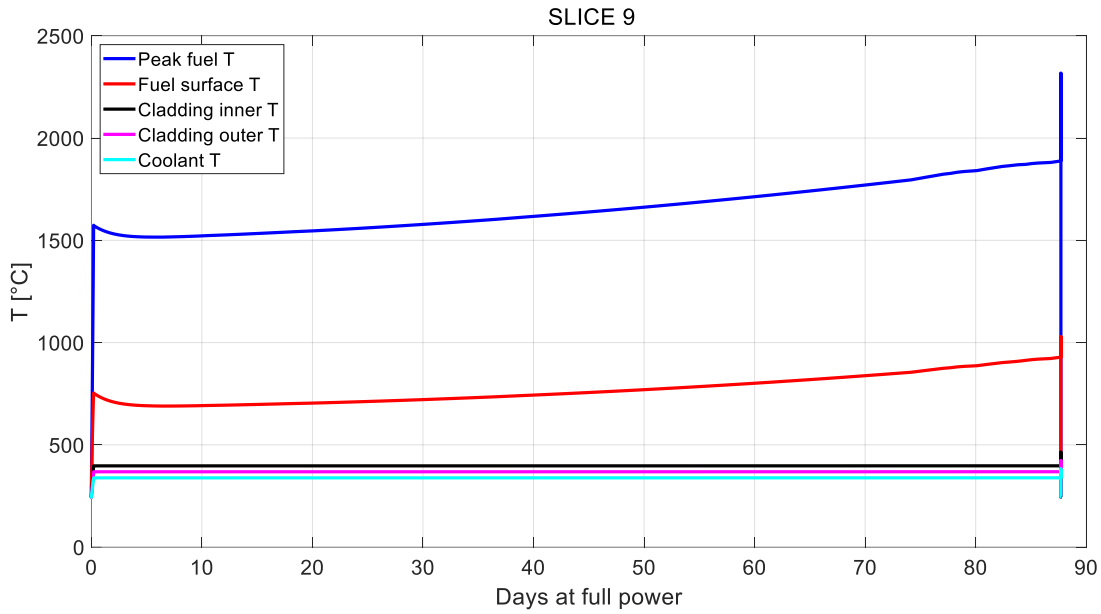

Figure 5.3: Evolution in time of fuel, cladding and coolant temperatures at slice 9 - BPJ at batch 1.

The differential thermal expansion between fuel and cladding in response to the temperature rise, involves the reduction of the gap width by roughly 15 μm, as displayed in Figure 5.4: the remaining width is still considerable (more than 30 μm), confirming the expectations[49]. The cladding plastic strain remains null in correspondence of slice 9 as well as in all the fuel pin axial length, accordingly. The average equivalent plastic strain at shutdown is reported in Figure 5.5 together with the permanent tangential strain, which is not influenced by the beam power jump.

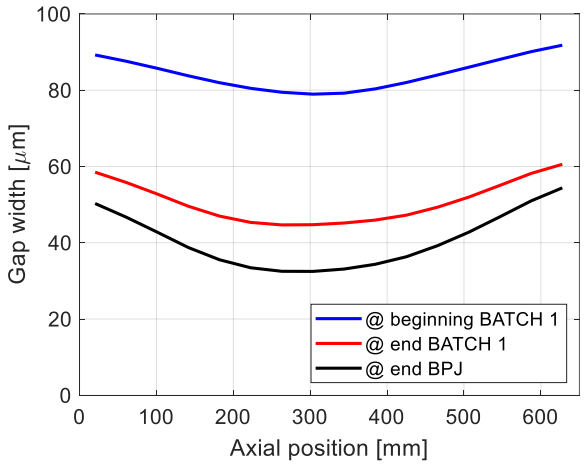

Figure 5.4: Axial gap width at different irradiation times - BPJ at batch 1.

[49] As said in Section 5.1.2, only the differential thermal expansion contributes to gap dynamics during the 3 s of the BPJ, given that creep and swelling mechanisms are accelerated by the overpower conditions, but the time in which these conditions persist is too limited to enlarge their contribution to cladding deformation.

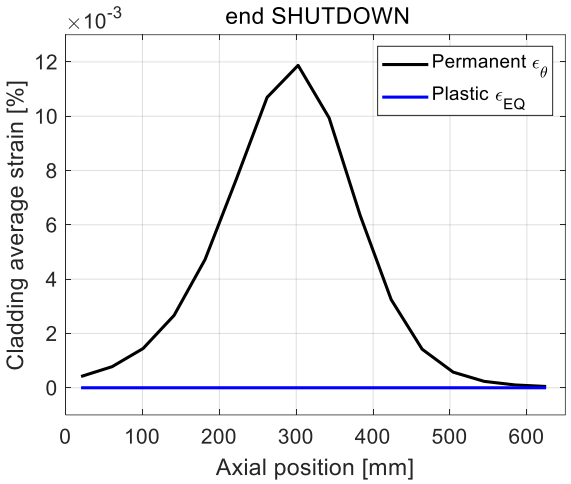

Figure 5.5: Cladding axial strains at shutdown - BPJ at batch 1.

5.2.1 Worst case

The worst case in terms of fuel temperature only has been searched for in case of a BPJ transient occurring at the end of batch 1. It has been shown, indeed, that the pellet-cladding contact is far from verifying in the reference case, so reaching a contact pressure causing yielding is deemed definitely impossible, even considering the worst possible combination of input models.

The outcome of the multivariate analysis unveils the existence of four different correlation sets leading to the highest peak fuel temperature, as reported in Table 5.2. The reason of multiple scenarios is ascribed to the irrelevancy both of the thermal creep model choice and of the fuel swelling one. Concerning the swelling modelling, the burnup reached after batch 1 is lower than 1 at.%, so that the *BE-MOX according to Preusser* and the *MOX according to Freund et al.* models coincide (see Figure 4.19). All the four correlation sets, instead, share the same options regarding void swelling, irradiation creep (with the *Többe correlation* in place of the *Grossbeck data fitting* that held in base irradiation conditions) and fuel thermal conductivity.

Figure 5.6 shows the comparison between the temperature evolutions for the reference and for the worst case, with a maximum discrepancy between the fuel curves of more than 100 °C after few days at full power, which gradually reduces towards the end of the batch. Considering the early occurrence of the BPJ, the fuel thermal conductivity dominates in determining the peak fuel temperature. Thus, the worst case includes the *MOX according to Carbajo et al.* model, supplying the lowest thermal conductivity values (see Figure 4.20).

Table 5.2: Models leading to the worst cases (WC) in terms of fuel temperature - BPJ at batch 1.

Phenomenon/Property	WC - Fuel temperature
Cladding thermal creep	Not relevant
Cladding irradiation creep	*Többe correlation*
Cladding swelling	*Lemehov "B version"*
Fuel thermal conductivity	*MOX according to Carbajo et al.*
Fuel swelling	Not relevant

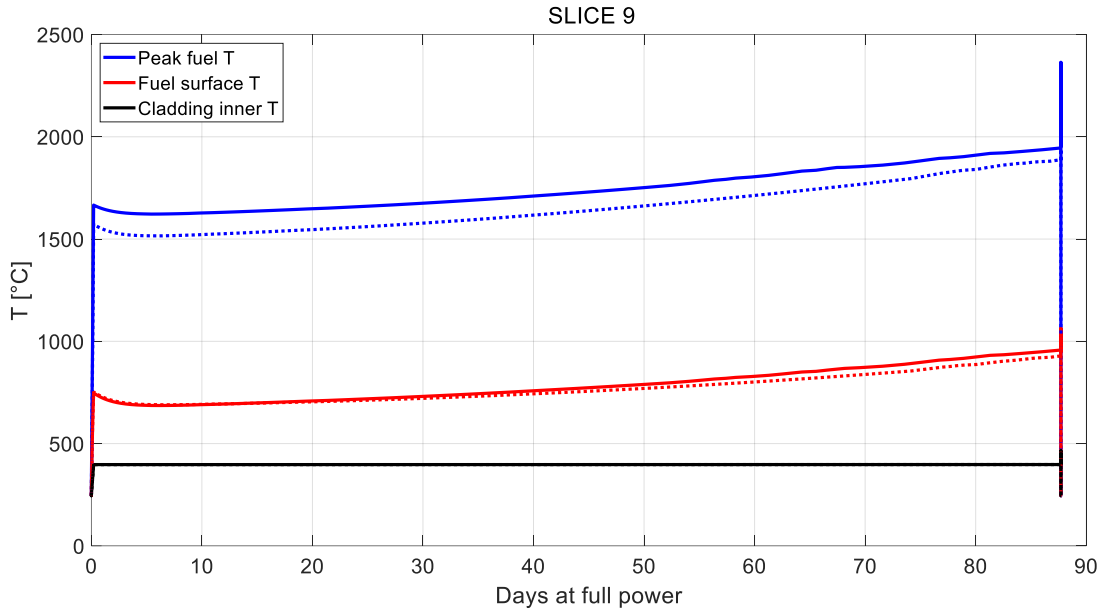

Figure 5.6: Evolution in time of fuel and cladding temperatures at slice 9 in RC (dotted line) and in WC (solid line) - BPJ at batch 1.

5.2.2 Assessment of design limits

The maximum values of peak fuel temperature and cladding plastic strain are summarized in Table 5.3 both for the reference and for the worst case. Whereas the plastic strain remains equal to zero, a 46 °C difference in the maximum peak fuel temperature takes place among the two scenarios. The design limit on the peak fuel temperature defined in Table 5.1, however, is respected even in the worst case and it is possible to rely upon a big safety margin for both the two situations.

Table 5.3: Assessment of design limits in RC and in WC – BPJ at batch 1.

Quantity	Maximum value	
	RC	WC
Peak fuel temperature during BPJ	2307 °C	2353 °C
Cladding plastic strain	0.00%	0.00%

5.3 BPJ at batch 2

In base irradiation conditions, the maximum fuel temperature is reached at the end of batch 2 and in correspondence of slice 9 (Figure 4.8). Following the same approach as for a beam power jump occurring at the end of batch 1, it is expected to find the hottest spot again at slice 9.

Figure 5.7 shows the real temporal evolution of the linear heat rate for slice 9. Owing to more relaxed power conditions featuring batch 2 with respect to batch 1, the linear power during the BPJ moves close to 350 W/cm, lower than the 400 W/cm reached with a BPJ after batch 1. As

proven analysing MYRRHA normal operating conditions, however, the evolution of gap conductance plays a crucial role in determining the peak fuel temperature. It could happen, therefore, that the minimum possible margin to melting during BPJ accidents takes place if one of such transients occurs after batch 2, although the linear power is not the highest possible one (i.e., is lower than that reached in case of a BPJ after batch 1).
The resulting temperature evolutions for the hottest slice are reported in Figure 5.8. A peak fuel temperature step of roughly 350 °C is obtained, leading to a maximum value close to the one achieved during the BPJ at the end of batch 1.

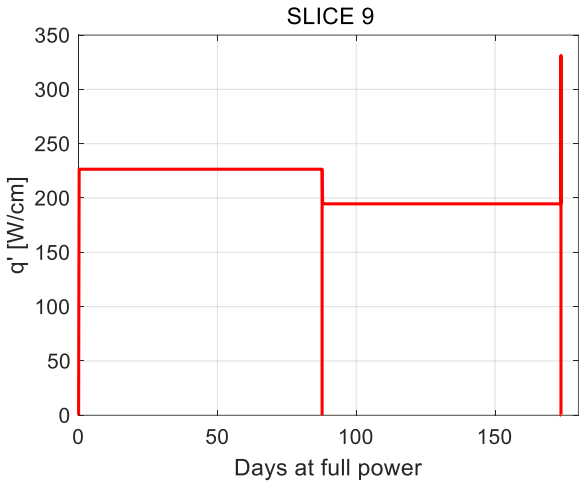

Figure 5.7: Linear power evolution in time at slice 9 -BPJ at batch 2.

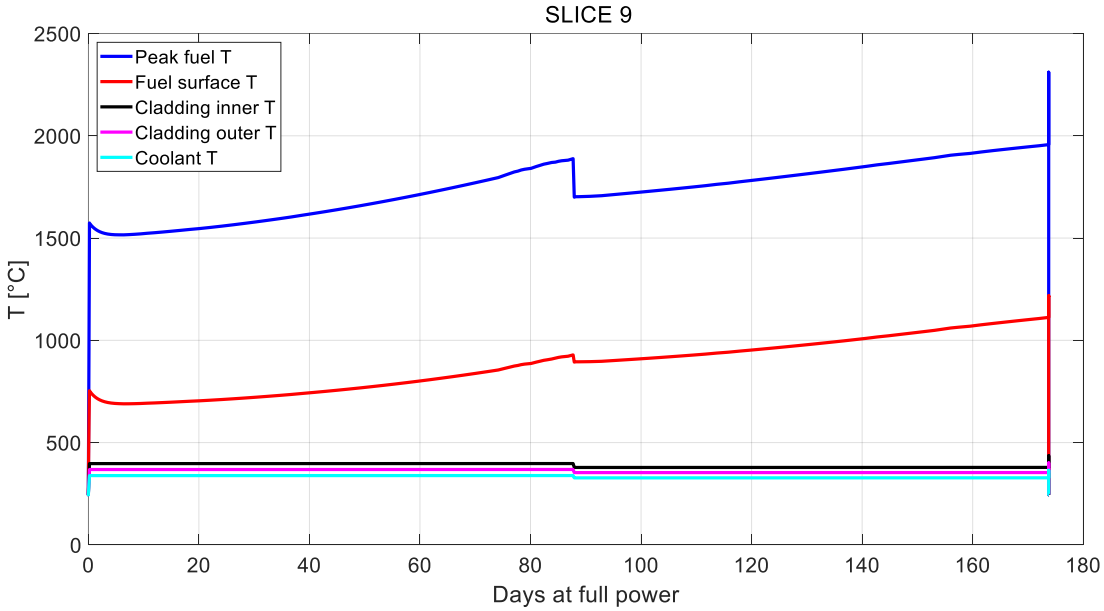

Figure 5.8: Evolution in time of fuel, cladding and coolant temperatures at slice 9 - BPJ at batch 2.

An outcome similar to the previous scenario holds for gap width: it is possible to appreciate from Figure 5.9 the gap reduction originating from the temperature increment consequent to the BPJ. Again, a considerable margin from gap closure still exists, making the cladding plastic deformation equal to zero allover the fuel pin length.

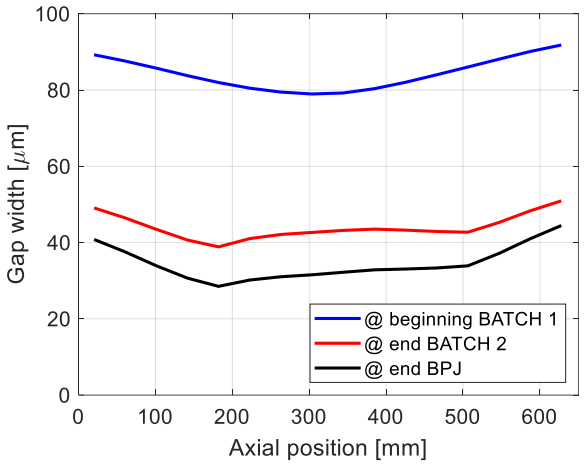

Figure 5.9: Axial gap width at different irradiation times - BPJ at batch 2.

5.3.1 Worst case

Similarly to the batch 1 investigation, only the peak fuel temperature has been considered as figure of merit for the sensitivity analysis, based on the reference case outcomes.

Two scenarios have been discovered from the multivariate procedure. Table 5.4 reports the model options employed by those two worst cases: the only difference with respect to the previous transient lies in the fuel swelling correlation. Having exceeded the limit fuel burnup of 1 at.%, indeed, the fuel pellet swelling behaviour predicted by the *BE-MOX according to Preusser* or by the *MOX according to Freund et al.* models is different. The first one features both the worst cases, given that it entails a lower gap size reduction, resulting in a higher thermal resistance.

The comparison between reference and worst case in terms of temperature is disclosed in Figure 5.10: a maximum gap of more than 100 °C after few days at full power appears, with a slight restriction as the irradiation history proceeds. Again, the major contributor to the discrepancy holds in the fuel thermal conductivity model.

Table 5.4: Models leading to the worst cases (WC) in terms of fuel temperature - BPJ at batch 2.

Phenomenon/Property	WC - Fuel temperature
Cladding thermal creep	Not relevant
Cladding irradiation creep	*Többe correlation*
Cladding swelling	*Lemehov "B version"*
Fuel thermal conductivity	*MOX according to Carbajo et al.*
Fuel swelling	*BE-MOX according to Preusser*

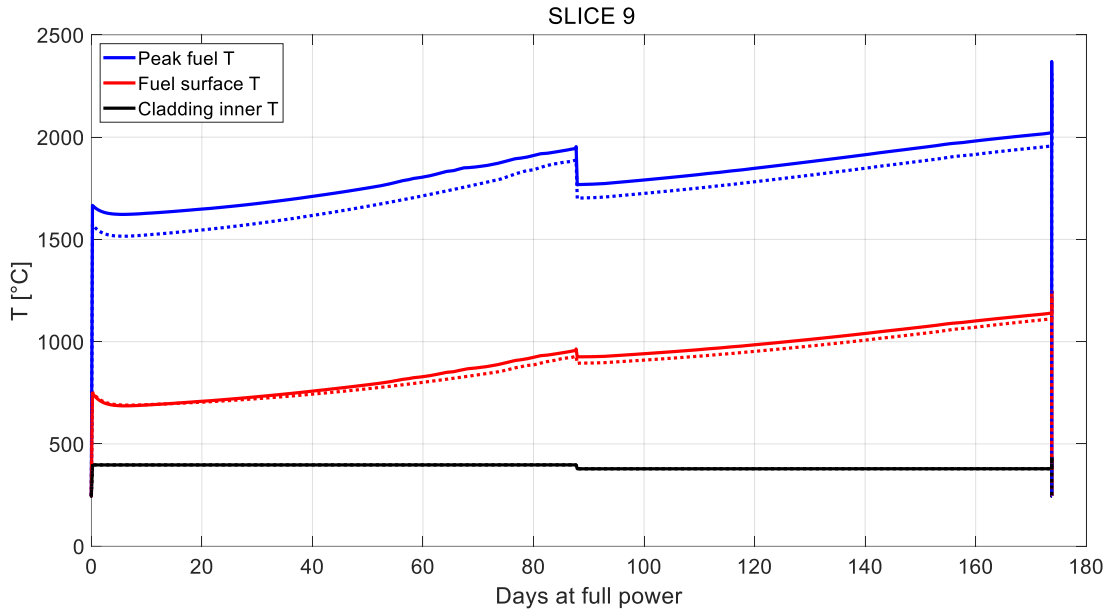

Figure 5.10: Evolution in time of fuel and cladding temperatures at slice 9 in RC (dotted line) and in WC (solid line) - BPJ at batch 2.

5.3.2 Assessment of design limits

Table 5.5 reports the maximum values calculated by TRANSURANUS for the two quantities subjected to design limits for accidental conditions.

As for the margin from fuel melting, a considerable gap exists for the investigated transient as well as for the previous one. It is interesting to note, however, that with the reference set of correlations it is a BPJ occurring at the end of batch 1 which provides the highest fuel temperature, meaning that the linear power effect wins over gap dynamics. The situation overturns accounting for the worst case. Such behaviour underlines again the importance to include model uncertainties inside the fuel performance analysis for a conservative assessment.

Finally, as in the BPJ transient after batch 1, the cladding plastic strain remains always equal to zero.

Table 5.5: Assessment of design limits in RC and in WC – BPJ at batch 2.

Quantity	Maximum value	
	RC	WC
Peak fuel temperature during BPJ	2303 °C	2359 °C
Cladding plastic strain	0.00%	0.00%

5.4 BPJ at batch 5

The effects of a BPJ at the end of batch 5 on MYRRHA fuel performance are here discussed as representative for the pin behaviour in case of a mid-life transient. Differently from the previous two occurrences, at batch 5 the linear heat rate has decreased to values sensibly smaller than 200 W/cm, while the ongoing fuel swelling has caused the gap to further reduce in width, potentially leading to closure.

Figure 5.11 represents the linear power scale evolution for the hottest slice, if the BPJ occurs after batch 5. To identify the hottest slice, the axial peak fuel temperature profile has been studied at the end of batch 2 and after the BPJ, discovering that higher temperatures are reached exactly during the accidental conditions, and again at slice 9. In Figure 5.12, the temperature trends are disclosed for such slice, showing a fuel maximum near 2000 °C immediately before shutdown, owing to a linear power achieving 250 W/cm (a value higher than the one featuring batch 1).

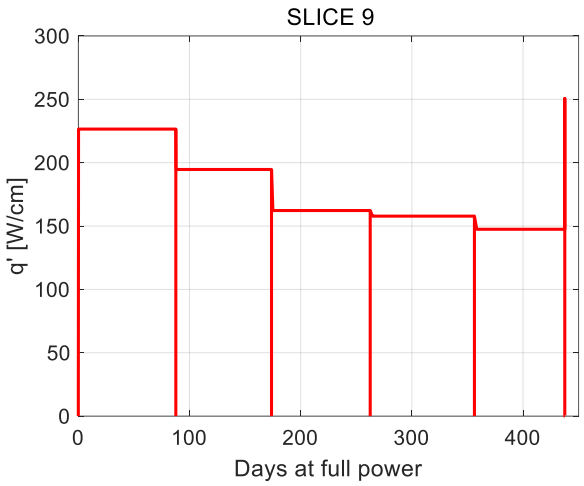

Figure 5.11: Linear power evolution in time at slice 9 -BPJ at batch 5.

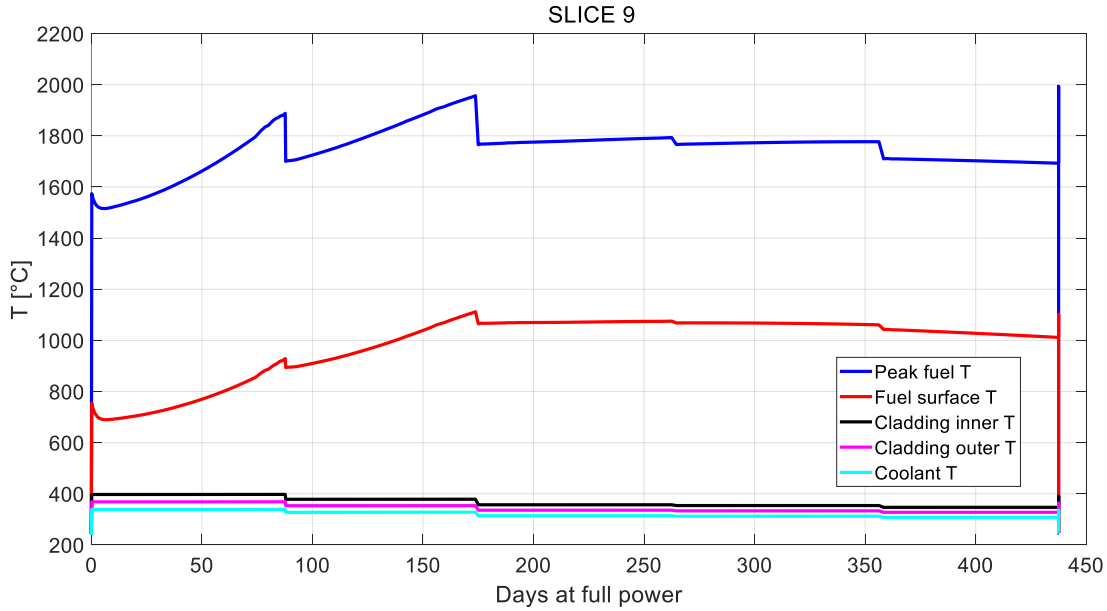

Figure 5.12: Evolution in time of fuel, cladding and coolant temperatures at slice 9 - BPJ at batch 5.

As far as the plastic strain is concerned, the gap axial profile is shown in Figure 5.13. Comparing these curves with Figure 5.9, a width reduction by roughly 10 μm can be inferred right before the BPJ. A further restriction takes place with the temperature increase, consequence of the overpower conditions, however the minimum thickness approaches 20 μm. Accordingly, no FCMI occurs and no cladding plastic deformation is possible.

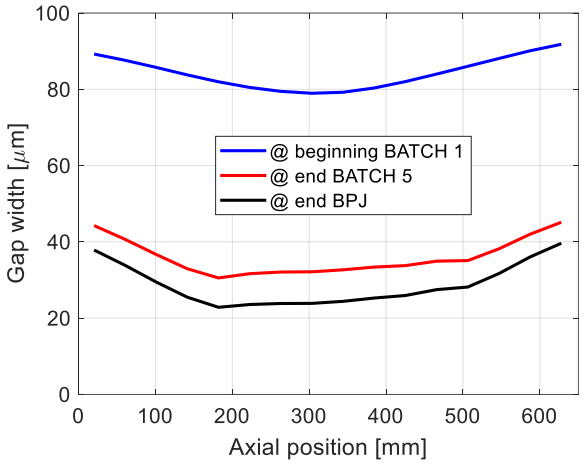

Figure 5.13: Axial gap width at different irradiation times - BPJ at batch 5.

5.4.1 Worst case

From the multivariate analysis, one single worst case has been obtained, featured by the highest fuel temperature and by zero plastic strain (as all the other scenarios).

Table 5.6 reports the model options characterizing the worst input combination. Differently from base irradiation conditions and from the BPJ transients analysed before, the thermal creep correlation employed in the simulation plays a difference in the fuel performance, although minimal (adopting the *Modified Delville correlation* in place of the *Többe* one implies a reduction by 0.02 °C in the maximum peak fuel temperature, which is too small and not significant in a fuel performance simulation). This means that the overpower conditions, during the 3 s in which they persist, accelerate the thermal creep mechanism enough to induce an effect on cladding deformation, reflecting on fuel temperatures.

The plots showing the comparison between reference and worst case results for the BPJ under consideration are not here disclosed, being exempt from significant criticalities both in terms of fuel temperature and of cladding plastic strain.

Table 5.6: Models leading to the worst case (WC) in terms of fuel temperature - BPJ at batch 5.

Phenomenon/Property	WC - Fuel temperature
Cladding thermal creep	*Többe correlation*
Cladding irradiation creep	*Grossbeck data fitting*
Cladding swelling	*Lemehov "B version"*
Fuel thermal conductivity	*MOX according to Carbajo et al.*
Fuel swelling	*BE-MOX according to Preusser*

5.4.2 Assessment of design limits

Maximum peak fuel temperature and cladding plastic strain are summarized in Table 5.7 for the sake of the design assessment in reference and in worst case. No differences exist between the two scenarios in terms of plastic deformation, being FCMI not reached in both. On the other hand, a discrepancy of more than 80 °C unveils for the maximum fuel temperature, although the margin from melting remains largely safe (more than 500 °C).

The outcome is ascribed to the moment during the irradiation history in which the BPJ occurs: despite five batches are a too long time from the fuel melting issue point of view (the linear heat rate has lowered consistently in the meanwhile), they are not enough to provoke FCMI even with a sudden boost of the fuel thermal expansion.

Table 5.7: Assessment of design limits in RC and in WC – BPJ at batch 5.

Quantity	Maximum value	
	RC	WC
Peak fuel temperature during BPJ	1985 °C	2066 °C
Cladding plastic strain	0.00%	0.00%

5.5 BPJ at batch 12

The last investigated transient is a BPJ occurring at the end of the whole irradiation history, useful to study the accidental fuel pin response at the EoL.

In such conditions, the combined effect of gap conductance increase (see Figure 4.11) and linear heat rate reduction, bring the fuel in a rather cold condition, if compared to the first batches. The maximum peak fuel temperature, indeed, takes place still at the end of batch 2 and in correspondence of slice 9 (coinciding with the maximum identified in base irradiation conditions), whereas the peak value reached during the BPJ locates 500 °C below, in correspondence of slice 10. Accordingly, the temperature trends for slice 10 are reported in Figure 5.15, whereas the linear power temporal evolution is shown in Figure 5.14 for the hottest slice.

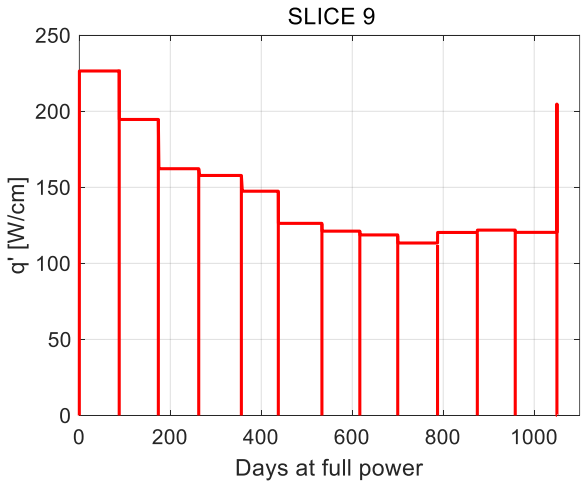

Figure 5.14: Linear power evolution in time at slice 9 - BPJ at batch 12.

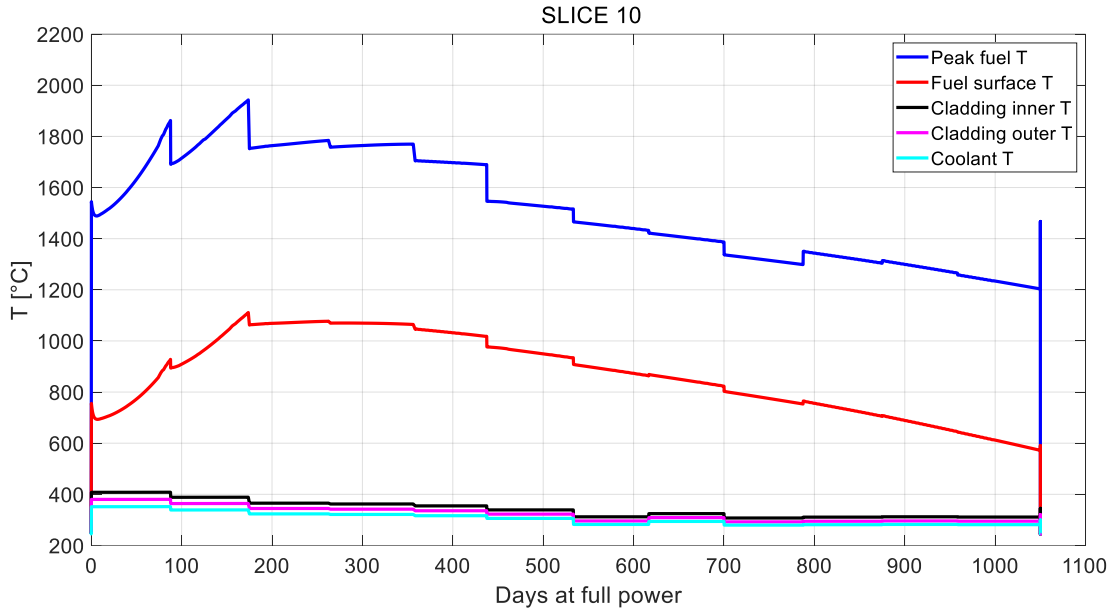

Figure 5.15: Evolution in time of fuel, cladding and coolant temperatures at slice 10 - BPJ at batch 12.

When dealing with a BPJ occurring at the end of the fuel pin life, it is more interesting to investigate the transient effects linked to the pellet-cladding contact issue. From the analysis of base irradiation conditions, the fuel gap at the end of batch 12 has a residual width of just 10 μm in reference case, so a further fuel thermal expansion could potentially close the gap, giving rise to a contact pressure between fuel and cladding.

Again, this does not occur: as from Figure 5.16 (left), the correspondent partial gap restriction consists of just 5 μm, leaving an equal minimum residual gap before FCMI occurs (at slice 8). Correspondingly, the plastic strain component remains null throughout the whole axial pin length (Figure 5.16, right).

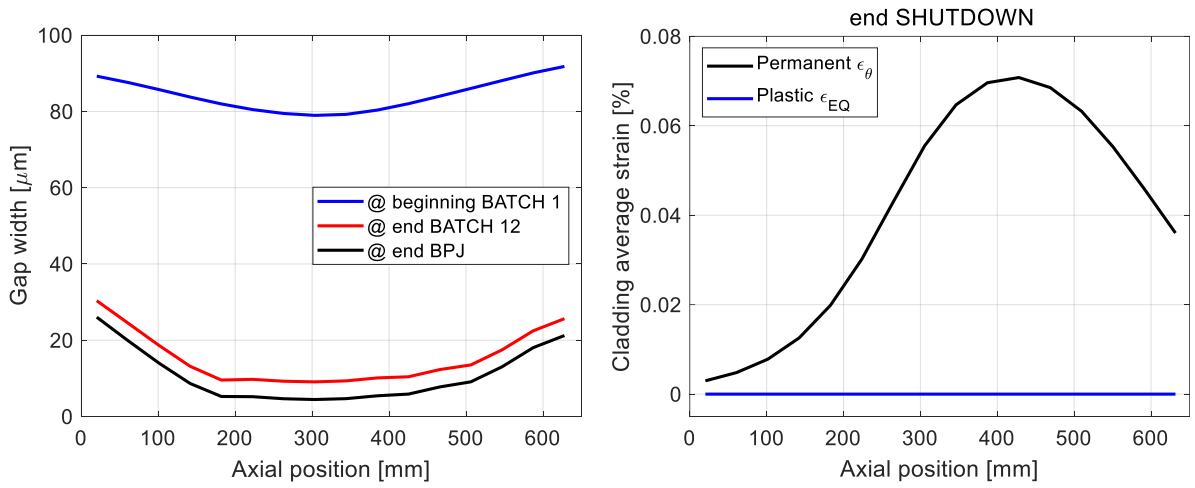

Figure 5.16: Axial gap width at different irradiation times and cladding axial strains at shutdown - BPJ at batch 12.

5.5.1 Worst case

In light of the results obtained in reference case, a worst scenario in terms of maximum fuel temperature has not been investigated[50]. Rather, the model combination leading to the highest plastic deformation has been searched for. All the 48 possible scenarios of the sensitivity analysis, however, are featured by a cladding plastic strain component equal to zero: another figure of merit has been set to extract an equivalent worst case.

Table 5.8: Models leading to the worst case (WC) in terms of contact pressure - BPJ at batch 12.

Phenomenon/Property	WC – Contact pressure
Cladding thermal creep	*Többe correlation*
Cladding irradiation creep	*Többe correlation*
Cladding swelling	*Lemehov "L version"*
Fuel thermal conductivity	*CONSERVATIVE-MOX according to Van Uffelen and Schubert.*
Fuel swelling	*MOX according to Freund et al*

The maximum contact pressure has been considered, given that the scenario characterized by its highest value (and so by the highest cladding stress), is the one which most approaches yielding[51]. The combination of models leading to the worst contact pressure case is reported in Table 5.8. Simulating the MYRRHA hottest pin exploiting such set of correlations, means predicting the major gap closure: the two *Többe correlations* are the ones supplying the lowest creep strain rates among the available options, similarly to the *Lemehov "L version"* for void swelling; conversely, the correlation predicting the highest possible fuel swelling appears. The fuel thermal conductivity option is the most difficult to explain, as the *MOX according to Freund et al* model places in between the other two alternatives.

Figure 5.17 (left) shows the axial gap width profile: an almost complete closure already features the fuel pin when the BPJ happens, causing its further contraction to the extent that just the extremity slices preserve a tiny opening (less than 1 μm thick). The strongest closure takes place in correspondence of the hottest slice (slice 9), as inferred from the right figure, showing the axial profile of the cladding average equivalent stress before the BPJ and right after.

The evolution with time of the gap width for slice 9 (suffering the highest cladding stress) is reported in Figure 5.18, highlighting that the main responsible for its closure (occurring towards the end of batch 9) is the fuel, swelling towards the cladding[52]. Moreover, whereas in reference case the gap width in correspondence of the BPJ suddenly restricts and reopens again after

[50] The outcome would not change: the temperature at the end of batch 2 would be always higher than the one reached during the BPJ, by far lower than the fuel melting temperature.

[51] Moreover, it has been guaranteed in base irradiation conditions that gap closure actually verifies for certain model combinations in input (see Table 4.8).

[52] Conversely, the cladding inner radius slightly reduces following the linear power evolution (being the irreversible cladding strain components very weak), before coming in contact with the pellet, driving then its deformation.

shutdown, the same does not hold for the worst case: the contact between fuel and cladding is kept also when the reactor is shut-off, as displayed in Figure 5.17 (left) as well.

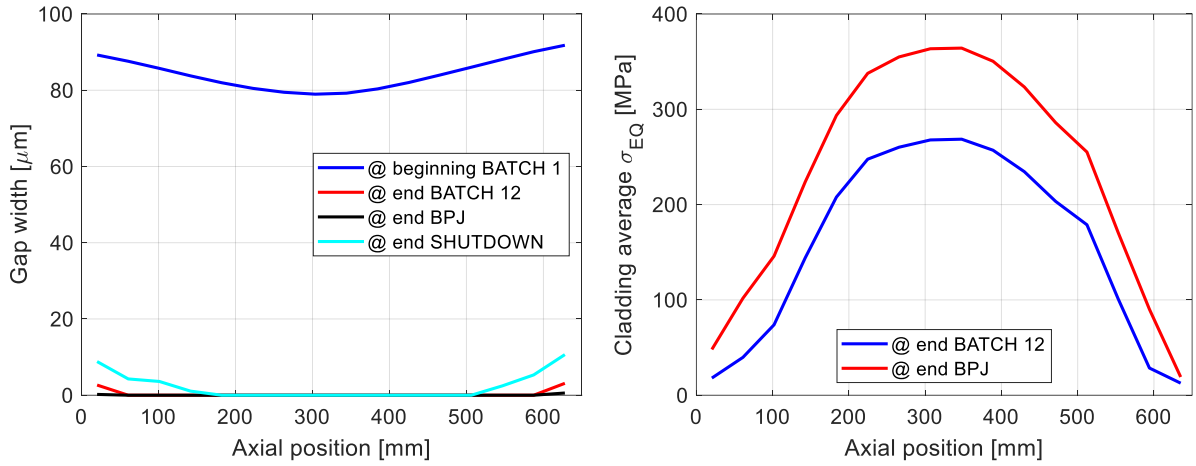

Figure 5.17: Axial gap width and cladding average equivalent stress at different irradiation times in WC - BPJ at batch 12.

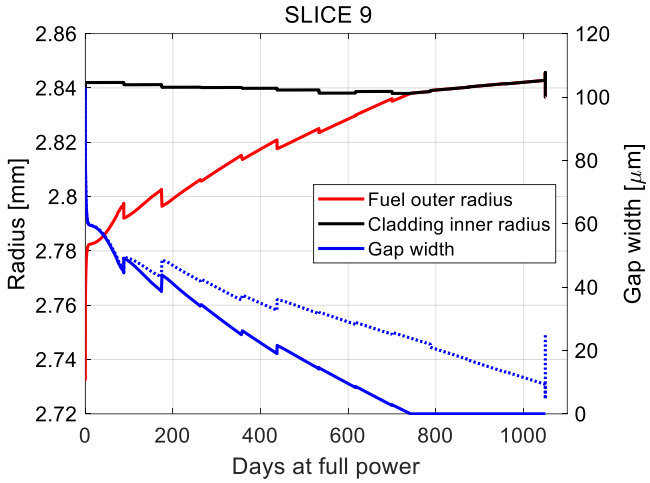

Figure 5.18: Gap evolution in time at slice 9 in RC (dotted line) and WC (solid line) - BPJ at batch 12.

The contact pressure between fuel and cladding is shown in Figure 5.19 together with the associated cladding average equivalent stress. The contact pressure begins to build-up after FCMI starts (the steps in the profile are caused by batch transfer), reaching roughly 45 MPa at the end of batch 12. Afterwards, a 15 MPa step develops during the BPJ, leading the contact pressure above 60 MPa. Following the contact pressure, cladding stress increases after gap closure as well, reaching more than 350 MPa during the BPJ and approaching the yielding point. Nevertheless, no plastic strain is present at the end of the irradiation history, as testifies Figure 5.20.

It is interesting to note that no stress relaxation verifies in this worst case, differently from what happens in base irradiation conditions (Figure 4.26). In that situation, the irradiation creep mechanism is very effective, owing to the *Grossbeck data fitting* formula featuring the worst case. Now, the creep phenomena are modelled with the two correlations predicting a slower mechanism: despite the significantly higher cladding stresses, stress relaxation cannot take place.

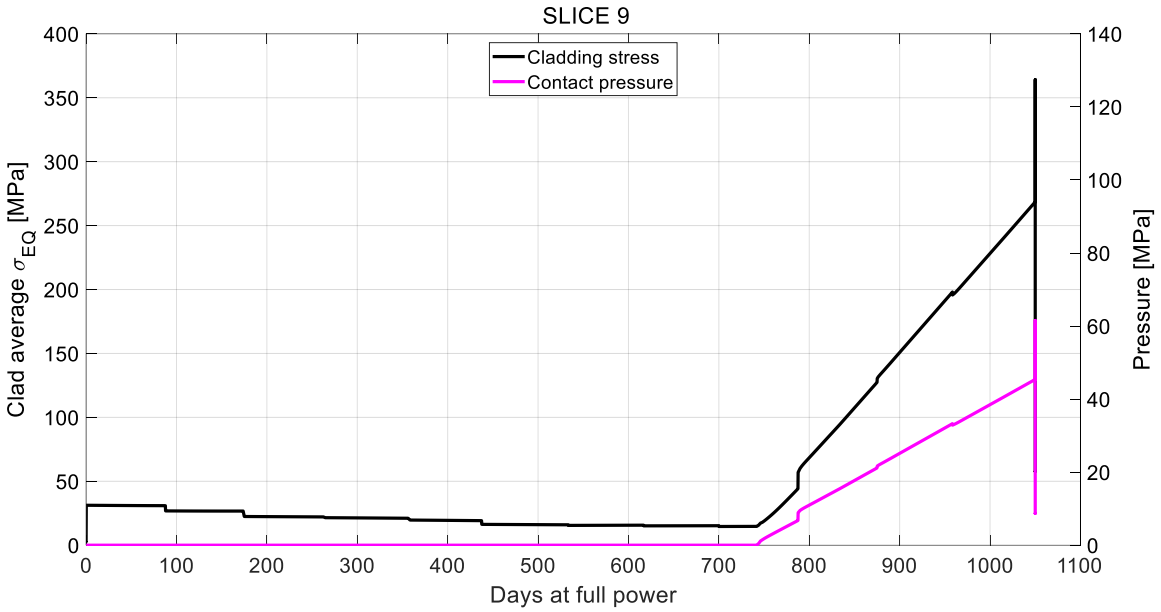

Figure 5.19: Evolution in time of cladding average equivalent stress and contact pressure at slice9 in WC – BPJ at batch 12.

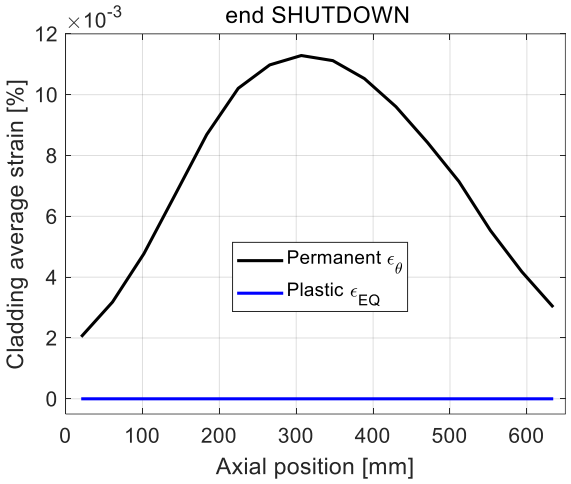

Figure 5.20: Cladding axial strains at shutdown in WC - BPJ at batch 12.

5.5.2 Assessment of design limits

In Table 5.9, the maximum values of peak fuel temperature and cladding plastic strain are reported for the two simulation cases.

As said, the BPJ transient under consideration is the one providing the greatest margin with respect to fuel melting, as the peak fuel temperature reached at the end of batch 2 stays well above that achieved during the transient.

The limit on cladding plastic strain, similarly, is respected in both the two scenarios. In this situation, however, the role of the sensitivity analysis is particularly crucial in the fuel performance: although yielding does not occur either in the reference or in the worst case, in the latter a cladding stress induced by fuel-cladding contact and exceeding 350 MPa takes place, whereas no FCMI at all happens in the former.

Table 5.9: Assessment of design limits in RC and in WC – BPJ at batch 12.

Quantity	Maximum value	
	RC	WC
Peak fuel temperature during BPJ	1463 °C	1386 °C
Cladding plastic strain	0.00%	0.00%

5.6 Power analysis

The outcome of MYRRHA hottest pin fuel performance simulations for the four beam power jump transients has unveiled that significant margins from the design limits set for accidental conditions exist, both considering fuel melting and cladding plastic strain.

A quantification of such margins, in terms of power, is the aim of this section, focused on the determination of the linear heat rate causing the fuel temperature or the cladding plastic strain to reach the imposed design limits. The usefulness of this analysis is twofold: on one side, it is necessary to assess the design in accidental situations; on the other side, a potential power increment in normal operating conditions is evaluated (taking care about the validity of the design limits also in such conditions).

The investigation is carried out considering those transients most approaching fuel melting or an excessive cladding plastic strain. Accordingly, the two beam power jumps occurring at BoL have been chosen to find the minimum margin to melting[53], whereas the one at the end of batch 12 for evaluating the minimum power increment needed to exceed the limit cladding plastic strain. Other transients could have been considered (e.g., the BPJ after batch 5); however, the critical power level achieved in such cases would be certainly higher. The worst case scenario for the selected transients is analysed, so that uncertainties are accounted for and a conservative assessment is carried out.

5.6.1 Power margin quantification in TRANSURANUS

To quantify the power margins, the MYRRHA hottest pin behaviour has been simulated increasing progressively the linear power produced by the fuel rod itself (and correspondingly the neutron flux), while monitoring the two figures of merit subjected to design limits. Being the irradiation history constituted by several batches, it has been chosen to increase the power level of the entire MYRRHA base irradiation history, instead of focusing only on the batch interested by the BPJ transient[54]. Such hypothesis is beneficial from two different points of view: firstly, the power margin thereby acquired is more prudent, since the fuel pin experiences harsher conditions along its whole in-reactor life; then, it supplies an immediately useful indication about the extent to which the reactor power could be incremented without exceeding the design limits for a BPJ accident.

[53] Both the BPJ after batch 1 and after batch 2 have been selected in view of the minimal discrepancy found between the two accidental situations.

[54] It has been assumed, furthermore, that the axial shape of the linear power itself remains unchanged (as well as the shape of the neutron flux).

The simulations have been carried out employing the worst sets of input models.
As discussed and proven in the previous sections, the worst combination changes according to the irradiation history, so it is not guaranteed that, modifying the linear power and the neutron flux, it remains the same as before. Considering the BPJ occurring after batch 1 and after batch 2, the maximum peak fuel temperature is mainly a consequence of fuel thermal conductivity and gap thermal resistance (the interaction between fuel pin mechanisms is minimal), so it is expected that increasing the power the outcome would not change markedly: the worst case is always featured by the correlations providing the lowest possible fuel thermal conductivity and the maximum possible gap opening (i.e., low fuel swelling and high cladding deformations).
A different argument holds for a BPJ taking place at the end of the irradiation history: the power increment affects the development of all mechanisms involved in the fuel performance and especially their interaction (e.g., stress relaxation when the gap closes), potentially changing the worst model combination previously identified.
In light of these explanations, the power increment has been applied to the worst case identified in Section 5.2.1 and Section 5.3.1 for the BPJ at the end of batch 1 and at the end of batch 2 respectively, whereas a complete sensitivity analysis has been performed at every power variation for the BPJ at batch 12, in order to find the worst scenario in terms of cladding plastic strain associated to each power step.

5.6.2 Power analysis results

Table 5.10 discloses the maximum power increment expressed as percentage of the nominal value (with a resolution of 1%), allowed before reaching the correspondent accidental design limit.
Note that the most restrictive transient is the BPJ occurring at the end of batch 1, which approaches the fuel melting limit rising the overall power history by 11%. A higher power increment, conversely, is required by a BPJ after batch 2, meaning that with a 11% increase the maximum peak fuel temperature reached during such transient is lower than that calculated in case of a BPJ occurring after batch 1, in contrast to what happens in nominal power.
A significant power increment (27%) is needed, instead, to approach the cladding plastic strain limit when a BPJ at the end of batch 12 verifies.

Table 5.10: Maximum power increments before exceeding the accidental design limits.

Accidental situation	Max. power increment	Limiting design limit
BPJ batch 1	+11%	Peak fuel temperature
BPJ batch 2	+14%	Peak fuel temperature
BPJ batch 12	+27%	Cladding plastic strain

BPJ at batch 1 and BPJ at batch 2

Figure 5.22 (left) and Figure 5.21 (left) show the evolution of the linear power in the limiting situation for a BPJ occurring after batch 1 and after batch 2 respectively, considering the worst case and the hottest slice. The two right figures display the peak fuel temperature trends, being the limiting factor for the power rise in such transients.

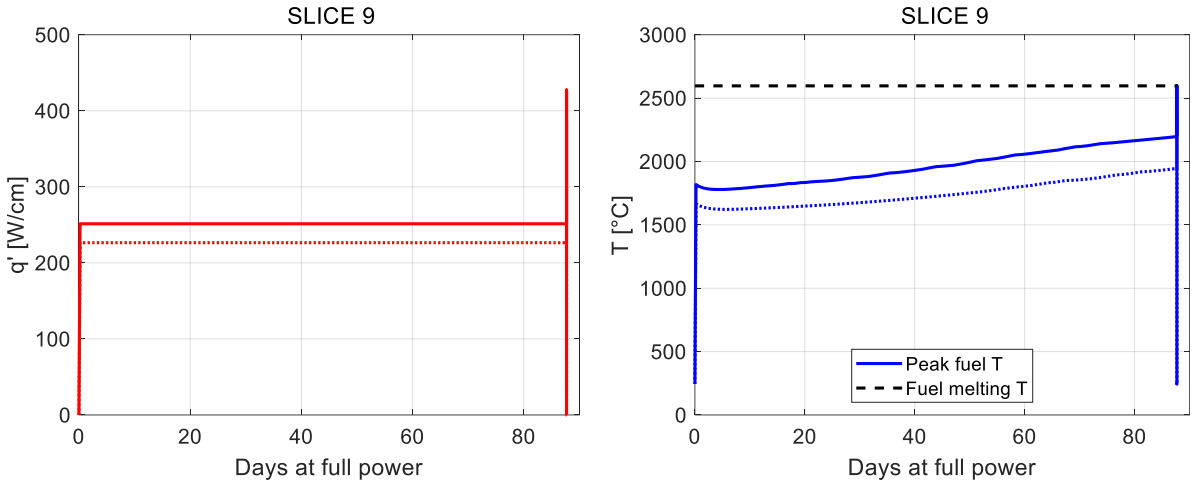

Figure 5.22: Evolution in time of linear power (left) and peak fuel temperature (right) at slice 9 in nominal (dotted line) and limit (solid line) power conditions, in WC – BPJ at batch 1.

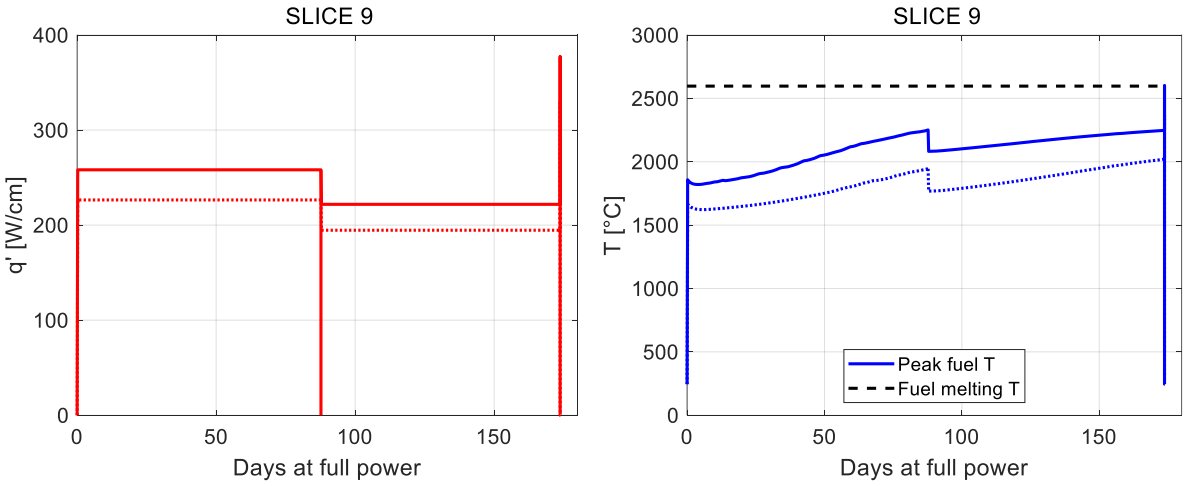

Figure 5.21: Evolution in time of linear power (left) and peak fuel temperature (right) at slice 9 in nominal (dotted line) and limit (solid line) power conditions, in WC – BPJ at batch 2.

BPJ at batch 12

Searching for the worst case for a BPJ after batch 12, the majority of the 48 scenarios composing the multivariate analysis are featured by a cladding plastic strain still equal to zero. The same model combination found for nominal power and described in Table 5.8, instead, has revealed to lead the highest cladding plastic strain, since it provides the fastest possible gap closure due to a strong fuel swelling and a slight cladding deformation.

Figure 5.23 shows the linear power evolution for the hottest slice considering the limiting power increment that still allows observing the design limits. The correspondent axial profile of cladding plastic strain is reported in Figure 5.24, displaying a maximum in correspondence of the hottest slice itself.

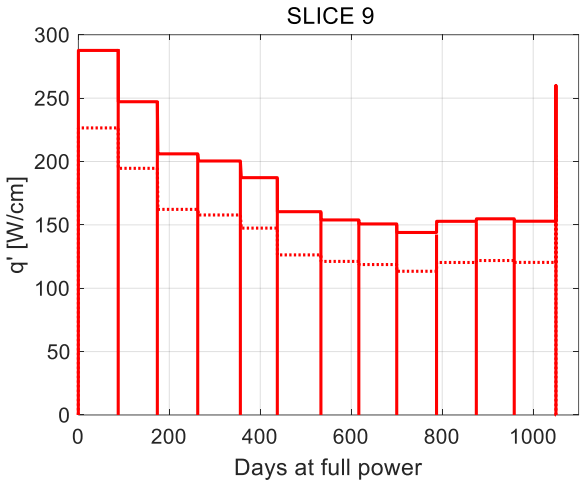

Figure 5.23: Linear power evolution in time at slice 9 in nominal (dotted line) and limit (solid line) power conditions – BPJ at batch 12.

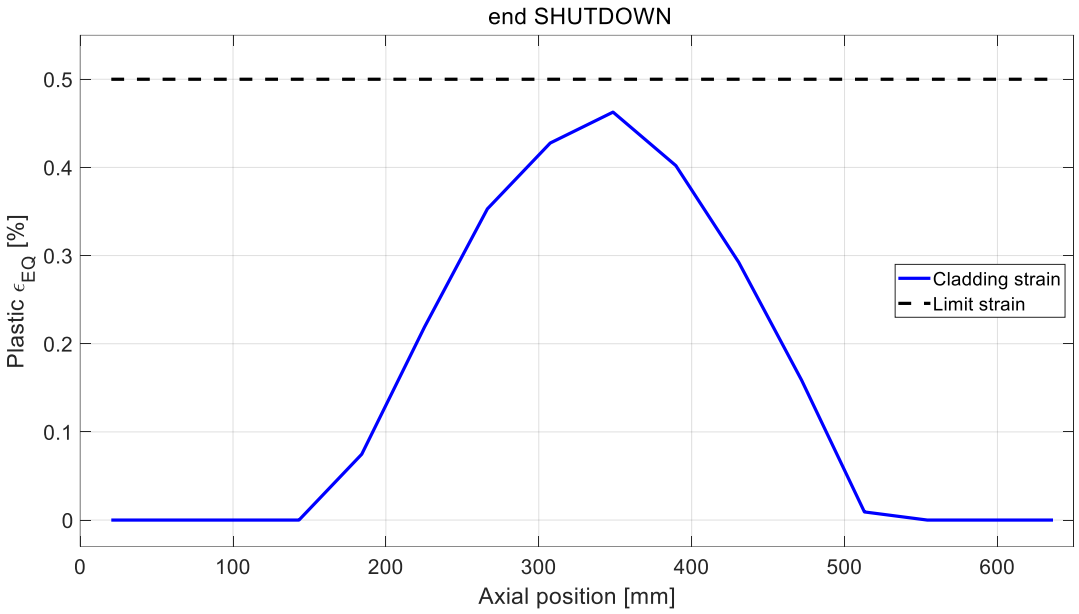

Figure 5.24: Cladding axial plastic strain at shutdown in limit power conditions in WC - BPJ at batch 12.

As already discussed in deep, the main responsible for the plastic strain is the FCMI, beginning towards the middle of batch 6 if a power increment by 27% is considered (instead of being at the end of batch 9), as demonstrated in Figure 5.25. From that irradiation instant on, the cladding loading situation switches to imposed deformation (by the fuel), and the contact pressure continuously increases until reaching a maximum value of about 80 MPa, which corresponds a cladding equivalent stress of almost 500 MPa (Figure 5.26, left)[55]. At this stage (beginning of batch 12), yielding takes place and cladding stress ceases to growth even during the overpower

[55] Note that, owing to the two *Többe correlations* featuring the worst case scenario, no stress relaxation is observed throughout the whole pin in-reactor life. Such fact certainly has a strong influence in determining the situation with the maximum possible cladding plastic strain, given that the stress can continue to rise undisturbed until reaching yielding.

transient, due to the perfect plasticity assumption made by the TRANSURANUS code. On the other hand, the plastic strain continues to increase with a sudden peak during the BPJ, as shown in Figure 5.26 (right). It is at this point that the FCMI achieves its major strength.

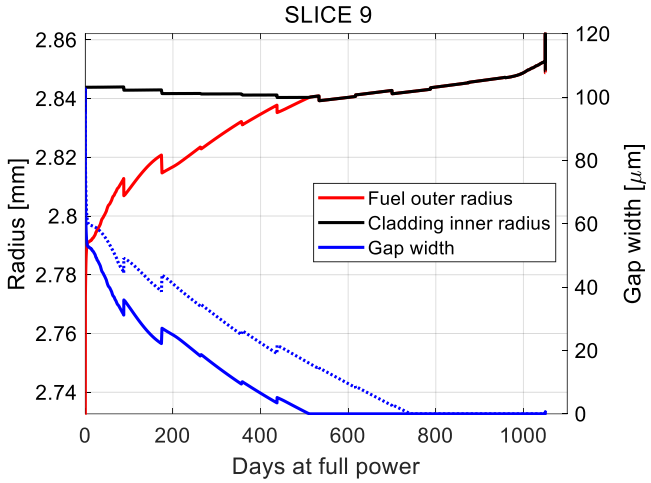

Figure 5.25: Gap evolution in time at slice 9 in nominal (dotted line) and limit (solid line) power conditions in WC – BPJ at batch 12.

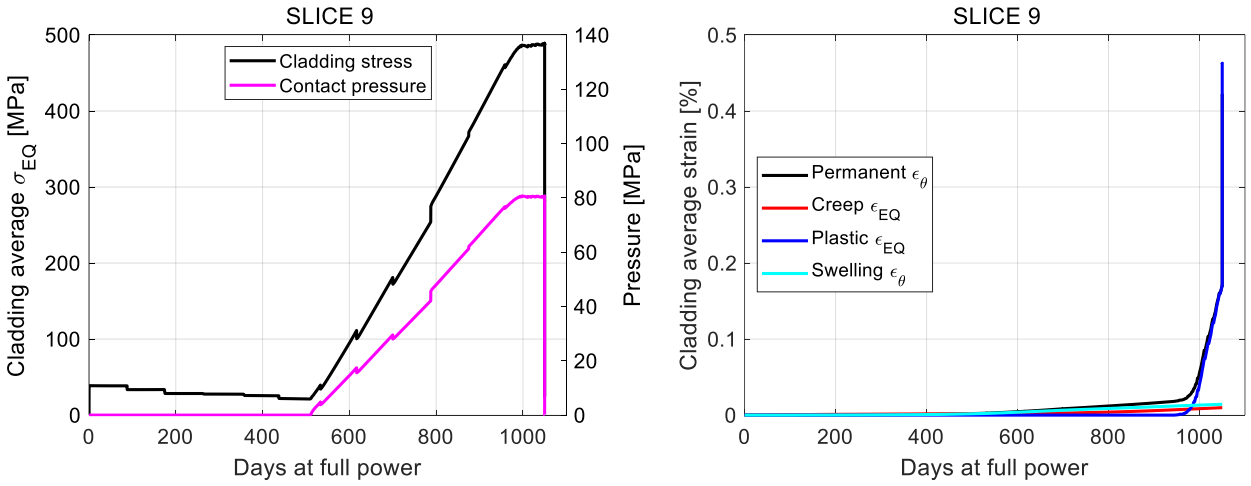

Figure 5.26: Evolution in time of cladding equivalent stress and contact pressure (left) and of irreversible strain components (right) in limit power conditions, in WC - BPJ at batch 12.

Chapter 6

Conclusions

This thesis work has dealt with MYRRHA (Multi-purpose Hybrid Research Reactor for High-tech Applications) fuel pin thermo-mechanical assessment exploiting the TRANSURANUS fuel performance code. The structure is in line with the strategic objectives of the INSPYRE (Investigations Supporting MOX Fuel Licensing in ESNII Prototype Reactors) H2020 European Project, aiming at extending the applicability of state-of-the-art simulation tools and to transfer their own potentiality to end-users.

The TRANSURANUS code has been arranged for the performance assessment by reviewing the models implemented in its original *v1m1j18* code version. The focus has been on such correlations addressing the cladding behaviour modelling, with the goal to extend the code predicting capabilities also to DIN1.4970 austenitic stainless steel, the specific material choice for MYRRHA cladding. A deep research in the open literature regarding its creep and swelling response has finally led to the implementation of five correlations, originally developed starting from raw experimental data (by a best fit procedure), or directly taken as they were inside reference papers. The outcome, besides being useful in the context of the simulations performed in this work, should be considered as a starting point for any further development and application, either concerning MYRRHA facility or other reactors adopting DIN1.4970 as cladding steel.

The following step consisted in the fuel pin performance assessment focusing on a fictitious hottest pin, identified on purpose to draw up conservative conclusions about MYRRHA fuel performance. Firstly, normal operating conditions have been investigated, simulating the fuel pin behaviour with the most reliable set of input models ("reference case") and relying on indicative design limits. The results have excluded the presence of any issues, both in terms of cladding deformations (actually, fuel-cladding mechanical interaction never verifies along the whole irradiation history) and of fuel and cladding temperatures. In order to account for the uncertainties associated to the modelling of key fuel and cladding phenomena, significantly affecting the simulation outcomes (i.e., cladding thermal and irradiation creep, void swelling, fuel swelling and fuel thermal conductivity), a sensitivity analysis on models has been employed, with the aim to identify those correlation sets supplying the worst fuel pin conditions in terms of fuel temperature or cladding deformation ("worst case"). The scenarios thereby defined have proven

a worse but anyway satisfactory response, with a slight fuel-cladding mechanical interaction leading to a weak contact pressure and irreversible cladding strains far from their design limits; the only exception has been the maximum fuel temperature, slightly above its threshold and so requiring a special monitoring. Design limits, however, have not been considered as strict boundaries, rather as guidelines useful to filter the simulation outcomes and to provide a qualitative judgement, as they were not defined on purpose for the facility under consideration.

Finally, the MYRRHA hottest pin response to a particular design basis accident entailing an overpower condition originating from the worst possible accelerator beam current trip, has been investigated. In such case, tailored accidental design limits on fuel melting and excessive fuel-cladding mechanical interaction hold. Four beam power jump transients have been selected to represent beginning-of-life, mid-life and end-of-life conditions, on the base of the normal operation analysis results. What has been found is that the minimum margin to fuel melting is reached during a transient at beginning-of-life, whereas it is a beam power jump happening at end-of-life which brings the cladding closer to the plastic strain limit; mid-life conditions, instead, do not involve any criticality. A sensitivity analysis on models has been performed again, proving to be essential especially for an end-of-life accidental scenario. The maximum fuel temperature reached during a premature beam power jump, indeed, stays well below the melting threshold, both in reference and in worst case. On the other hand, the occurrence at end-of-life entails in reference case a restriction of the gap width without achieving its closure throughout the whole axial length; with the worst set of models, conversely, a strong fuel-cladding mechanical interaction takes place, resulting very close to the yielding point (still without a plastic deformation, however). In light of the attained results, the last analysis has been devoted to determine the linear power requested to cross the accidental design limits for the most severe transients, considering the worst case fuel pin response: the minimum power increase (over 10% higher than the nominal one) has been found for a beam power jump occurring at beginning-of-life, leading to fuel melting issues.

Summarizing, the MYRRHA fuel pin design can be considered adequate for the most severe beam power jump transient, although very conservative hypotheses have been done and the worst conditions accounting for model uncertainties have been considered. A comparison between base irradiation results and design limits for normal operating conditions properly set for MYRRHA, instead, would be required. Afterwards, an investigation concerning all the selected design basis accidents and normal or off-normal operating transients would be necessary to definitively assess the current MYRRHA fuel pin design. Such steps are left to potential future works.

Bibliography

[1] R. J. M. Konings, *Comprehensive Nuclear Materials, Volume 2*. Elsevier Ltd, 2012.

[2] D. G. Cacuci, *Handbook of Nuclear Engineering*. Springer, 2010.

[3] Y. Guerin, D. Parrat, and J. Noirot, "NUCLEAR FUEL for Light Water Reactors and Fast Reactors," Cadarache, 2016.

[4] A. E. Waltar, D. R. Todd, and P. V. Tsvetkov, *Fast Spectrum Reactors*. Springer, 2012.

[5] P. Van Uffelen, J. Hales, W. Li, G. Rossiter, and R. Williamson, "A review of fuel performance modelling," *J. Nucl. Mater.*, vol. 516, pp. 373–412, 2019.

[6] K. Lassmann, "URANUS - A computer programme for the thermal and mechanical analysis of the fuel rods in a nuclear reactor," *Nucl. Eng. Des.*, vol. 45, pp. 325–342, 1978.

[7] European Commission - Joint Research Center, *TRANSURANUS Handbook (v1m1j17)*. Institute for Transuranium Elements, Karlsruhe.

[8] I. Crossland, *Nuclear fuel cycle science and engineering*. National Nuclear Laboratory: Woodhead Publishing, 2012.

[9] "Generation IV International Forum." [Online]. Available: https://www.gen-4.org/gif/jcms/c_9260/public.

[10] I. L. Pioro, *Handbook of Generation IV Nuclear Reactors*. Woodhead Publishing, 2016.

[11] "INSPYRE Web Page." [Online]. Available: http://www.eera-jpnm.eu/inspyre/.

[12] "INSPYRE Web Page - Word Package 7." [Online]. Available: http://www.eera-jpnm.eu/inspyre/?q=jpnm&sq=sub7.

[13] L. Luzzi *et al.*, "Definition of detailed configurations of the case studies for the fuel performance simulations in Task 7.3," *INSPYRE Milestone MS16*, 2019.

[14] O. Gelineau and S. Gavrilov, "Final report material property requirements for ASTRID and MYRRHA ADS system," *MATTER Deliv. D1.3*, 2011.

[15] J. R. Lamarsh and A. J. Baratta, *Introduction to Nuclear Engineering*, 3rd Ed. Prentice Hall, 2001.

[16] L. Edwards, "Generation IV Nuclear Reactors." [Online]. Available: https://www.ansto.gov.au/research/programs/nuclear-fuel-cycle/generation-iv-nuclear-reactors.

[17] OECD / NEA, *Handbook on Lead-bismuth Eutectic Alloy and Lead Properties , Materials Compatibility , Thermal- hydraulics and Technologies*, 2015 Ed. 2015.

[18] H. Aït Abderrahim, P. Baeten, D. De Bruyn, and R. Fernandez, "MYRRHA - A multi-purpose fast spectrum research reactor," *Energy Convers. Manag.*, vol. 63, pp. 4–10, 2012.[19] D. De Bruyn, H. Aït Abderrahim, and M. Schyns, "Recent progress and perspectives in the Belgian MYRRHA ADS program," *Eur. Res. React. Conf. (RRFM 2019)*, 2019.

[20] R. J. M. Konings, *Comprehensive Nuclear Materials, Volume 5*. Elsevier Ltd, 2012.

[21] SCK•CEN, "MYRRHA: a new multifunctional research reactor." [Online]. Available: https://sckcen.be/en/MediaLibrary/Pictures/MYRRHA#prettyPhoto.

[22] J. Engelen, H. Ait Abderrahim, P. Baeten, D. De Bruyn, and P. Leysen, "MYRRHA : Preliminary front-end engineering design," *Int. J. Hydrogen Energy*, vol. 40, pp. 15137–15147, 2015.

[23] P. Yvon, M. Le Flem, C. Cabet, and J. L. Seran, "Structural materials for next generation nuclear systems: Challenges and the path forward," *Nucl. Eng. Des.*, vol. 294, pp. 161–169, 2015.

[24] W. R. Corwin *et al.*, *Updated Generation IV Reactors Integrated Materials Technology Program Plan*, Revision 2. Oak Ridge National Laboratory, 2005.

[25] L. Malerba, "Structural Materials Challenges for ESNII Reactors." CIEMAT, Spain.

[26] A. Strafella, A. Coglitore, P. Fabbri, and E. Salernitano, "15-15Ti(Si) austenitic steel: creep behaviour in hostile environment," *Frat. ed Integrita Strutt.*, vol. 42, pp. 352–365, 2017.

[27] N. Cautaerts, R. Delville, W. Dietz, and M. Verwerft, "Thermal creep properties of Ti-stabilized DIN 1.4970 (15-15Ti) austenitic stainless steel pressurized cladding tubes," *J. Nucl. Mater.*, vol. 493, pp. 154–167, 2017.

[28] D. R. Olander, *Fundamental Aspects of Nuclear Reactor Fuel Elements*. 1976.

[29] D. Pizzocri, S. Lorenzi, and L. Luzzi, "Extension of the TRANSURANUS code to the 15-15Ti austenitic steels for the fuel pin performance analysis of Gen-IV Liquid Metal-cooled Fast Reactors," *Tech. Rep. CeSNEF-IN-03-2015*, 2015.

[30] L. Luzzi, S. Lorenzi, D. Pizzocri, A. Aly, D. Rozzia, and A. Del Nevo, "Modeling and Analysis of Nuclear Fuel Pin Behavior for Innovative Lead Cooled FBR," 2014.

[31] V. Sobolev, "Preliminary recommendations for thermal and mechanical properties of unirradiated stainless steel 15-15Ti," *Intern. Report, SCK-CEN I-198*, 2011.

[32] H. Többe, "Das Brennstabrechenprogramm IAMBUS zur Auslegung von Schellbrüter Brennstäben," *Tech. Bericht ITB 75.65*, 1975.

[33] IAEA, "Structural Materials for Liquid Metal Cooled Fast Reactor Fuel Assemblies – Operational Behaviour," *IAEA Nucl. Energy Ser. No. NF-T-4.3*, 2012.

[34] L. Luzzi, A. Cammi, V. Di Marcello, S. Lorenzi, D. Pizzocri, and P. Van Uffelen, "Application of the TRANSURANUS code for the fuel pin design process of the ALFRED reactor," *Nucl. Eng. Des.*, vol. 277, pp. 173–187, 2014.

[35] M. F. Ashby and H. J. Frost, *Deformation-mechanism maps: the plasticity and creep of metals and ceramics*. Pergamon Press, 1982.

[36] H. Schroeder, "In-beam creep rupture properties of DIN 1.4970 austenitic stainless steel at 873 K," *J. Nucl. Mater.*, vol. 141–143, pp. 476–481, 1986.

[37] N. Yamamoto and H. Schroeder, "In-beam creep rupture properties of cold-worked DIN 1.4970 and AISI 316 L at 873 K," *J. Nucl. Mater.*, vol. 155–157, pp. 1043–1048, 1988.

[38] J. Radler, "Smooth transition between functions with tanh()." [Online]. Available: https://www.j-raedler.de/2010/10/smooth-transition-between-functions-with-tanh/.

[39] M. L. Grossbeck, K. Ehrlich, and C. Wassilew, "An assessment of tensile, irradiation creep, creep rupture, and fatigue behavior in austenitic stainless steels with emphasis on spectral effects," *J. Nucl. Mater.*, vol. 174, no. 2–3, pp. 264–281, 1990.

[40] S. E. Lemehov, V. P. Sobolev, and M. Verwerft, "Predicting thermo-mechanical behaviour of high minor actinide content composite oxide fuel in a dedicated transmutation facility," *J. Nucl. Mater.*, vol. 416, no. 1–2, pp. 179–191, 2011.

[41] W. Daenner, "A comparison of AISI Type 316 and german Type DIN 1.4970 stainless steel with regard to the first-wall lifetime," *J. Nucl. Mater.*, vol. 103–104, pp. 121–126, 1981.

[42] G. Grasso, C. Petrovich, K. Mikityuk, D. Mattioli, F. Manni, and D. Gugiu, "Demonstrating the effectiveness of the European LFR concept: the ALFRED core design," *IAEA-CN-199/312*, 2013.

[43] OECD / NEA, *Fuels and Materials for Transmutation*. 2005.

[44] F. Vettraino and L. Luzzi, "ADS-demo Fuel Rod Analysis Report," 2001.

[45] P. T. Elton and K. Lassmann, "Calculational Methods for Diffusional Gas Release," *Nucl. Eng. Des.*, vol. 101, pp. 259–265, 1987.

[46] H. Matzke, "Gas release mechanisms in UO2 - a critical overview," *Radiat. Eff.*, vol. 53, pp. 219–242, 1980.

[47] W. Dienst, I. Muelle-Lyda, and H. Zimmermann, "Swelling, densification and creep of oxide and carbide fuels under irradiation," *Int. Conf. fast Breed. React. Perform.*, pp. 166–175, 1979.

[48] T. Preusser and K. Lassmann, "Current Status of the Transient Integral Fuel Element Performance Code URANUS," *Int. Conf. Struct. Mech. React. Technol. (SMiRT), Pap. C 4/3*, 1983.

[49] J. B. Ainscough, B. W. Oldfield, and J. O. Ware, "Isothermal grain growth kinetics in sintered UO2 pellets," *J. Nucl. Mater.*, vol. 49, pp. 117–128, 1973.

[50] C. S. Olsen, "UO2 pore migration and grain growth kinetics," *Trans. Struct. Mech. React. Technol.*, vol. C, p. C1/9, 1-10, 1979.

[51] P. Botazzoli, "Helium production and behaviour in LWR nuclear oxide fuels," Ph.D. Thesis, Politecnico di Milano, 2011.

[52] P. Botazzoli, L. Luzzi, S. Bremier, A. Schubert, and P. Van Uffelen, "Microstructural Evolution in Heterogeneous and Homogeneous MOX Fuels," Karlsruhe, Germany, 2010.

[53] E. Federici, A. Courcelle, P. Blanpain, and H. Cognon, "Helium production and behaviour in nuclear fuelsduring irrdiation in LWR," San Francisco, California, USA, 2007.

[54] K. Lassmann and F. Hohlefeld, "The Revised URGAP-Model to Describe the GAP Conductance Between Fuel and Cladding," *Nucl. Eng. Des.*, vol. 103, pp. 215–221, 1987.

[55] A. L. Lindsay and L. A. Bromley, "Thermal Conductivity of Gas Mixtures," *Ind. Eng. Chem.*, vol. 42, no. 8, pp. 1508–1510, 1970.

[56] R. J. M. Konings, *Comprehensive Nuclear Materials, Volume 3*. Elsevier Ltd, 2012.

[57] A. Schubert, P. Van Uffelen, J. van de Laar, M. Sheindlin, and L. Ott, "Present status of the MOX version of the TRANSURANUS code (F2.5)," Sandefjord, Norway, 2004.

[58] J. J. Carbajo, G. L. Yoder, S. G. Popov, and V. K. Ivanov, "A review of the thermophysical properties of MOX and UO2 fuels," *J. Nucl. Mater.*, vol. 299, pp. 181–198, 2001.

[59] D. Freund, R. Pesl, H. Gärtner, and H. Steine, "SATURN-S, Ein Programmsystem zur Beschreibung des thermomechanischen Verhaltens von Kernreaktorbrennstäben unter Bestrahlung," *Tech. Bericht, KFK 4272*, 1987.

[60] J. C. Melis, L. Roche, J. P. Piron, and J. Truffert, "GERMINAL - A computer code for predicting fuel pin behaviour," *J. Nucl. Mater.*, vol. 188, pp. 303–307, 1992.

[61] K. J. Geelhood, W. G. Luscher, P. A. Raynaud, and I. E. Porter, "FRAPCON-4.0: A Computer Code for the Calculation of Steady-State, Thermal-Mechanical Behavior of Oxide Fuel Rods for High Burnup," *NUREG/CR-7022*, vol. 1, no. PNNL-19418, 2015.

[62] K. J. Geelhood, W. G. Luscher, C. E. Beyer, and J. M. Cuta, *FRAPTRAN 1.5: A Computer Code for the Transient Analysis of Oxide Fuel Rods*, vol. 1, no. Rev. 1. 2014.

[63] Y. Rashid, R. Dunham, and R. Montgomery, "Fuel analysis and licensing code: FALCON MOD01 volume 1: theoretical and numerical bases," *Tech. results*, vol. 1, no. 3, p. 246, 2014.

[64] R. L. Williamson *et al.*, "Multidimensional multiphysics simulation of nuclear fuel behavior.," *J. Nucl. Mater.*, vol. 423, pp. 149–163, 2012.

[65] J. Sercombe *et al.*, "Multi-dimensional modeling of PCMI during base irradiation and ramp testing with ALCYONE V1.1," *Proc. Top Fuel 2009*, 2009.

[66] "About ESNII - SNEPT Web Page." [Online]. Available: http://www.snetp.eu/esnii/.

[67] T. Beck *et al.*, "Conceptual design of ASTRID fuel sub-assemblies," *Nucl. Eng. Des.*, vol. 315, pp. 51–60, 2017.

[68] G. Grasso *et al.*, "The core design of ALFRED, a demonstrator for the European lead-cooled reactors," *Nucl. Eng. Des.*, vol. 278, pp. 287–301, 2014.

[69] R. Stainsby, K. Peers, C. Mitchell, C. Poette, K. Mikityuk, and J. Somers, "Gas cooled fast reactor research in Europe," *Nucl. Eng. Des.*, vol. 241, pp. 3481–3489, 2011.

[70] J. R. Lamarsh, *Introduction to NUCLEAR REACTOR THEORY*. American Nuclear Society, 2002.

[71] N. Korepanova, L. Gu, L. Zhang, and Y. Dai, "Evaluation of displacement cross-section for neutron-irradiated 15-15Ti steel and its swelling behavior in CiADS radiation environment," *Ann. Nucl. Energy*, vol. 133, pp. 937–949, 2019.

[72] A. L. Pitner, B. C. Gneiting, and F. E. Bard, "Irradiation performance of fast flux test facility

drivers using D9 alloy," *Nucl. Technol.*, vol. 112, no. 2, pp. 194–203, 1995.

[73] J. H. Ferziger and M. Peric, *Computational Methods for Fluid Dynamics*, 3rd Ed. Springer, 2002.

Appendix A

Implementation strategy

The routines implemented during the TRANSURANUS review (see Chapter 3) are introduced and described in three main sections: Section A.1 addresses creep strain rate computation, which groups both thermal creep and irradiation creep; Section A.2 aims at the treatment of the cumulative damage function evolution in time; finally, Section A.3 deals with the determination of the void swelling effect. The way each correlation can be selected inside the input file is presented, together with a description about the default options adopted by the TRANSURANUS code in the case a specific choice is not declared in the input file.

Once all the routines have been written, a compilator has been used to translate the FORTRAN language, which is a high level language, in machine code (compilation step). All files, then, have been linked, i.e., it has been made possible for the main program to read and to communicate with the new functions (linking step): the outcome has been a new executable file, which embeds the new correlations. Eventually, TRANSURANUS simulation results (referring to an extremely simplified geometry, in which only the pin cladding is analysed) have been compared with the theoretical models to verify if any error has been committed during the implementation phase.

The steps going from compilation to verification are not described in the following sections, which focus on the content of the new routines developed in the review.

A.1 Creep strain rate

Creep strain rate calculation is treated by the TRANSURANUS code through the real function `etacr`, computing the total deformation rate due to the combined effect of thermal creep and irradiation creep for the axial slice `l`, coarse zone `igrob`, fine zone `i`, under investigation at time `t`.

The correlation adopted to attribute a value to function `etacr` depends on the input variable `ModClad(7)`; whether no preferences are stated (`ModClad(7)=0`), the default option applies. Since MYRRHA facility adopts a steel as cladding material, which is labelled with `2` for the general material property selection (`MPgen_clad`), this means that the calculation entails the use of option `2` which in turn calls the real function `crpc02`. The latter makes use of *Többe* correlation for both thermal creep and irradiation creep, giving back to `etacr` function the sum of the two.

In the following, each one of the modified routines is discussed.

A.1.1 Routine `etacr`

Two new selectable alternatives have been introduced inside `etacr`: option `43` calling the real function `crpc43` and option `44` calling the real function `crpc44` (where the final `c` letter stays for cladding, to differentiate the creep phenomenon it suffers from the one taking place inside the fuel). The first one computes the thermal creep strain rate with the *Többe* correlation (for thermal creep), whereas the second one embeds the *Modified Delville* correlation; both allow switching between *Többe* correlation (for irradiation creep) or *Grossbeck* data fitting to deal with irradiation creep.

To understand why it has been developed another function enveloping the *Többe* correlation for thermal creep, it is necessary to recall two facts. First of all, remember that `etacr` function returns the total creep strain rate. Second, in view of the sensitivity analysis on models performed to evaluate MYRRHA fuel pins behaviour (see Chapter 4 and Chapter 5), it must be taken into account that different combinations of formulae for thermal creep strain rate and irradiation creep strain rate are necessary. Correspondingly, it has been required to allow `etacr` to return a total deformation rate due to all the possible combinations of thermal and irradiation creep models. This is an important underlining since the default option (option `2`) calculates the total creep strain rate without allowing the possibility to switch between different alternatives for the two contributions it is made of. Additional details about how the correlation combination is carried out are given inside the sections treating `crpc` and `irrcrpc` routines.

Besides the value of the total creep strain rate, the new alternatives introduced inside `etacr` function include the call to another routine, called `cdfc`, taking care of the evaluation of the cumulative damage function evolution in time. The outcome of this function is ascribed to the variable `aux(lschni)` which is useful inside the function itself and for such reason further details are given in Section A.2.1.

A.1.2 Routines `crpc43` and `crpc44`

These are the first two routines written from scratch. Precisely, they are real functions through which the calculation of the cladding total deformation rate due to creep is performed.

As for the thermal creep contribution, they take as input from `etacr` the cladding temperature in Kelvin and the applied stress (in the axial slice and radial node under consideration) and provide in output the correspondent strain rate. The last one is computed through *Többe* correlation in the case of `crpc43`, through the *Modified Delville* correlation in the case of `crpc44`.
The irradiation creep contribution, instead, is supplied by the properly developed routine `irrcrpc`, called inside both `crpc43` and `crpc44`.
The two components of the strain rate are summed together and returned to `etacr` function.

A.1.3 Routine `irrcrpc`

Routine `irrcrpc` has been developed anew to satisfy the necessity to be able to join any correlation for irradiation creep to any other for thermal creep. This real function, indeed, is called in both the two routines `crpc43` and `crpc44` and allows selecting the *Többe* correlation (for irradiation creep) or the new *Grossbeck* data fitting by means of the auxiliary variable `iiii1`, passed through the input file. Specifically, when the variable `iiii1` is set equal to `1`, the *Többe* correlation is adopted, whereas when it is set equal to `2`, the *Grossbeck* data fitting is selected; eventually, whether the irradiation creep contribution want to be neglected, `iiii1` must be set equal to `0`.
Regardless the value of the auxiliary variable, the real function takes always as input the neutron flux existing in the considered axial slice and the applied stress, being the influencing variables the same for the two correlations. The output, instead, is just the computed strain rate, which is then added to the thermal contribution inside routines `crpc43` or `crpc44` to provide the total creep strain rate, finally returned to routine `etacr`.

A.2 Cumulative damage function

A.2.1 Routine `cdfc`

As previously said, a call to routine `cdfc` is done, along with a call to `crpc`, inside options `43` or `44` of the function `etacr` to evaluate the evolution in time of the cladding cumulative damage function.
Similarly to the case of routine `irrcrpc`, the function `cdfc` has needed to be written anew, since the computation of the cladding cumulative damage function is usually performed inside `crpc02` without a dedicated routine.
From the comparison among literature data and embedded correlations, it has been decided to keep the existent approach based on P parameter, which is expected to be conservative for MYRRHA, and to interchange it with the new one based on LM parameter, which instead should be a best estimate evaluation. The way to choose the desired approach implemented inside `crpc02` has been preserved, i.e., deciding the favourite one by means of the auxiliary variable `iiii3` from input file. Particularly, setting `iiii3` equal `0` entails the P parameter approach, whereas `3` is the option for the *New LMP* approach.
The inputs for the routine are the cladding temperature measured in Kelvin and the applied stress. The last one is used to derive the time-temperature parameter (P or LM) through the correlation correspondent to the chosen approach; once the parameter is known, temperature allows

deriving the associated time-to-rupture from the parameter definition itself. Eventually, dividing the timestep in which such temperature and stress conditions persist by the correspondent time-to-rupture, the damage function could be determined and summed to the one at the previous time. An additional precaution has been added during the coding: that is, a lower bound on the applied stress equal to 5 MPa, under which the time-to-rupture computation does not apply but the associate damage function is directly set equal to zero. This expedient has been required owing to an overflow error which could be encountered in the calculation with the LMP approach when both the stress and the temperature are considerably small, as may happen with MYRRHA reactor. Such conditions, indeed, entail a very slow creep mechanism which translates in a huge time-to-rupture, capable to exceed the limits of the FORTRAN representable interval. Thus, the overflow limit equal to 10^{37} has been attributed to the time-to-rupture and a boundary LM parameter has been calculated using as temperature the MYRRHA coolant one. A lower bound for the stress, then, has been acquired graphically (Figure A.1), otherwise a bisection method would have been required to compute it analytically[56].

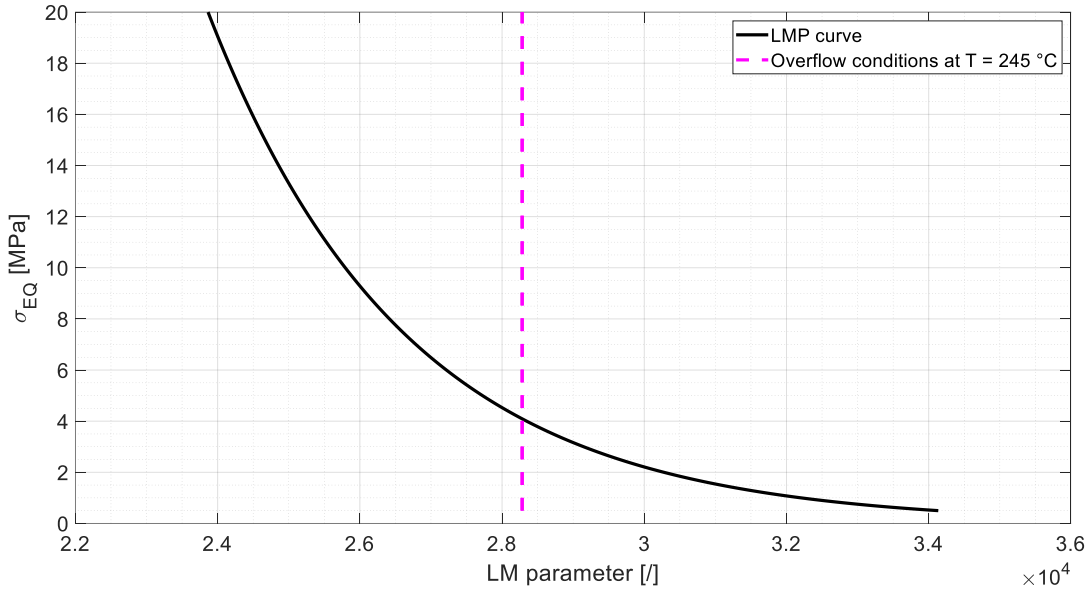

Figure A.1: Graphic determination of the overflow stress limit through a Larson-Miller parameter correspondent to overflow conditions and MYRRHA temperature.

As far as the output of the routine is concerned, `cdfc` has been defined as an integer function supplying as outcome an index proving if cladding has reached rupture due to an excessive cumulative damage. In detail, a variable called `aux` has been attributed to each of the cladding

[56] Note that having assumed the coolant temperature to calculate the limit LM parameter is precautionary from the overflow problem point of view. Since in operating conditions the cladding temperature is certainly higher than the coolant one, indeed, the corresponding time-to-rupture is lower, moving away from the possibility that it exceeds the representable interval limit. In addition, it is expected that the stress rises after the BOL, so the previous discussion holds again.
Finally, even in the eventuality that the stress remains equal to the fixed lower bound with an increasingly hotter environment, temperatures far from the typical MYRRHA range would be necessary to involve a consistent rise of the cumulative damage function.

axial slices and its value is modified inside routine `etacr` assuming the one given back by the `cdfc` function. As soon as the first radial node of the `l`-th axial slice reaches a CDF equal to 1, the output of the function becomes 1 and in turn the variable `aux(l)` does; TRANSURANUS displays the time when cladding reaches rupture as well as the slice where it occurs. For the successive radial nodes, `aux` variable remains equal to 1 independently from their CDF value since rupture has been already reached. The procedure repeats for all the axial slices in which the cladding is subdivided.

A.3 Void swelling

The way adopted by TRANSURANUS to deal with swelling is analogous to the one it employs for creep: `sweloc` routine is the main inventory containing all the possible models to treat the phenomenon (similarly to `etacr`); then, according to the value assumed by variable `ModClad(4)` inside input file, the corresponding alternative is referred to.
Again, the default option is called in the case no preference has been stated (`ModClad(4)=0`), meaning option `2` for a steel cladding. Differently from creep, however, there is not a call to a default separate function (as `crpc02`) but the swelling *Specific AIM1* correlation is implemented in code lines immediately after the cross reference[57].
Regarding the implemented correlations, it has been chosen to follow the same strategy adopted for creep, so two new separate routines have been generated from scratch (`swec43` and `swec44`).

A.3.1 Routine `sweloc`

Two new selectable alternatives have been implemented inside `sweloc`: option `43` calling the routine `swec43` and including *Lemehov* correlation for the "B version" of DIN1.4970, and option `44` calling `swec44` for the "L version" (again, the final `c` letter stays for cladding).
The two real functions determine the isotropic single strain increment due to the swelling effect during one timestep. The outcome of the functions is attributed to variable `deltas`, exploited in turn to calculate variable `eta(igrob,i,kn,7)` representing the strain due to swelling (index `7`) for the radial, axial and tangential components (index `kn`) of the radial node `(igrob,i)`. Variable `eta` is obtained for each direction adding `deltas` (which is always the same being the swelling isotropic) to the swelling strain at the previous time (`eta7(igrob,i,kn)`).
Eventually, `sweloc` routine provides as outcomes all the three strain components: this is possible because, differently from `etacr` which is a function, `sweloc` is a subroutine.

A.3.2 Routines `swec43` and `swec44`

The two `swec` routines are precisely real functions. They require in input the neutron fluence (E>0.1 MeV) at the time under consideration and at the previous time, as well as the temperature in Kelvin. The two neutron fluences are necessary to compute the increment of the fluence itself during the current timestep, which is the basis to determine the swelling effect pertaining to that interval (`deltaV_rel`). The output of the two functions is not the volumetric increase, rather the single strain component increase, which is one third of the total, being the swelling isotropic.

[57] The presence of the *Specific AIM1* as default option originates from the *extended PoliMi* version of TRANSURANUS code, addressed to ALFRED reactor (employing AIM1 as cladding steel).